Experimental and Computational Study of Vibration-Based Energy Harvesting Systems for Self-Powered Devices

Saeed K. ALNuaimi

Dissertation submitted to the Faculty of the
Virginia Polytechnic Institute and State University
in partial fulfillment of the requirements for the degree of

Doctor of Philosophy
in
Engineering Mechanics

Muhammad R. Hajj, Co-Chair
Saad A. Ragab, Co-chair
Lei Zuo
Alexandrina Untaroiu
Surot Thangjitham

15th of December, 2020
Blacksburg, Virginia

Keywords:Method of multiple scales, Energy harvesting, Piezoelectric materials,Energy harvesting, Galloping, Phenomenological modeling, Nonlinear damping, XBee Communication,piezoelectric, composite material.Numerical simulation ,CFD, Ansys Fluent.

Experimental and Computational Study of Vibration-Based Energy Harvesting Systems for Self-Powered Devices

Saeed K. ALNuaimi

ABSTRACT

Energy harvesting of ambient and aeroelastic vibrations is important for reducing the dependence of wireless sensing and networks on batteries. We develop a configuration for a piezoelectric energy harvester with the capability to wirelessly communicate vibration measurements while using those vibrations to power the sensing and communication devices. Particularly, we perform experiments that aim at identifying challenges to overcome in the development of such a configuration. Towards that objective, we successfully tested a self-powered real-time point-to-point wireless communication system between a vibration sensor and transmission and receiving modules. The sensing device and transmission module are powered by the vibrating object using a piezoelectric energy harvester. The communication is established by using two XBee modules. In the second part of this dissertation, we address the optimization of the output power of piezoelectric energy harvesters of aeroelastic vibrations. Given the complexity of high-fidelity simulations of the coupling between the fluid flow, structural response and piezoelectric transduction, we develop and experimentally validate a phenomelogical reduced-order model for energy harvesting from wake galloping. We also develop a high-fidelity simulation for the same phenomena. The modeling and high-fidelity simulations can be a part of a multi-disciplinary optimization framework to be used in the design and operation of galloping-based energy harvesters.

Experimental and Computational Study of Vibration-Based Energy Harvesting Systems for Self-Powered Devices

Saeed K. Alnuaimi

GENERAL AUDIENCE ABSTRACT

Energy harvesting of ambient or flow-induced vibrations is important for reducing the dependence on batteries in wireless sensing and networks to monitor deterioration conditions, environmental pollution or wildlife conservation. Balancing the benefits and shortcomings of a specific approach, namely piezoelctric transduction, for energy harvesting from vibrations, we address a specific challenge related to the development of a configuration that allows for communicating measured vibrations using their power. Furthermore, given the low levels of output power from piezoelectric transduction, we address the need to optimize power output levels through the development of predictive models that depend on geometry and speed of the fluid flow.

Dedication

To my parents who passed. To my wife and my children,bothers and sister.

Acknowledgments

I begin by thanking Almighty Allah for all the wisdom He bestowed upon me during my graduate studies. I thank my advisors, Dr. Muhammad Hajj and Dr. Saad Ragab, for their immeasurable support and guidance. I wish to extend gratitude to the rest of my committee members: Dr. Lei Zuo, Dr. Alexandrina Untaroiu, and Dr. Surot Thangjitham for their support and contributions to my research.

Special thanks go to my fellow researchers: Dr. Mohammad Y. Al-Haik, Dr. Mohamed Zakaria, Dr. AbdulMohsen Al-Othman, Dr. Hisham M. Shehata, Dr. Ahmed Hussein, Dr. Jamal Alrowaijeh, Guillermo Gonzalez, Vamsi Chandra and Mustafa Bukhari. I would like to also thank Dr. Hassan Fayed for sharing his experience and words of wisdom about the academic world.

Most importantly, I would like to extend my most significant appreciation to my wife and kids, who have sacrificed so much for me to accomplish this work.

Lastly, I would like to thank the administrative staff of the Department of Biomedical Engineering and Mechanics (BEAM) for their assistance throughout my studies.

Chapter 1

Introduction

One of the challenges in the development of wireless sensing and communication technologies is the ability to provide power for prolonged periods to avoid replacing batteries on a regular basis, especially when the sensor or device is located in a hard-to-reach place.. This ability will enhance the development of capabilities to continuously monitor deterioration in structures and environmental pollution and of smart and connected systems. In many cases, power sources including ambient vibrations and fluid flows are readily available and can be exploited to harvest energy and power wireless sensing and communication devices. Different mechanisms based on electromagnetism [1,2], electrostatic [3], and piezoelectric [4] transduction can be used to convert mechanical energy to useful electrical power. Of these mechanisms, the piezoelectric transduction is most durable and easy-to-implement for harvesting ambient vibration energy, especially when considering small devices and low power levels [5]. The same is applicable to harvesting energy from air flows through aeroelastic vibrations including vortex-induced vibrations, galloping and flutter.

Several questions remain when it comes to piezoelectric energy harvesting of vibrations. One question is related to the need in many situations to measure or sense the vibrations that are used as a power source. Monitoring wildlife is one example where one needs to power a communication device on an animal. A battery has a limited life-span. As such, the question arises as to the possibility of monitoring the animal from its motion and at the same time use that motion to power the sensor. Another question is related to enhancing the performance of piezoelectric energy harvesters. For instance, in the case of a fluid flow, such an enhancement will require optimization of geometry of the aeroelastic structure for a specific fluid flow. This dissertation aims at answering these questions with teh following objectives:

In the first chapter, we focus on exploiting piezoelectric energy harvesting to measure and the vibration and transmit the measurements. The main objective is to develop a configuration for a self-powered real-time point-to-point wireless system that communicates measured vibrations using the vibration power. In the second chapter, we develop and validate a single equation that directly predicts the energy levels that can be harvested from large oscillations of an object subjected to wake galloping. In the third chapter, we implement a high-fidelity simulation to determine energy that can be harvested from wake galloping. The combination of the models developed in the second and third chapters provide the basis for developing a multi-disciplinary optimization framework for enhancing the performance of galloping-based energy harvesters.

Chapter 2

Remote vibration sensing system with locally-powered devices

Track changes is on 23

2.1 Introduction

In the context of the Internet of Things and smart systems, effective sensing relies on wireless connectivity of spatially distributed autonomous sensors and devices that acquire and transmit data to a primary location. To date, the majority of sensing and wireless transmission devices rely on wired connections or batteries that require frequent replacement, which may not be practical depending on the needs and applications. Although the lifespan of batteries can be extended in some applications by setting the sensor in the sleep mode and waking it up only when data is needed, fitting and replacing batteries may not always possible, especially in remote and inaccessible locations. In contrast, advances made towards the development of low-power microcontrollers and sensing devices, and ultra-low-power wireless technologies open the opportunity for substituting depletable batteries with low levels of locally-harvested energy to power sensing and communication devices.

The predominant approach to exploiting locally-harvested energy has been to use an auxiliary harvester, such as a solar, thermoelectric, or mechanical energy harvester, to operate vibration or flow sensing and transmission devices [6]. Still, there exist some challenges. Simjee et al. [7] noted that, in low-power applications, the interaction between the harvesting circuit of small-scale solar harvester systems and the powered device affects the feasibility of designing a solar harvester independently from the embedded systems. Similar issues must be addressed when using low-current piezoelectric transducers or low-voltage thermoelectric generators.

Given that a monitored quantity, such as vibrations, temperature or flow speed can be also considered as an energy source, it would be advantageous in many applications to use the monitored system as the energy source. With this capability, there is better matching between the required power and sensing needs. Furthermore, the size of the sensing and communication elements is reduced because there is no need to attach an auxiliary energy harvester. More importantly, using the monitored system as the energy source allows for implementing sensing and communication in challenging environments and applications. For instance, it is not possible to add an auxiliary device to power a fish tag that monitors migration behavior and survival of fish species. In that respect, using a depletable battery is not an option. One approach would be a piezoelectric energy harvester from fish motion to power a piezoelectric-based acoustic fish transmitter such as the one developed by Deng et al. [8].

Different approaches have been considered to use the monitored system as the energy source.

Liu et al. [9] proposed a self-sustained flow-sensing microsystem consisting of a PZT micro-cantilever beam that is powered by an array of similar micro-cantilevers that harvest energy from wind-driven vibrations without consideration of wireless transmission. Li et al. [10] implemented battery-free acoustic transmitter that is powered by a flexible piezoelectric beam, which harvests energy from fish swimming. Tan et al. [11] used a wind turbine to generate power for a wireless sensing node that measures the wind speed for predicting wildfire spreading. Alrowaijeh, Hajj et al. [12] presented autonomous sensing of airspeed without a need for wired connections to an external power source or batteries.

Recognizing the challenges in supporting self-powered wireless vibration measurement systems using power harvested from piezoelectric beams, we perform experiments that aim at identifying these challenges and approaches to overcome. Particularly, we establish a self-powered real-time point-to-point wireless communication system between a vibration sensor and transmission and receiving modules. The sensing device and transmission module are powered by the vibrating object using a piezoelectric energy harvester. The communication is established by using two XBee modules. A schematic of the proposed system is presented in figure 2.1. The interest is in remote sensing the vibrations of a beam attached to the vibration source. Towards that objective, an energy harvesting module is also connected to the vibrating source to harvest energy that would power the sensing circuit and transmission module. The energy harvesting module includes a piezoelectric beam, a circuit, and a capacitor for energy storage. This capacitor powers the sensing circuit and the transmitting XBee module. The transmitted signal is then received wirelessly by another XBee controlled by an Arduino and a computer.

2.2 Experimental setup

A 900-lb permanent-magnet shaker driven by an amplified signal from a function generator is used as the vibration source as shown in schematic presented in figure 2.2,. The harvester consists of a cantilever beam with a piezoelectric patch that is mounted on the shaker. The geometric and material properties of the two beams are presented in Table 2.1 and Table 2.2

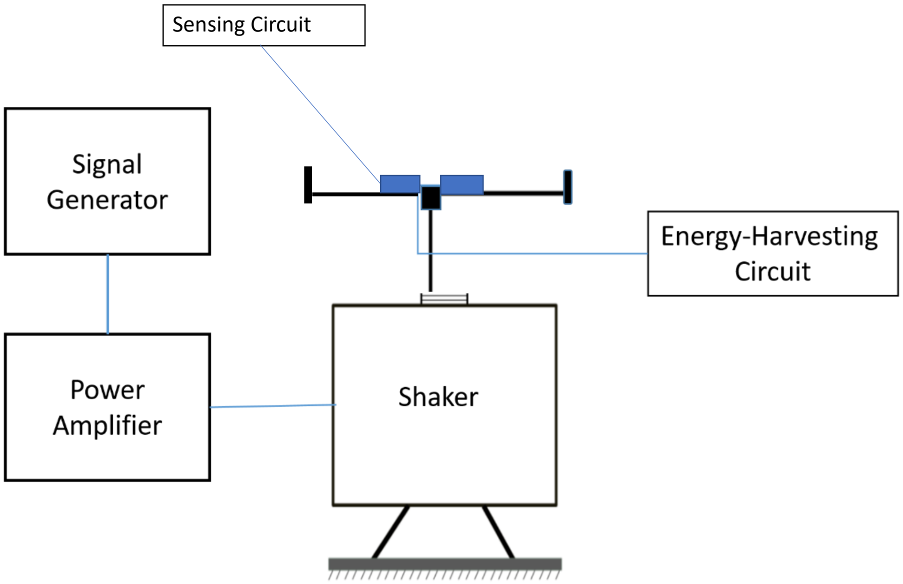

Figure 2.1: Illustration of the Vibration source

(b)

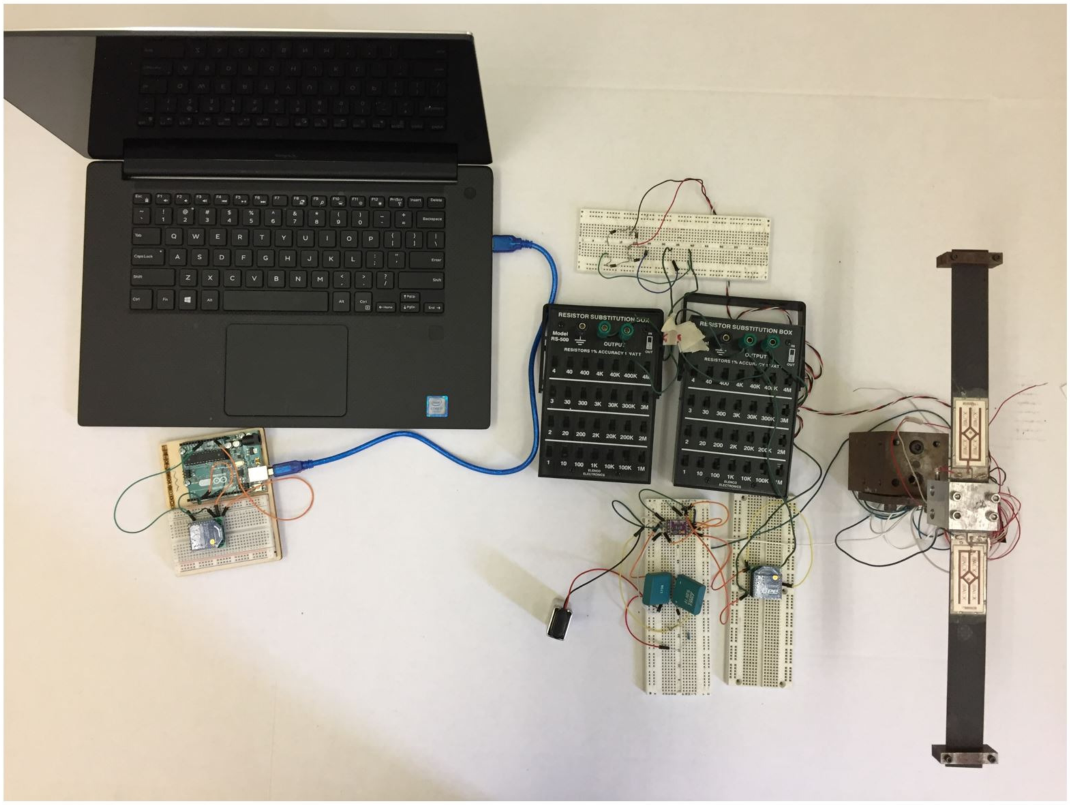

Figure 2.2: Illustration of the Vibration source

Property	**value**
mass density (ρ)	1409 Kg/m^3
Young's Modulus (E)	60 GPa
Length horizontal beam (l)	150 mm
Width (b)	25.4 mm
Thickness (t)	1 mm
Mass of the tip mass(m)	35.2 gm

Table 2.1: Material and geometric parameters Composite beam

Layer material	**Thickness (mm)**
Polyester	0.05
Copper	0.03
PZT 5H	0.15
Stainless Steel 304	0.15
Polyimide	0.03
Total	0.46

Table 2.2: Composition of piezoelectric patch PPA-1001 (MIDE engineering solutions)

2.3 Experimental results and discussion

The power output of the piezoelectric device is intermittent, alternating, and noisy, depending upon the vibrating source. Therefore, a suitable interface is needed to store the available power from the piezoelectric device and provide a stable power supply. Moreover, a backup medium-term to a long-term storage device may be needed to ensure uninterrupted communications during instances of low vibrational energy. Based on these considerations, a battery and super-capacitor-assisted energy harvester circuit is developed using the energy harvesting module $LTC-3588$. The overall scheme for the energy harvester circuit is shown in figure 2.3. The voltage output of the $LTC-3588$ is set to $3.3V$. The energy harvested from the piezoelectric device is stored in the super-capacitor. A backup 9 Volt battery is connected in parallel with the super-capacitor to ensure uninterrupted communications even if the piezoelectric device does not generate energy for a considerably long time. Note that a diode and a resistor are inserted between the battery and super-capacitor to limit the current and possible reverse power flow that could damage the battery. Finally, the 3.3 V DC power output from the Vcc pin of LTC-3588 IC is sent out to the sensing circuit as required by the communication circuit.

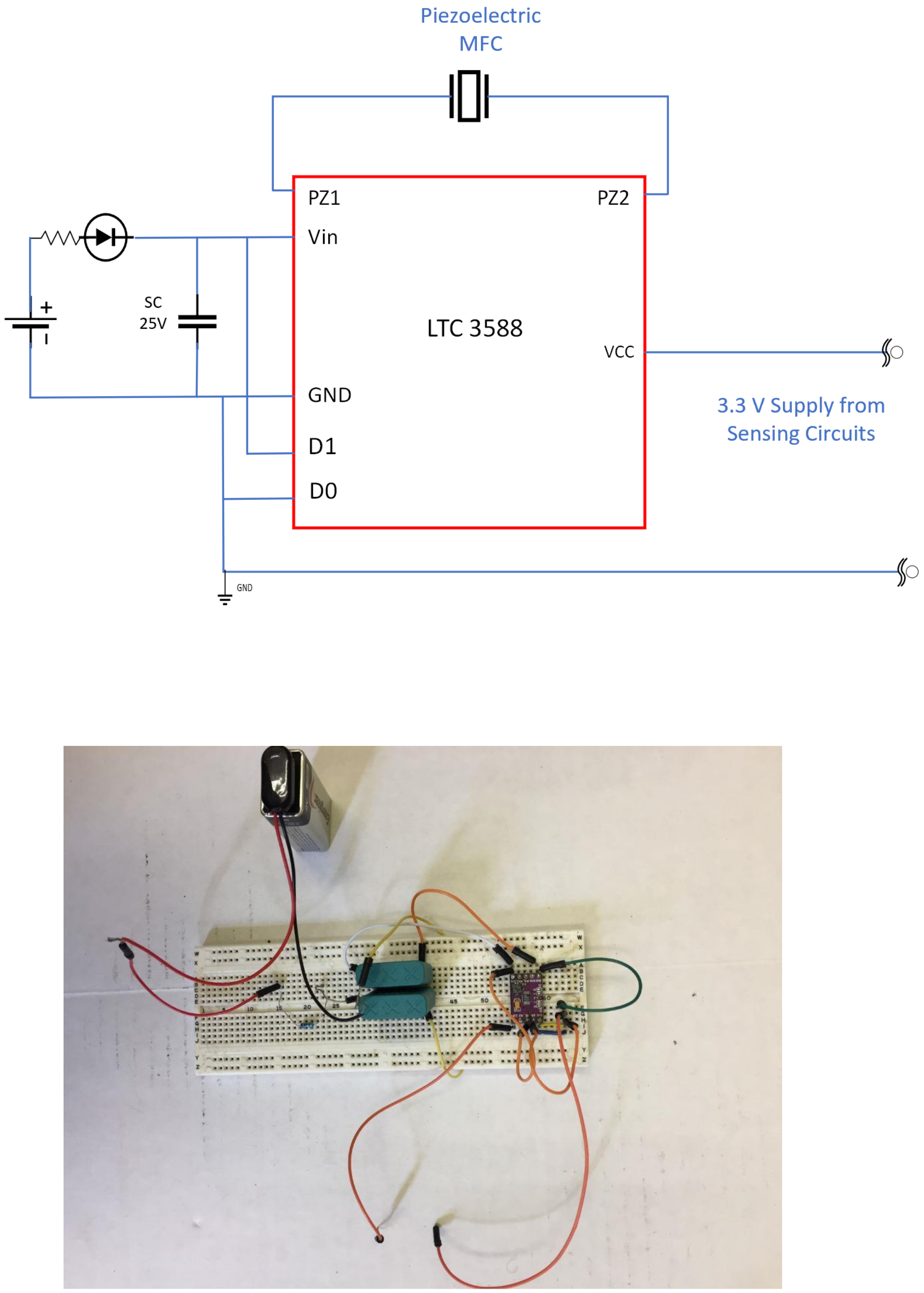

Figure 2.3: Block Diagram of the energy Harvesting Circuit and 3.3 V Supply“to” Sensing Circuit

These requirements result in the sensing circuit diagram presented in figures 2.4a-2.4b that is attached to the transmitting module. The full-wave bridge rectifier shown in this figure is built using four diodes. For an input signal X(t), the output of the full-wave rectifier is the absolute value of |X(t)|. A resistance potential divider is used to step down the voltage to the range of the XBee. For the input signal |X(t)| to the potential divider, its output at the acquisition point is R2|X(t)|/(R1+R2). It should be noted that the voltage step down factor depends only on the relative magnitudes of the resistance limbs R1 and R2, and not on individual values. However, large values for R1 and R2 help in keeping the power loss in the potential divider low. Hence, the values of the two resistances were chosen to be R1=1 MOhms, R2=100 kOhms. Thus, for an input voltage signal from piezoelectric between -35 V and +35 V, the final signal R2|X(t)|/(R1+R2) transmitted to the XBee module is limited to values between 0 and 3.3 Volts, which is within the desired limits. The output signal from the potential divider, which conditioned for the ADC input of XBee is next send to the D0 pin of XBee1, which configured as an ADC pin. The XBee1 serves as a router that sends the local measurements to the remote receiving unit XBee2. The transmission range for the XBee modules used in this setup is between 30 m (indoor) and 50 m (outdoor). Higher configuration devices may be used to extend the communication range, as needed. The ADC in XBee1 needs a reference voltage Vref, to serve as the analog equivalent of the highest discrete value of 10^2-1. To attain the maximum resolution, the reference is chosen as Vref=3.3 V. Thus the Vref pin on XBee1 is connected to the Vcc, the supply voltage pin.

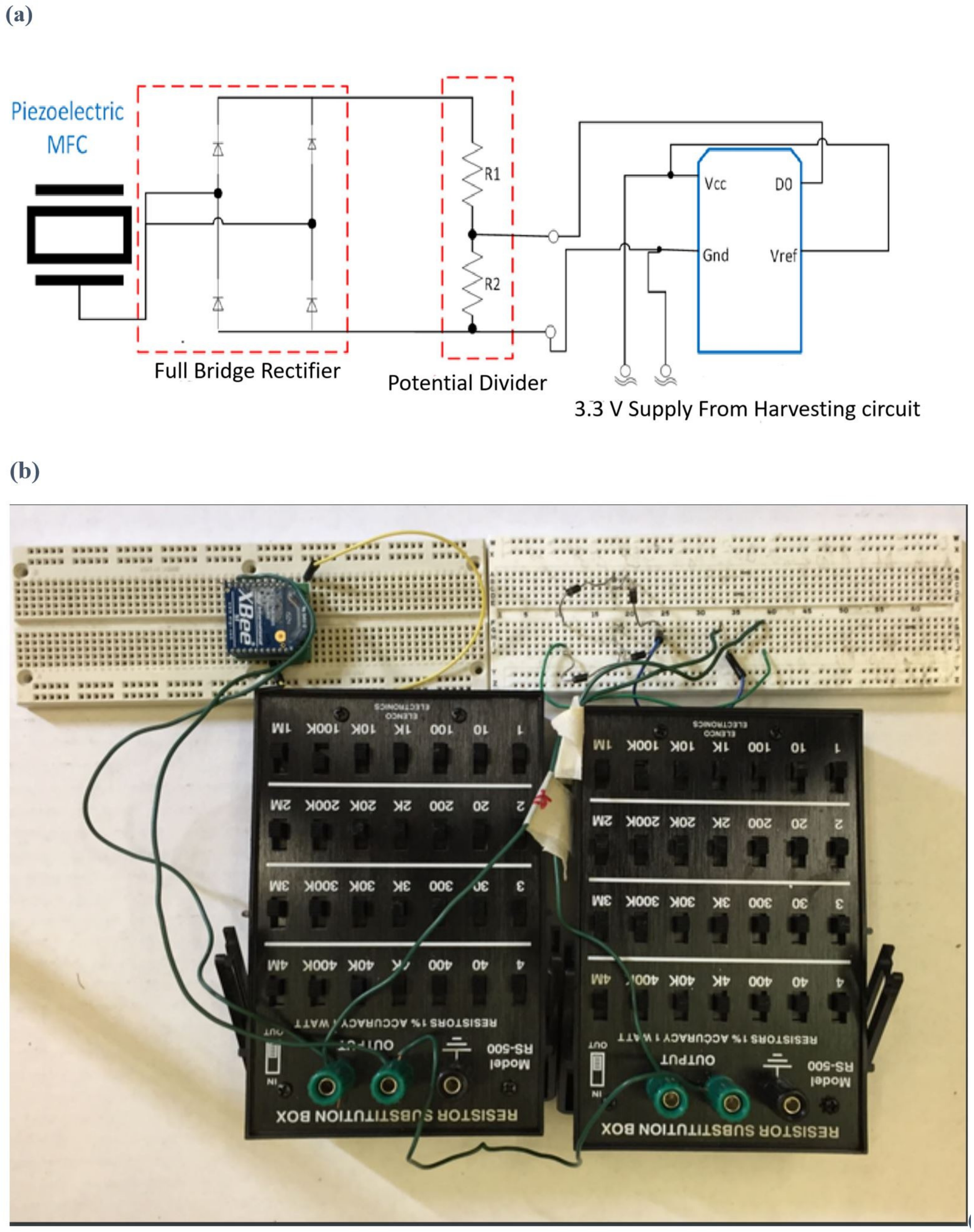

Figure 2.4: Block Diagram of the sensing Circuit.

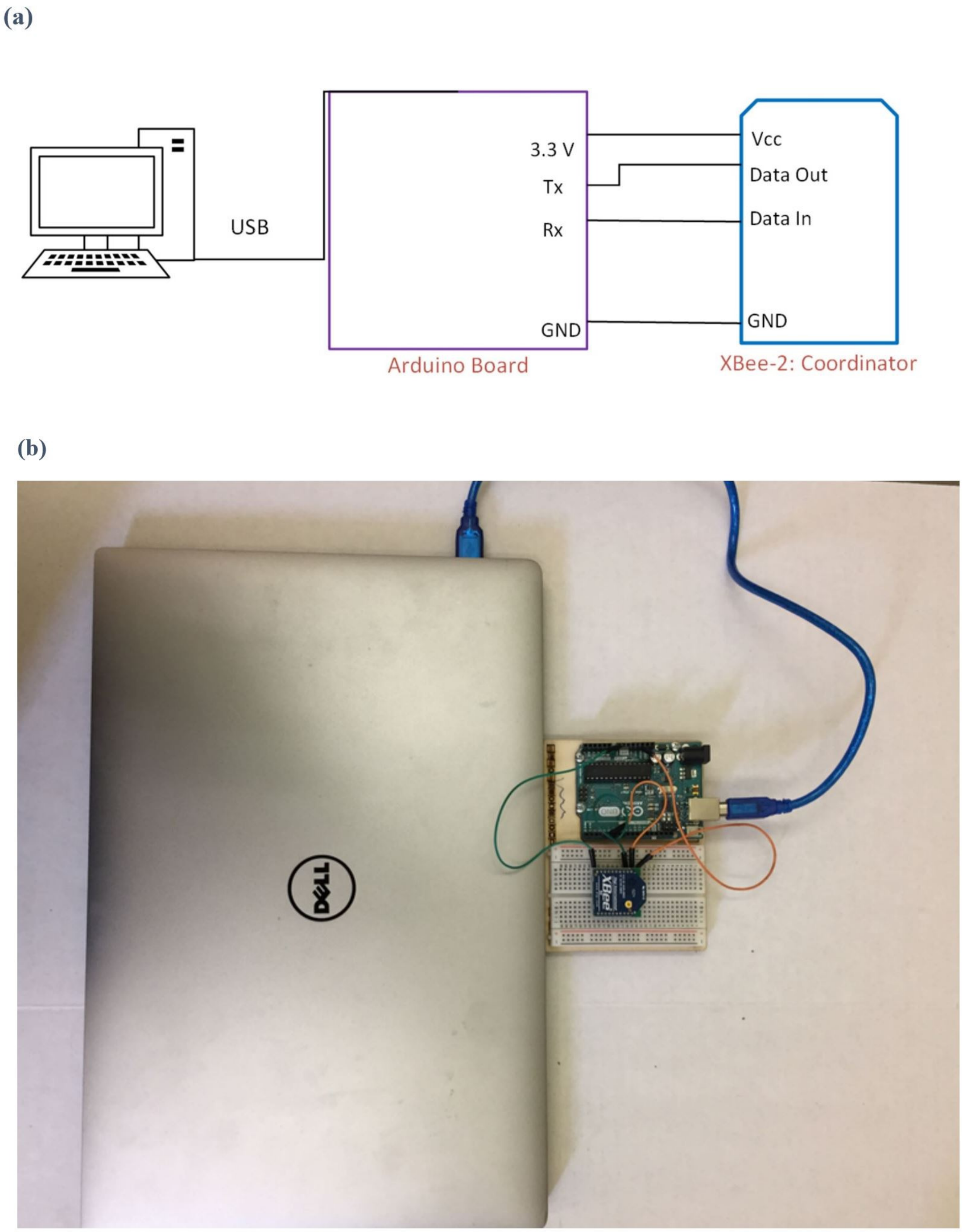

Figure 2.5: Block Diagram of the communication circuit

The data transmitted by XBee-1 shown in Figures 2.5a-2.5b is received by the receiver XBee-

2 shown in Figure 5. XBee-2 passes on the data received from XBee-1 to an Arduino circuit through the Tx-Rx pins. The on board 3.3V DC power supply from the Arduino board is used to power XBee-2. The Arduino board can be used to conveniently communicate with a PC using a USB connection. However, the data received by XBee-2 is in a specific XBee protocol, which needs to be externally decoded in the Arduino Web editor software. The detailed list of components used in building the energy harvesting, sensing and receiver circuits is provided in Table III.

Sl No.	Component name	Circuit	Description
1	XBee-1 & XBee-2	Communication	Series 1, 1mW modules from Digi International
2	Diodes	Sensing	1N4007 Rectifier Diode 1a 1000v
3	Resistances	Sensing	R1=1 MOhms, R2=100kOhms
4	Piezoelectric Patch	Sensing	PPA-1001
5	Supercapacitor	Harvesting	9V1F ESR 350m Ohm 8x22mm Radial Lds
6	LTC-3588	Harvesting	Energy Harvest Collector
7	ARDUINO UNO	Receiver	ATMEGA328, ARDUINO UNO R3 SMD ED

Table 2.3: Component description for the circuits

To establish a successful communication between the two XBee's, they need to be configured suitably. To do so, the open-source configuration software X-CTU 6.3 was used. For each node, we used X-CTU software provided by Digi International. This software enables the user to update the parameters, and perform communication testing easily. For example, the Router radio is programmed with AT Firmware and the Destination address DH, DL is given as the Source address (Serial Number SH,SL) of Coordinator.The PAN ID and Baud Rate should be same for both router and coordinate. The pin 20 –(Digital Input/Output) DIO 0 of Router is to be connected to the pin is declared as DIGITAL INPUT. Also, set the IR Sampling Rate as hex value 1388 which equals 5000 in Decimal.i.e a digital sample is sent every 5000 ms or 5 secs in the router node. As well, set the API mode Enable in the coordinate node.

XBEE breakout arduino	**XBEE breakout arduino**
PIN 1	+3.3V
PIN 10	GND
PIN 2 (TX)	PIN 0 (Rx)
PIN 3 (RX)	PIN 1 (Tx)

Table 2.4: The configuration of the Arduino with XBee

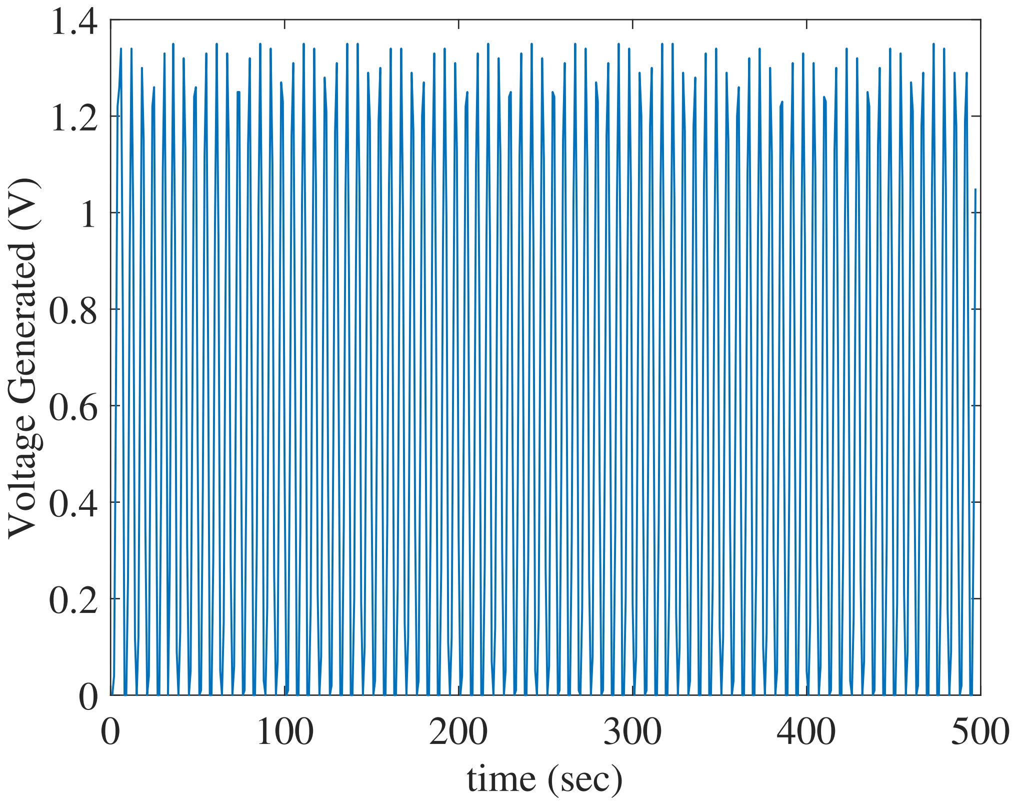

Figure 2.6: Time series of the communicated signal.

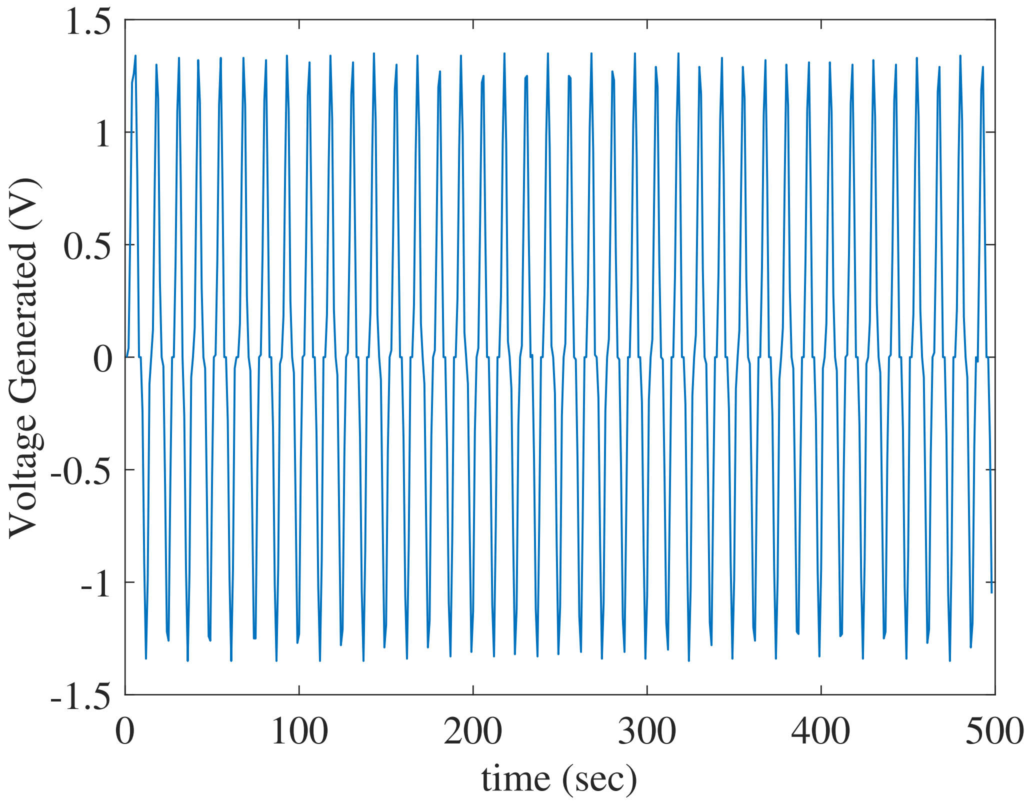

Figure 2.7: Time series of the Full wave rectifier original signal multiplying by -1.

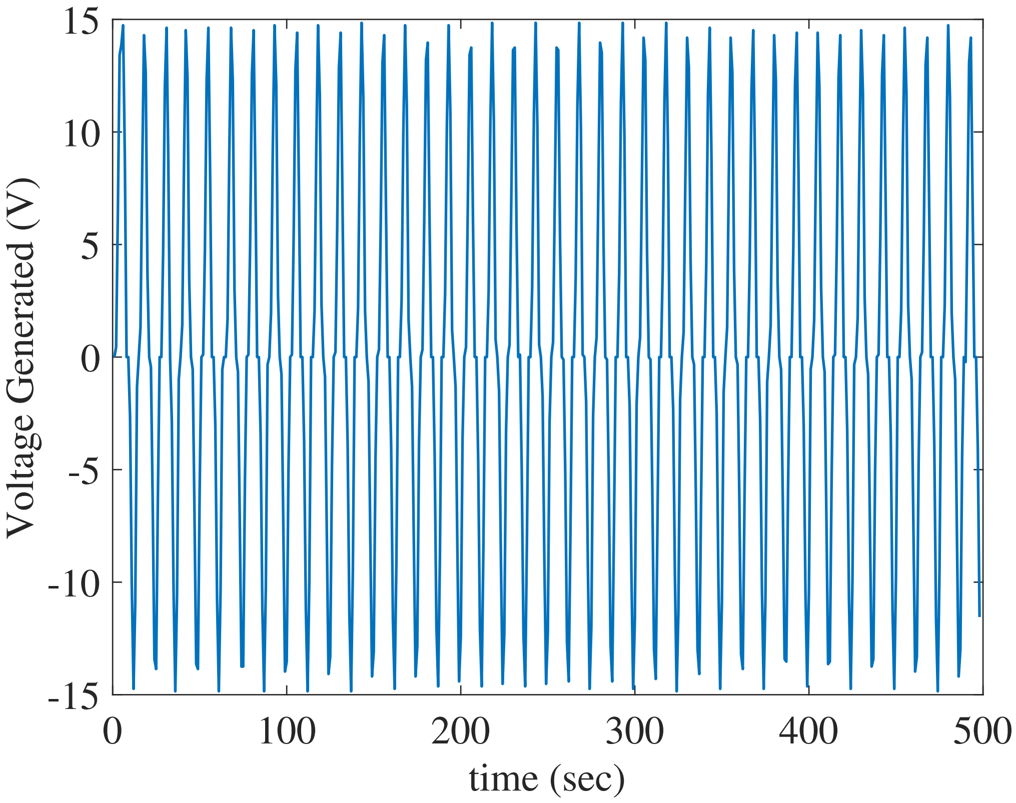

Figure 2.8: Time series of measured signal multiplying by 11.

We shall next present some results to demonstrate the process of recovering the signal from a vibrating object, from the actual signal received by the receiver circuit of Figure2.5. The rectified and scaled down time series signal from a vibrating object is shown in Figure 2.6. Considering that the original signal is alternating, the shape of the original signal was recovered by flipping the alternate half-cycles of the rectified signal received. The transformed signal is shown in Figure 2.7. Next, from the resistance values of the potential divider used in the sensing circuit, it is known that the original signal was scaled down by a ratio 11 : 1. Hence, finally the original transmitted signal was recovered by scaling up by the same factor, as shown in Figure 2.8.

2.4 Conclusion

We have successfully shown that the developed WSNs play a significant role in assisting the gathering of data from large areas. As the locations of deployment often lack the infrastructure required, this is often associated with a certain degree of wireless communication and independence from the electrical grid. Thus, WSNs are made up of numerous nodes to which devices of wireless transmission and batteries are attached. As a consequence, the storage capacity of the battery establishes the WSN operating time, and the encoded logic within the nodes is driven by it. In this context, research is underway to minimize the consumption of energy through the assessment of the methods of transmission and processing data before the transmittance of wakeup protocols within the mechanism of duty-cycle that is more efficient and effective.

Chapter 3

Phenomenological model of piezoelectric energy harvesting from galloping oscillations

3.1 Introduction

Energy harvesting from fluid flows or fluidic energy harvesting (FEH) at low speeds over small volumes is of interest to power spatially dispersed small sensors and devices for monitoring and communication purposes. More importantly, FEH can augment existing low-power electronics towards developing self-powered sensors [12]. Fluidic energy harvesting is realized through the interaction of air (or water) flow with a structure resulting in aeroelastic (or hydroelastic) vibrations that are then converted to electrical energy using electrostatic, electromagnetic, or piezoelectric transduction. Phenomena that have been considered to harvest energy from fluid flows include wing flutter [13–16], vortex-induced vibrations [17–19], and galloping [20–26]. The galloping phenomenon is of particular interest because the displacement amplitude of a galloping object is usually much larger than the characteristic dimension of the object itself, which is not the case of vortex-induced vibrations or wing flutter. As such, galloping can potentially draw more energy from the fluid flow than other aeroelastic vibrations.

Galloping takes place when an object with a non-circular cross section is placed in a fluid flow. If the object's response is modelled as that of a spring-mass-damper system, its displacement, y, is governed by [27]

$$m\ddot{y} + r\dot{y} + ky = \frac{1}{2}C_F\rho U_\infty^2 A \tag{3.1}$$

where m, r, and k are respectively the lumped mass, damping, and stiffness parameters with m and k defining the frequency ; and U_∞, C_F, ρ, and A are respectively the free stream velocity, aerodynamic lift force coefficient, density of the fluid, and cross-sectional area of the galloping object that is normal the flow direction. Galloping is initiated at a critical speed when the absolute value of the negative linear aerodynamic damping, which is proportional to the object's velocity at small angles of attack, exceeds the structural damping. As the displacement amplitude increases, the assumption of small angle of attack is not applicable and flow and structural nonlinearities limit the displacement amplitude resulting in limit cycle oscillations. As such, galloping is a damping-controlled and velocity-dependent instability. The aerodynamic nonlinearities are usually represented by adding nonlinear dependence on the object's velocity or angle of attack resulting in a general representation that captures subcritical and supercritical Hopf bifurcations [28, 29]

$$C_F = \sum_{i=1}^{2m+1} A_i \left(\frac{\dot{y}}{U_\infty}\right)^i + \sum_{j=2}^{2k} A_j \left(\frac{\dot{y}}{U_\infty}\right)^j \frac{\dot{y}}{|\dot{y}|} \tag{3.2}$$

and where all coefficients are determined by fitting the lift force as a polynomial function of the angle of attack. Adding a piezoelectric element and an electric load to harvest energy from galloping yields to coupling equations 3.1 and 3.2 with a governing equation for the piezoelectric energy harvesting that is given by [30]

$$\dot{V} = -\frac{1}{C_p}\left(\frac{V}{R_l} + \theta\dot{y}\right) \tag{3.3}$$

where V is the harvested voltage, C_p is the capacitance, R_l is the resistance of the electric load, and θ is the electromechanical coupling coefficient.

The models in equations 3.1, 3.2 and 3.3 have been widely used to investigate and optimize the response and power generation levels of galloping-based FEH [21, 22, 25]. One shortcoming of this representation is the quasi-steady assumption of equation 3.2, that the displacement of the galloping object does not impact the flow, which is limited to small amplitude oscillations and only valid at low reduced frequencies, defined by the ratio fD/U_∞ where f is the oscillation frequency and D is the characteristic dimension of the cross section of the object. This assumption is not satisfactory for modeling high-performance energy harvesters where high-frequency responses and large amplitudes are desired. Furthermore, the linearized relation between the harvested voltage and body velocity does not account for nonlinear piezoelectric effects at relatively large amplitudes. Although high-fidelity simulations can be performed to account for the flow dynamics induced by the structure and the nonlinear piezoelectric effects, they remain computationally expensive especially if the interest is in optimizing the performance of galloping-based energy harvesters.

In contrast to quasi-steady models and high-fidelity numerical simulations, phenomenological models can be used to effectively account for relevant phenomena and accurately represent specific aspects of fluidic energy harvesting devices. One example is the wake oscillator model used to model the lift force on a circular cylinder induced by vortex-induced vibrations [31–33]. Particularly, Nayfeh et al. [34] used the method of multiple scales to identify the parameters of phenomenological models representing this force on a stationary circular cylinder. They validated their approach using high-fidelity simulations of the flow over a broad range of Reynolds numbers. Considering the incident flow, galloping object and electrical load as one dynamical system, we develop and validate a phenomenological model that represents energy harvested from an object subjected to wake galloping. Given that the induced galloping is a damping-controlled instability, the aerodynamic damping at large amplitudes is a nonlinear function of the free stream velocity, and that energy harvesting could be represented by a damping term, we introduce in the phenomenological model linear and nonlinear damping terms that account for all of these phenomena. The model coefficients are then identified using an approximate solution of the assumed model and experimental measurements. The identified coefficients are then validated by comparing time series obtained by integrating the governing equation with the experimentally measured time series.

3.2 Experimental setup

The experiments were performed in a suction-type open circuit wind tunnel with a 52 × 52 cm square test section that is 120 cm long . Figure 3.1 shows a schematic of the experimental setup that consisted of two cuboidal cylinders placed in the wake of a circular cylinder. The cylinders are 25.4 cm long and have a square cross section with a side dimension of 1.27 cm. The upstream fixed cylindrical bluff body has a diameter of 1.27 cm. Based on many tests, it was decided to place the cylinders 12.7 cm apart. With this setup, the downstream cuboidal cylinder underwent very large amplitude oscillations.The energy was harvested from a piezoelectric sheet bonded to a composite beam that held the cuboidal cylinder. This beam had a length of 13.97 cm, a width of 2.54 cm, and a thickness of 0.048 cm. These beams were fabricated using two layers of well dried carbon fibers (plainweave SGP196 with 6K filaments count in a tow) with a polymeric matrix made from epoxy resin/hardener. The harvested voltage was measured using DATAQ DI-245 DAQ at a sampling rate of 1000 Hz. Measuring the output electrical power generated by different electrical loads, it was determined that the optimum load resistance is 400 kOhms, which was used in all subsequent experiments.

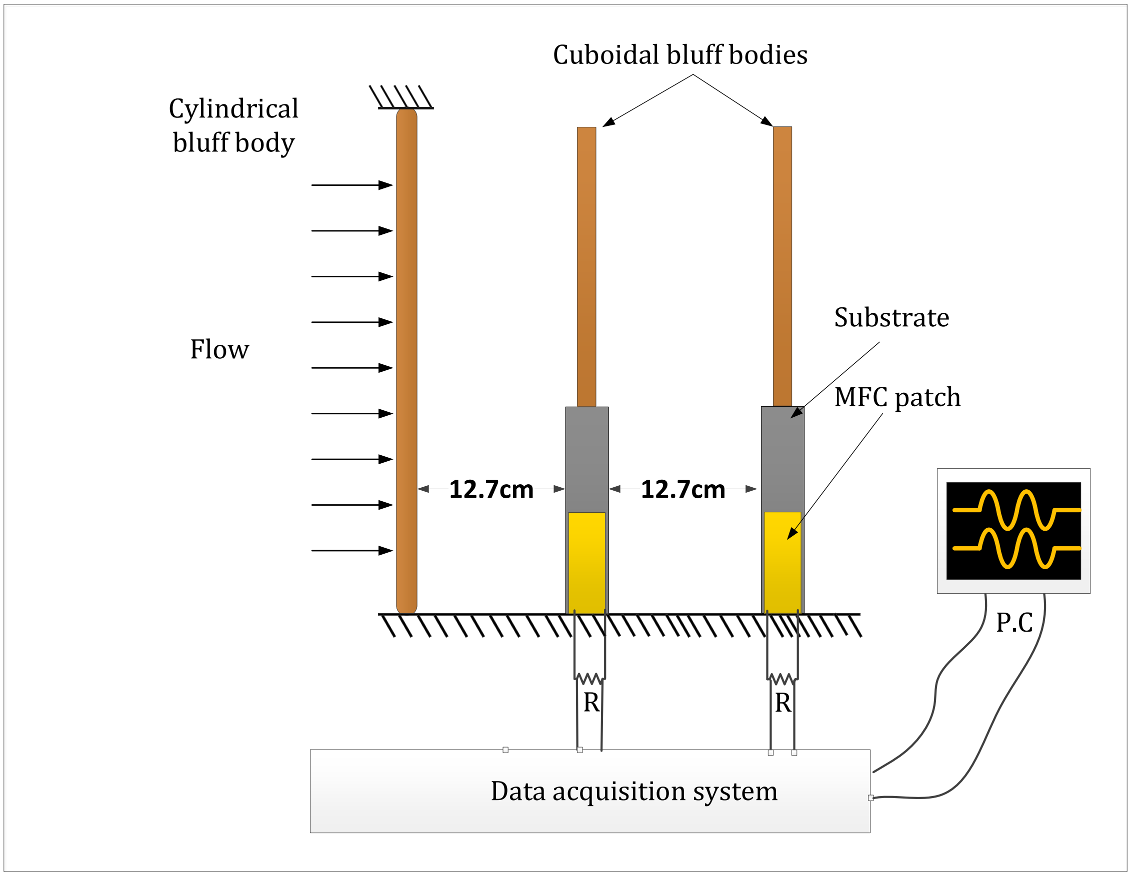

Figure 3.1: Schematic of the experimental setup.

3.3 Experimental results and discussion

The variation of the RMS of the harvested voltage with the Reynolds number, Re, is presented in Figure 3.2. The Reynolds number is defined as $U_\infty D/\nu$ where ν is the kinematic viscosity of the air. The plot shows a significant increase in the level of harvested voltage as the Reynolds number is increased from 1200 to 4573. Table 3.1 presents values of the harvested power, the frequency, and the dominant peaks of the spectra at the fundamental frequency Ω and its third superharmonic 3Ω over the same range of Reynolds numbers. The numbers show a nonlinear relation between the harvested power and the Reynolds number, which implies that the coefficients in the phenomenological model must depend on the Reynolds number. Furthermore, the ratio of the amplitudes of the fundamental and third harmonic frequency components is almost constant indicating that the coefficients must be related by this ratio.

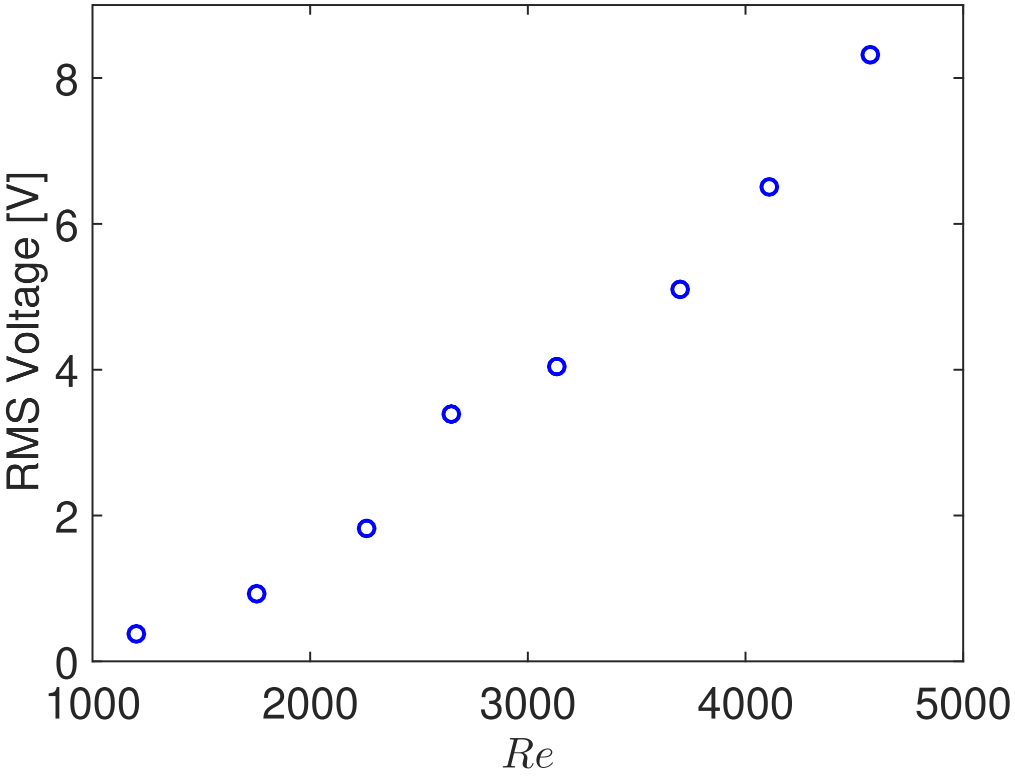

Figure 3.2: Variation of the RMS of harvested voltage with flow speed represented by the Reynolds number, Re.

Re	$Power[mW]$	$\Omega[rad/s]$	$V_\Omega[V]$	$V_3\Omega[V]$
1200	0.36	15.08	0.54	0.01
1755	2.09	15.08	1.29	0.03
2258	8.32	15.08	2.56	0.08
2650	28.75	15.08	4.71	0.14
3135	40.70	15.08	5.67	0.17
3700	64.96	15.08	7.17	0.19
4105	106.10	15.08	9.16	0.20
4573	172.77	15.08	11.68	0.20

Table 3.1: Harvested power, oscillation frequency and amplitudes of spectral peaks at the fundamental frequency and its third superharmonic as the Reynolds number is increased from 1200 to 4573.

Based on the damping characteristics, the voltage generated by the energy harvester, V, is modeled phenomenologically as a lumped parameter system given by

$$\ddot{V} + \Omega^2 V - \mu_l \dot{V} + \mu_2 \dot{V}|\dot{V}| = 0 \tag{3.4}$$

Here Ω, μ_l, and μ_2 are respectively the oscillation frequency, linear damping coefficient, and quadratic damping coefficient. The oscillation frequency is usually very close to the undamped natural frequency of the harvester. The linear damping term, $\mu_l \dot{V}$, accounts for the structural damping and electrical load resistance while the nonlinear damping term, $\mu_2 \dot{V}|\dot{V}|$, accounts for the aerodynamic drag and nonlinear piezoelectric response.

Although crucial, the influence of linear and nonlinear damping terms in equation 3.4 on the response is smaller than that of the inertia and stiffness terms. As such, the linear and nonlinear damping terms are scaled with a small non-dimensional parameter ϵ as $\mu_l = \epsilon \hat{\mu}_l$, and $\mu_2 = \epsilon\hat{\mu}_2$. Moreover, we note that the oscillations of the cuboidal cylinder, which is a consequence of its inertia and stiffness, occur at a much faster time scale than variations due to the damping terms. Subsequently, we complement the time scale, $t(\equiv T_0)$ with a slower time scale $\epsilon t(\equiv T_1)$ and solve equation 3.4 using the method of multiple scales, which yields the approximate solution [35–37]

$$V(t,\epsilon) = a(t,\epsilon)\cos[\Omega t + \beta] + \frac{a(t,\epsilon)^2\mu_2}{15\pi}\sin\left[3\Omega t + 3\beta\right] \tag{3.5a}$$

where the amplitude a is governed by

$$\dot{a}(t,\epsilon) = \frac{1}{2}\mu_l a(t,\epsilon) - \frac{4}{3\pi}a(t,\epsilon)^2\Omega\mu_2 \tag{3.5b}$$

with the dot representing differentiation with respect to time and β is a constant phase.

By imposing the steady state condition on equation 3.5b in conjunction with the approximate solution presented in equation 3.5a, we obtain

$$\mu_2 = 15\pi\frac{V_{3\Omega}}{V_{\Omega}^2}, \text{ and} \tag{3.6a}$$

$$\mu_l = \frac{8}{3\pi}\Omega\mu_2 V_{\Omega} \tag{3.6b}$$

where $V_{\Omega} = a_0$, and $V_{3\Omega} = a_0^2\mu_2/15\pi$; and a_0 is the steady state amplitude, which is the nontrivial fixed point of equation 3.5b.

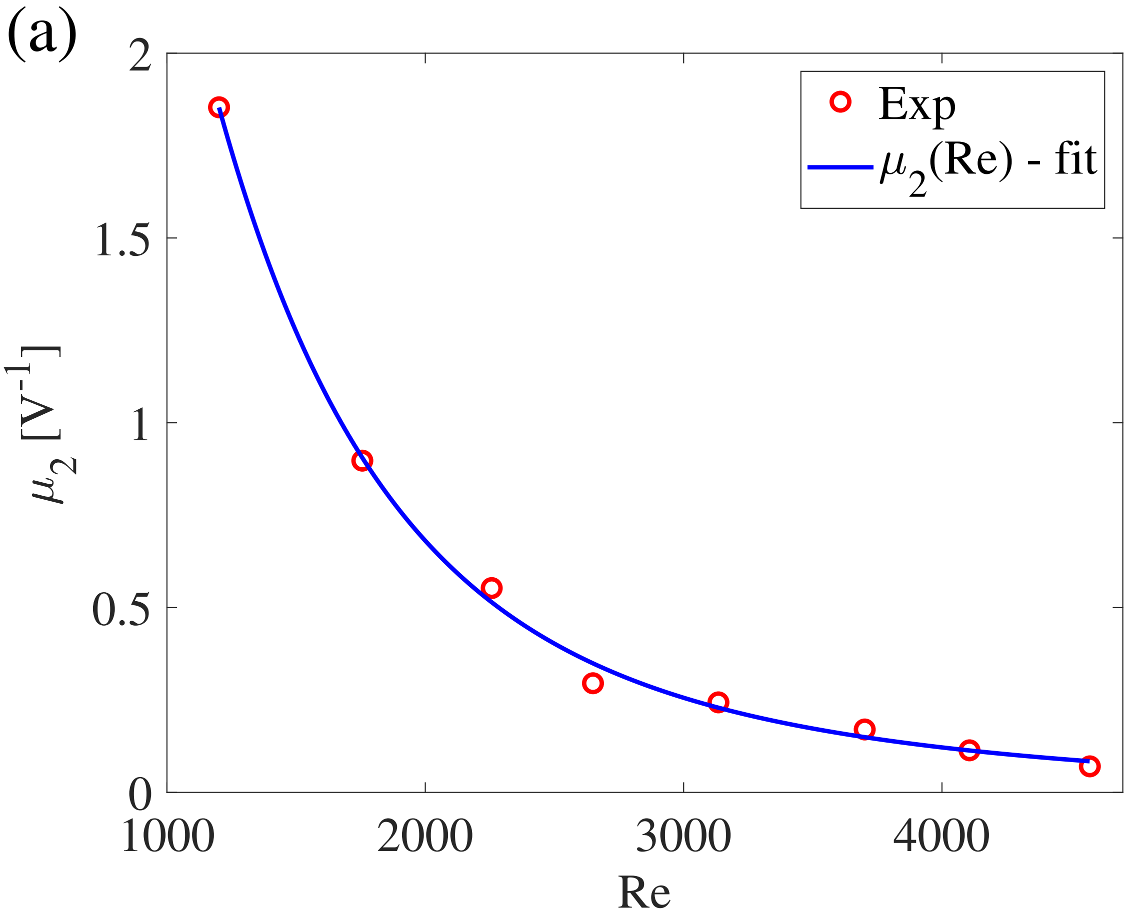

Figure 3.3: Variation of identified (a) quadratic damping coefficient μ_2, with the flow speed represented by the Reynolds number, Re. Expressions for the curve fits are respectively presented in equation 3.6a

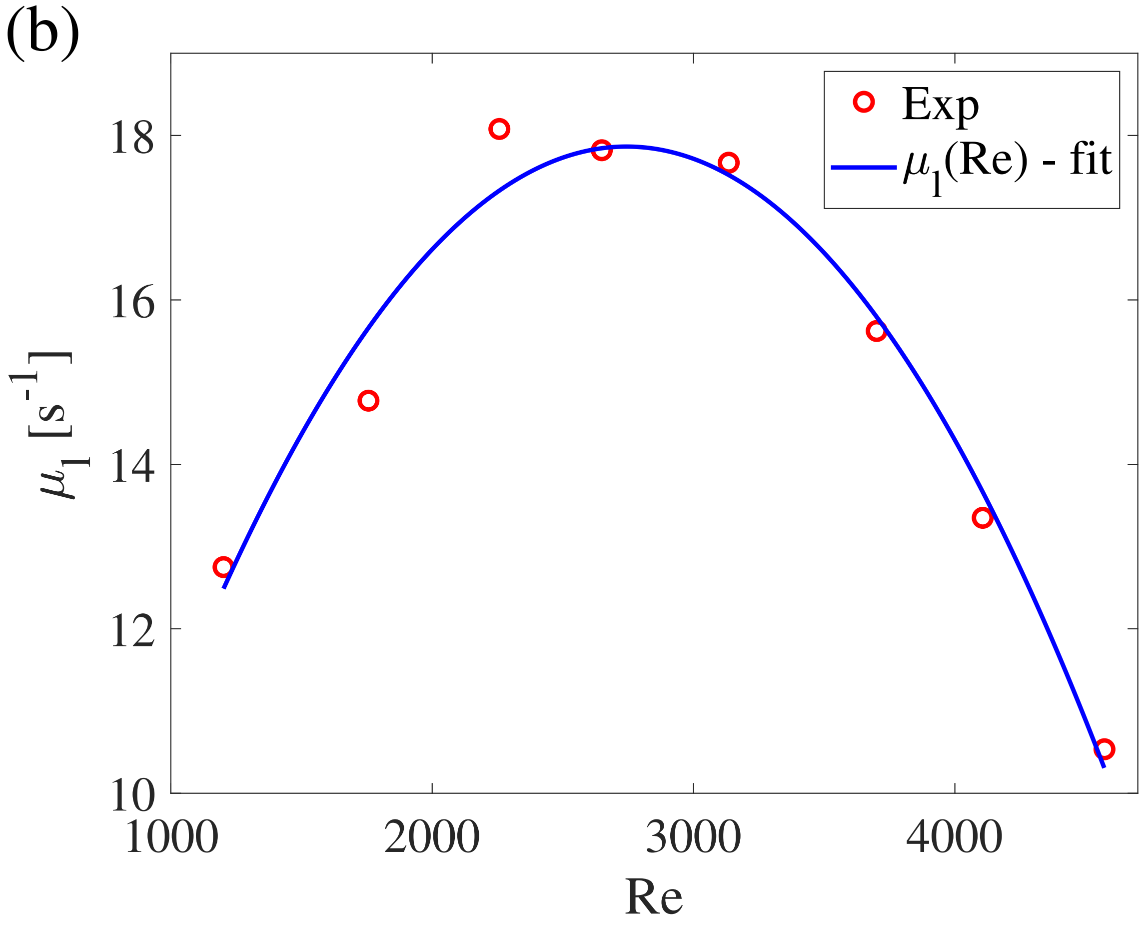

Figure 3.4: Variation of identified for linear damping coefficient μ_l, with the flow speed represented by the Reynolds number, Re. Expressions for the curve fits are respectively presented in equation 3.6b

The values presented in Table 3.1 and relations presented in equations 3.6a, and 3.6b are then used to identify μ_l, and μ_2 at different flow speeds or Re. The variation of the quadratic damping coefficient, μ_2, as a function of the Re is shown in figure 3.3. We note that the quadratic damping coefficient decreases exponentially as the Reynolds number is increased. This relation is given by the fitted empirical equation

$$\mu_2(Re) = 10.123 \times e^{-0.002Re} + 1.04 \times e^{-5.614\times10^{-4}Re} \tag{3.7}$$

Using equation 3.6b and the identified values of V_Ω, Ω, and μ_2, we evaluate the linear damping coefficient, μ_l which is presented in figure 3.4. Further, we obtain the empirical relation governing this variation as

$$\mu_l(Re) = -2.261 \times 10^{-6} \times Re^2 + 0.0124 \times Re + 0.843 \tag{3.8}$$

Re	1200	1755	2258	2650	3135	3700	4105	4573
$\mu_\mathbf{l}$ **[1/s]**	12.75	1 4.77	18.08	17.82	17.67	15.62	13.35	10.53
$\mu_\mathbf{2}$ **[1/V]**	1.85	0.90	0.55	0.30	0.24	0.17	0.11	0.07

Table 3.2: Identified linear and nonlinear damping coefficients from experimental data at different Reynolds numbers.

The efficacy of the proposed phenomenological model is validated by comparing time series and corresponding spectra obtained from experiments to those obtained by numerically integrating equation 3.4 using the coefficients mentioned in table 3.2. Figures [3.5-3.7] show agreement between measured and predicted time series with correlation levels larger than 0.99. This value drops to values between 0.95 and 0.90 when the comparison is carried over more than 25 periods. The percent difference between the measured and numerically predicted root mean square (RMS) values of the harvested voltage varies between 0% at Re = 1200 and a maximum value of 7.4% at Re = 3135 as shown in table 3.3. A comparison of the corresponding spectra presented in figures [3.8-3.10] shows that the model predicts the spectral amplitudes at Ω and 3Ω with differences that are less than 10% as shown in table 3.3. The larger differences of 9.1% and 9.4% are associated with 3Ω, whose amplitude is very small in comparison to that of the fundamental and, as such, does not impact the predicted RMS level much, especially for Re =1200. The sources of these differences include the turbulence intensity of the incident flow, which results in the background noise, and low-frequency variations in the flow that can be more pronounced at specific flow speeds.

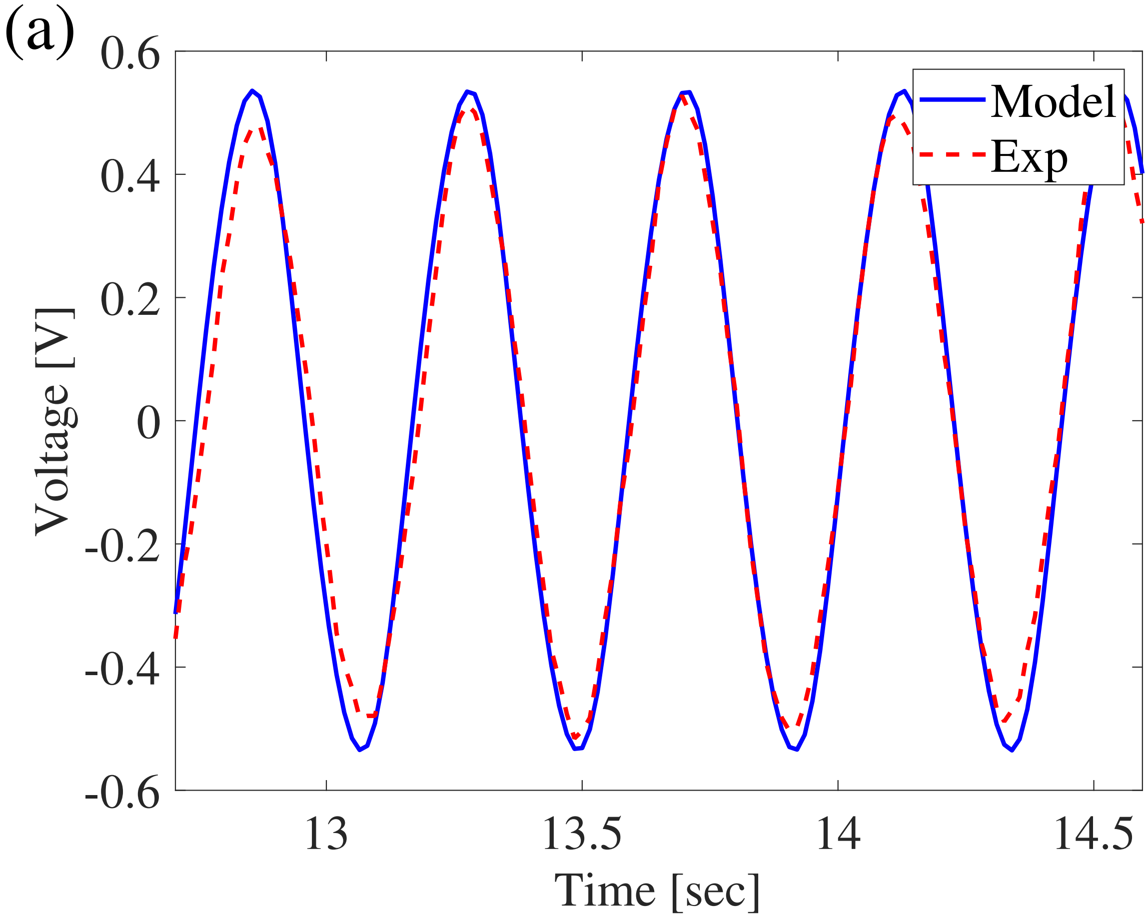

Figure 3.5: Comparison of measured time series of harvested voltage to those obtained by numerically integrating equation 3.4 using identified coefficients for (a) $Re = 1200$.

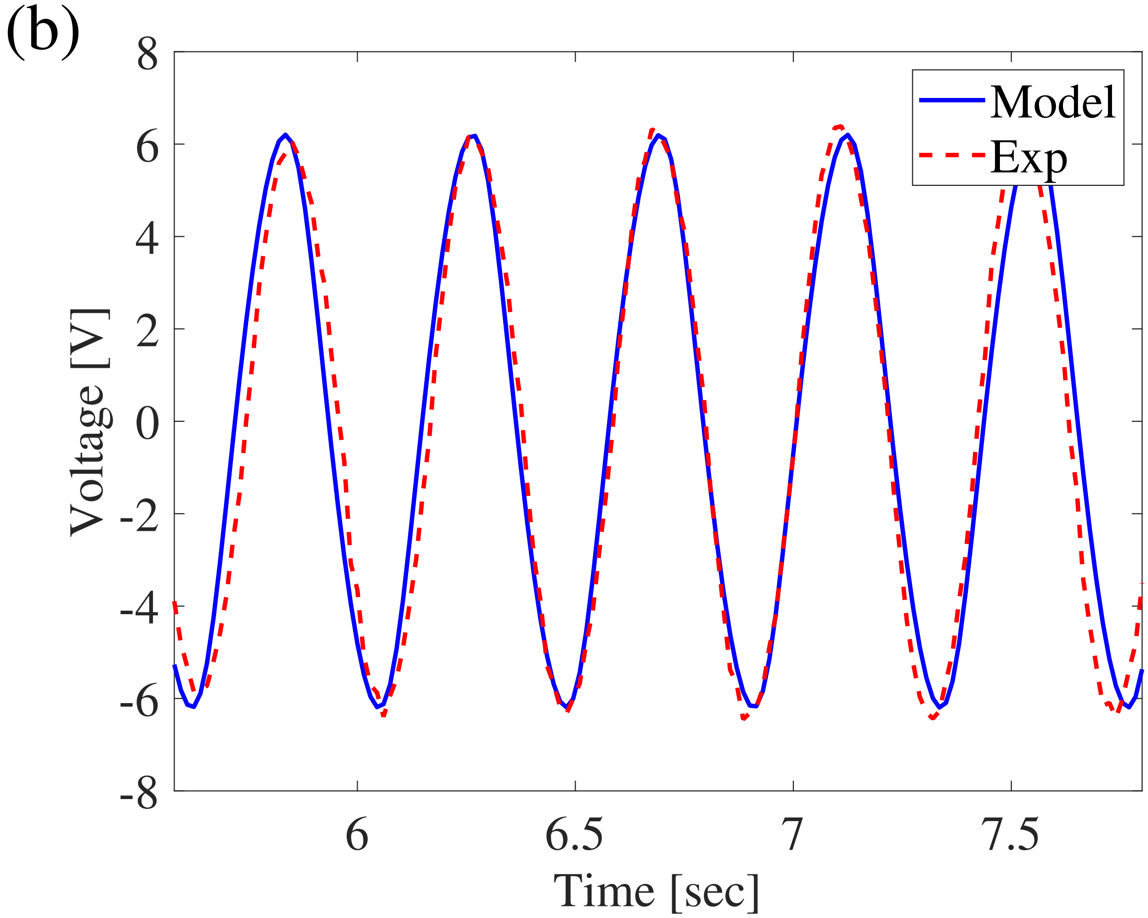

Figure 3.6: Comparison of measured time series of harvested voltage to those obtained by numerically integrating equation 3.4 using identified coefficients for $Re = 3135$,

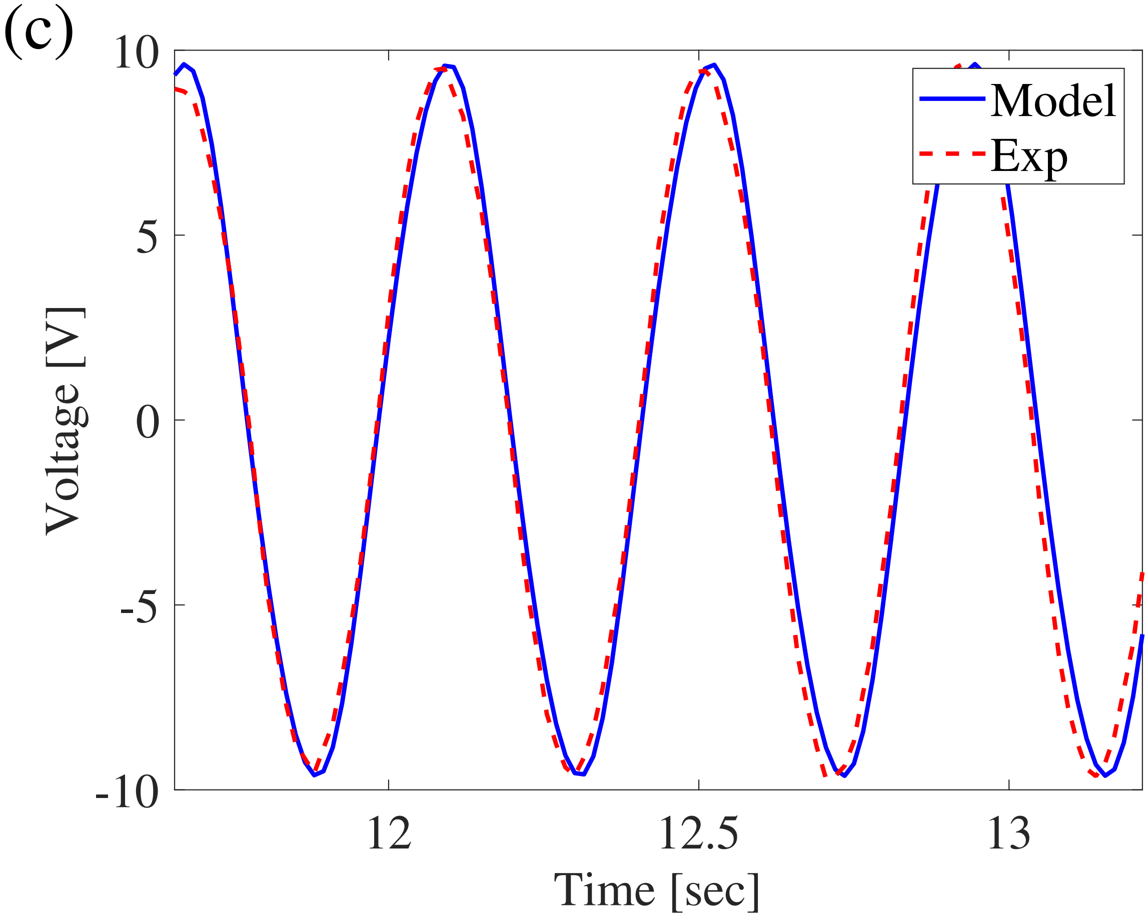

Figure 3.7: Comparison of measured time series of harvested voltage to those obtained by numerically integrating equation 3.4 using identified coefficients for $Re = 4105$.

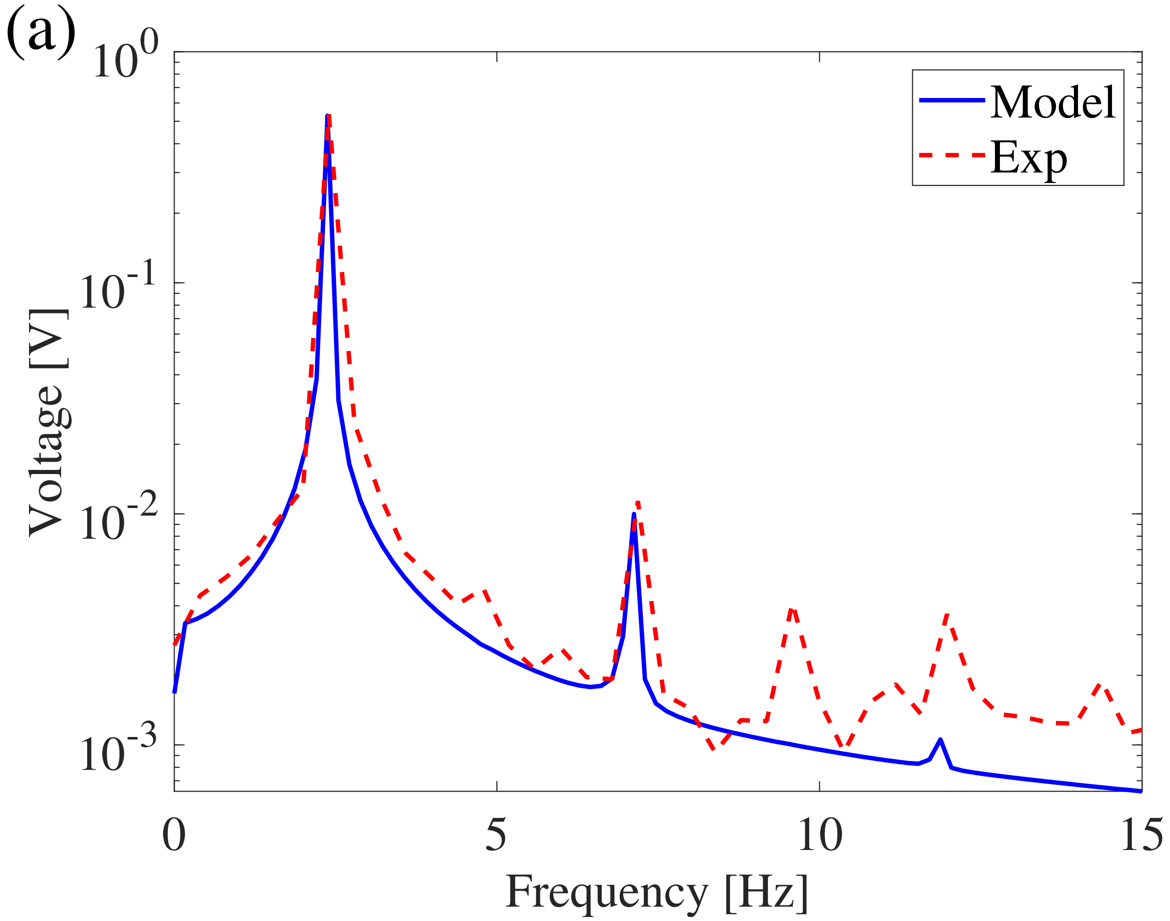

Figure 3.8: Comparison of model and experimental spectra for $Re = 1200$

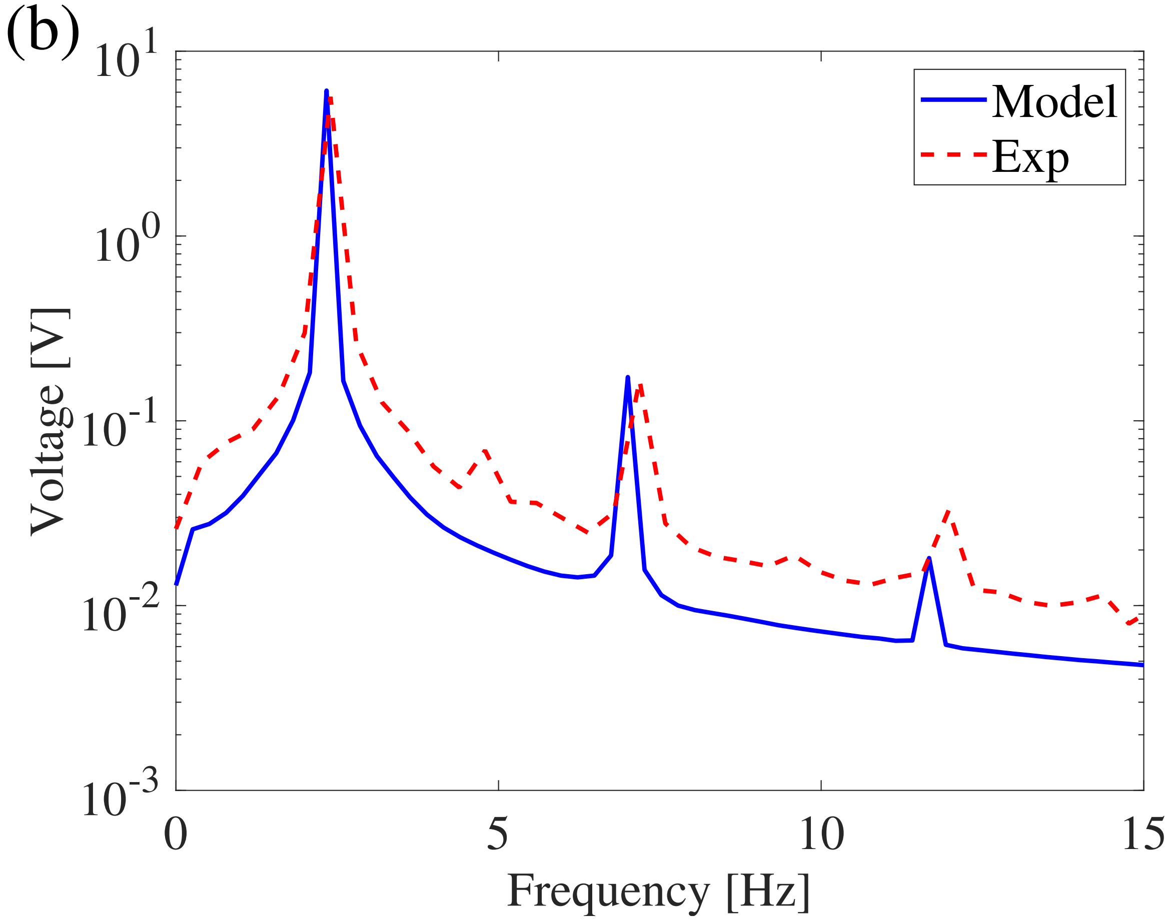

Figure 3.9: Comparison of model and experimental spectra for $Re = 3135$

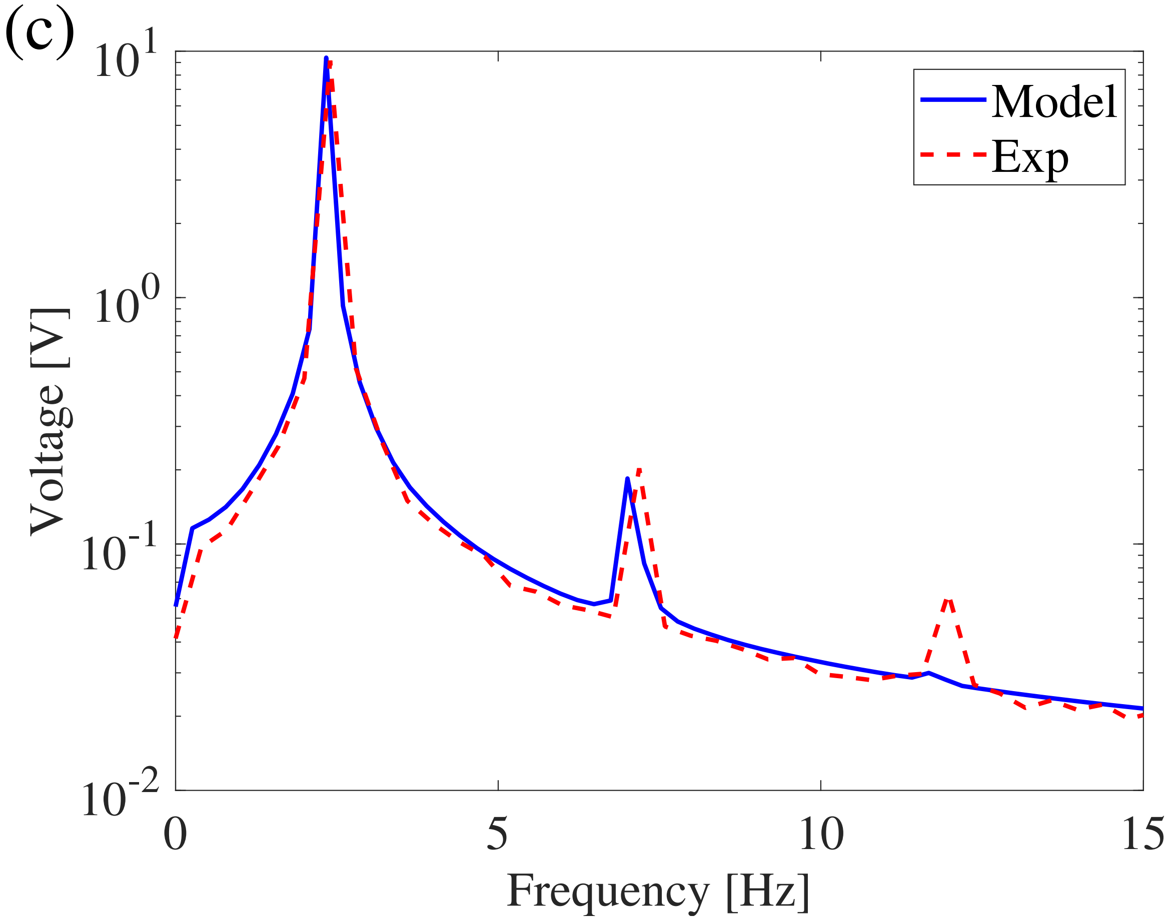

Figure 3.10: Comparison of model and experimental spectra for $Re = 4105$.

Re	**Exp.**			**Model**			**%difference**		
	$\mathbf{V_{RMS}}$ **[V]**	$\mathbf{V_{\Omega}}$ **[V]**	$\mathbf{V_{3\Omega}}$ **[mV]**	$\mathbf{V_{RMS}}$ **[V]**	$\mathbf{V_{\Omega}}$ **[V]**	$\mathbf{V_{3\Omega}}$ **[mV]**	$\mathbf{V_{RMS}}$	$\mathbf{V_{\Omega}}$	$\mathbf{V_{3\Omega}}$
1200	0.38	0.54	11	0.38	0.53	10	0	-1.9	-9.1
3135	4.04	5.68	166	4.34	6.12	172	7.4	7.8	3.6
4105	6.51	9.16	203	6.75	9.42	184	3.6	2.8	9.4

Table 3.3: Comparison of of model and experimental RMS and spectral amplitudes values at Ω and 3Ω.

3.4 Conclusions

We experimentally demonstrated that voltage harvested from wake galloping energy - a complicated multiphysics phenomena dealing with aerodynamics, aero-elasticity, and piezoelectricity - can be represented using a single nonlinear ordinary differential equation. Linear and nonlinear damping terms were used to represent physical characteristics related the galloping phenomena. By modeling the variations of linear and quadratic damping terms with the flow speed one can accurately determine the harvested voltage.

Chapter 4

Simulations of flow past a circular cylinder and interference between two cylinders in tandem

4.1 Introduction

Technological advancements of low power electronics have revolutionized the research and development of sensors, which have a wide range of applications including surveillance systems, structural stems for health monitoring, networks of remote sensing, and devices for monitoring the environmental changes, Priya et al. [38]. To make the sensors self sufficient (autonomous), piezoelectric materials are proposed as the power sources due to their ease of integration into a system and their ability to readily convert the ambient energy into usable electrical energy, Sodano et al. and Anton et al. [3, 39]. Again, harvesting energy from fluid flows at low pace is appropriate in many applications which include the deployment of self-powered sensors or batteries in homes, rivers, and airstreams. Latest research have focused on the conversion of aeroelastic vibrations in airfoil sections to electric power. Piezoelectric energy harvesting from wind has been of tremendous research interest as the wind energy is abundantly available and it can induce large strains in the system which are generally unavailable from ambient sources, Truitt et al., Abdelkefi et al., and Orrego et al. [40–42].

The study of single or a group of circular cylinders in cross-flow has attracted significant attention in recent decades. Perhaps, the flow over a circular cylinder is the most investigated problem in configuration fluid mechanics, and the interest in that flow continued in recent decades. It is a simple shape but a complex flow field. The flow over a circular cylinder is a useful model for different engineering applications, including flow around tall buildings, offshore structures, transmission cables, cooling towers, etc. Researchers have investigated the flow over a single or a pair of cylinders, numerically and experimentally. Sourabh et al. [43] simulated flow over a stationary circular cylinder at wide range of Reynolds number, 100 to 1000. They predicted and summarized drag coefficient, , Strouhal number, and compared numerical results with experimental data. Chloe et al. [44] computed drag coefficient, lift coefficient, and Strouhal number for flow past a circular cylinder at Re 100, Re=200 and $Re = 1000$. Nayfeh et al. [34] numerically studied 2D flow over a fixed cylinder for different values of Reynolds numbers and calculated lift and drag. Akhtar [45] simulated the flow past a circular cylinder at fixed Reynolds numbers 525. He obtained good agreement with published computational results for fluctuating lift coefficient, mean drag coefficient, and Strouhal number. Mittal et al. [46] conducted a numerical studies for flow over a single cylinder, and staggered and tandem cylinders for various spacing $2d - 5d$ at Reynolds number of 100 and 1000. They compared the results to other researchers results for the mean drag coefficient and the Strouhal number. Also, they predicted that two cylinders show a strong dependence on the Reynolds number compared with the flows past a single cylinder. Sharman et al. [47] reported the mean and fluctuating lift and drag coefficients for cylinders in tandem for center-to-center cylinder spacing between 2 and 10 diameters. The strong interference between cylinders happens for spacing between 3.75 and 4 for Reynolds number of Re=100. Meneghini et al. [48] obtained results for flow past a pair of circulars cylinders for Reynolds number from $Re = 100$ to $Re = 200$. The gab center to center was chosen in the range $(1.5d - 4d)$. They calculated the average drag coefficient and Strouhal number for four difference gabs.

Our aim in this chapter is to validate the computational model for flow over a circular cylinder. We solve the unsteady incompressible Navier-Stokes equations using ANSYS-FLUENT software. We will investigate in detail the flow at two Reynolds numbers $Re = 525$ and $Re = 1000$, and compare lift amplitude fluctuation C_L, the mean drag coefficient C_D, and Strouhal number for vortex shedding with published results. because our energy harvesting model is made of two cylinders in tandem, we will compute the flow over such an arrangement. We consider a square cylinder placed in the wake of circular cylinder, and the study the effects of the separation distance on the unsteady lift on the square cylinder.

4.2 Two-dimensional flow over a circular cylinder

Accurate resolution of the wake of the circular cylinder is a basic requirement in the development of the present model because of the interaction between the generated vortices in its wake the energy harvesting square cylinder. In this study, we solve the unsteady incompressible Navier-Stokes equations using ANSYS-FLUENT software (version 17.2). In this section, we will investigate in detail the flow over a single cylinder at two Reynolds Re=525 and Re= 1000. To validate our simulations, we compare unsteady lift amplitude C_L, the mean drag coefficient C_D, and Strouhal number for vortex shedding St with published data by other researchers.

4.2.1 Governing equations

We assume unsteady incompressible two-dimensional flow, and solve numerically the unsteady Navier-Stokes equations. We limit our study to low Reynolds number, and use fine grid to resolve all the two-dimensional motion scales. Thus no turbulence model is activated in the simulations. The equations for continuity and momentum may be expressed as follows:

Continuity :

$$\frac{\partial u}{\partial x} + \frac{\partial v}{\partial y} = 0 \tag{4.1}$$

Momentum:

$$\frac{\partial u}{\partial t} + u\frac{\partial u}{\partial x} + v\frac{\partial u}{\partial y} = -\frac{1}{\rho}\frac{\partial p}{\partial x} + \nu\left(\frac{\partial^2 u}{\partial x^2} + \frac{\partial^2 u}{\partial y^2}\right) \tag{4.2}$$

$$\frac{\partial v}{\partial t} + u\frac{\partial v}{\partial x} + v\frac{\partial v}{\partial y} = -\frac{1}{\rho}\frac{\partial p}{\partial y} + \nu\left(\frac{\partial^2 v}{\partial x^2} + \frac{\partial^2 v}{\partial y^2}\right) \tag{4.3}$$

where $\nu = \mu/\rho$ is the kinematic viscosity.

Nondimensional Variables

We use the cylinder diameter d, free stream velocity U, pressure ρU^2, time d/U as a reference length, velocity, pressure, and time, respectively. In non-dimensional form, the equations become

$$\frac{\partial u}{\partial x} + \frac{\partial v}{\partial y} = 0 \tag{4.4}$$

$$\frac{\partial u}{\partial t} + u\frac{\partial u}{\partial x} + v\frac{\partial u}{\partial y} = -\frac{\partial p}{\partial x} + \frac{1}{Re}\left(\frac{\partial^2 u}{\partial x^2} + \frac{\partial^2 u}{\partial y^2}\right) \tag{4.5}$$

$$\frac{\partial v}{\partial t} + u\frac{\partial v}{\partial x} + v\frac{\partial v}{\partial y} = -\frac{\partial p}{\partial y} + \frac{1}{Re}\left(\frac{\partial^2 v}{\partial x^2} + \frac{\partial^2 v}{\partial y^2}\right) \tag{4.6}$$

where $Re = Ud/\nu$ is the Reynolds number.

4.2.2 Computational domain and boundary conditions

Numerical solutions are obtained on a finite domain around the cylinder. The extent of the computational domain has significant impact on the behavior of the flow, both in steady and unsteady simulations. In the current work, a computational domain is a rectangle of dimensions $51d \times 40d$ is used as Figure 4.1, it is sufficiently large to reduced the disturbance caused by farfield boundary conditions. The origin is taken at the the center of the circular cylinder. The upstream boundary is at $x = -20.5d$, and the downstream boundary is at $x = 30.5d$. On the upstream boundary the velocity is prescribed $u = 1$ and $v = 0$, which known as inlet boundary in the Fluent software. On the downstream boundary, the pressure is prescribed, which known as pressure outlet in Fluent. On the side boundaries at $y = 20.5d$, symmetry conditions are applied.

They are challenge to Create a high-quality mesh and is one of the most critical factors that must be considered to ensure simulation accuracy.Figure 4.2 shows block structure mesh which we used it in out simulation and compare to other previously published numerical results.

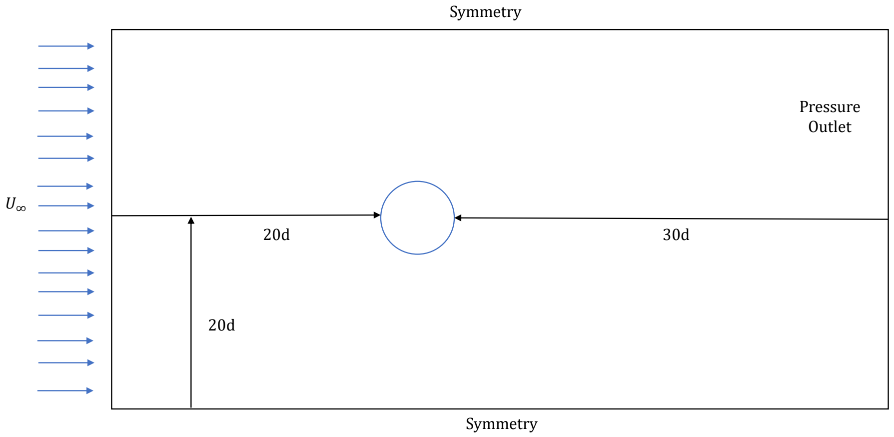

Figure 4.1: Computational domain and boundary conditions.

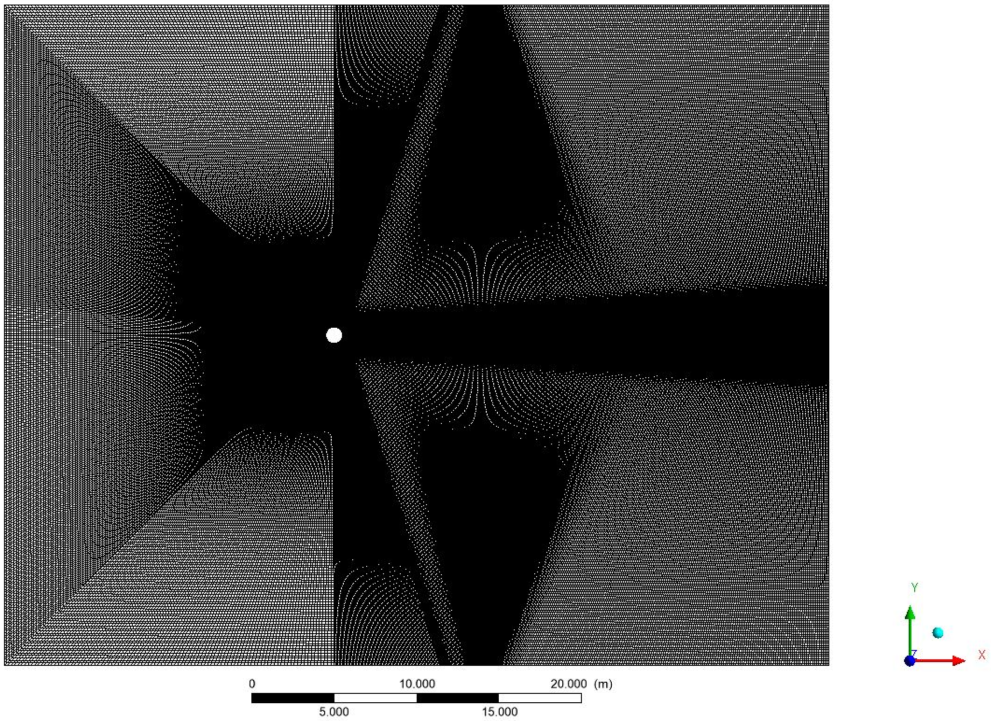

Figure 4.2: Block structured mesh one cylinder with Total nodes 200843

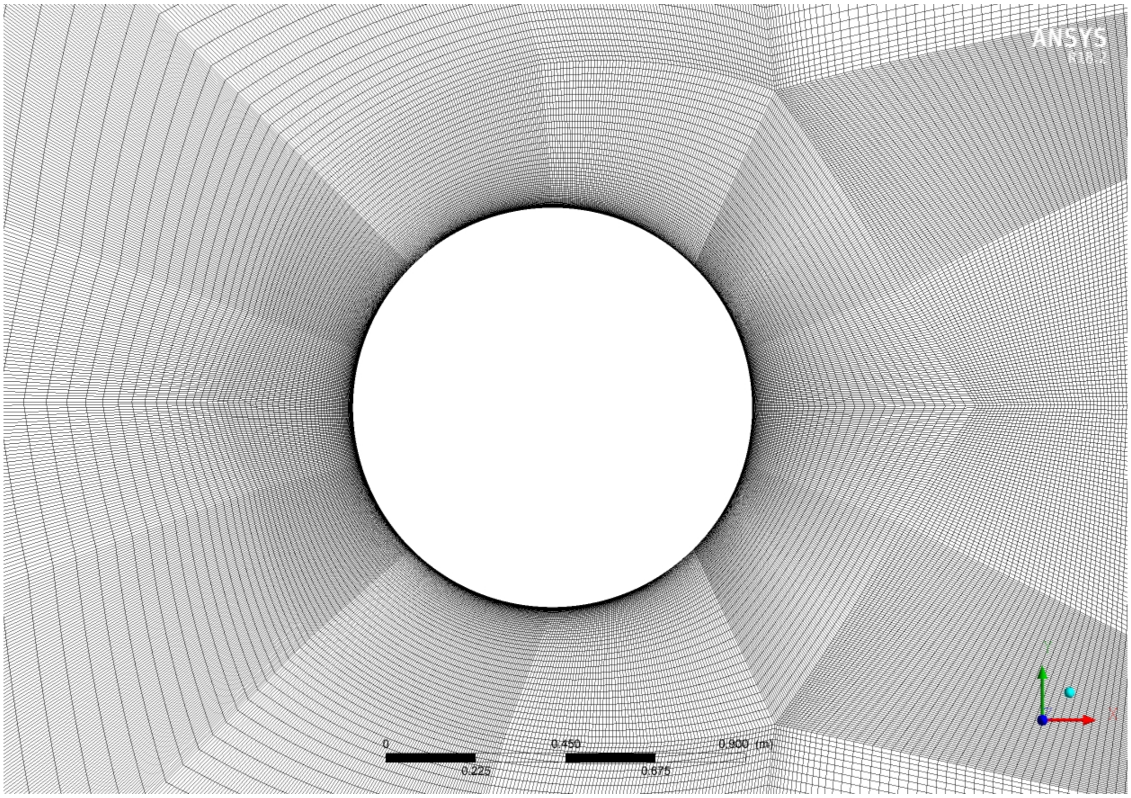

Figure 4.3: Zoomed-in view of the mesh around circular cylinder

4.2.3 Numerical results and discussion

First, we present results for $Re = 1000$. Figure (4.4) is a snap shot of the vorticity contours, which shows a typical von Karman vortex wake. The lift, drag and Strouhal number are defined by

$$C_L = \frac{L}{\frac{1}{2}\rho U^2 d} \tag{4.7}$$

$$C_D = \frac{D}{\frac{1}{2}\rho U^2 d} \tag{4.8}$$

$$St = \frac{f_o d}{U} \tag{4.9}$$

where L and D denote lift and drag, St is the Strouhal number, and f_o is vortex shedding frequency which is calculated from spectral analysis of unsteady lift. The time history of unsteady lift and drag coefficients are depicted in Figures (4.5) and (4.6). The power spectrum density of lift coefficient against frequency fd/U is depicted in Figure (4.7). Due to flow separation and formation of shed vortices in the cylinder wake, unsteady pressure distribution occurs on the cylinder surface. The non-uniform pressure distribution on the cylinder wall results in a fluctuation in the lift and drag acting on the cylinder. The spectral analysis of the periodic lift shows a dominant frequency f_o, and superharmonics at $3f_o$ and $5f_o$. The Strouhal number is considred to be the fundamental frequency f_o.

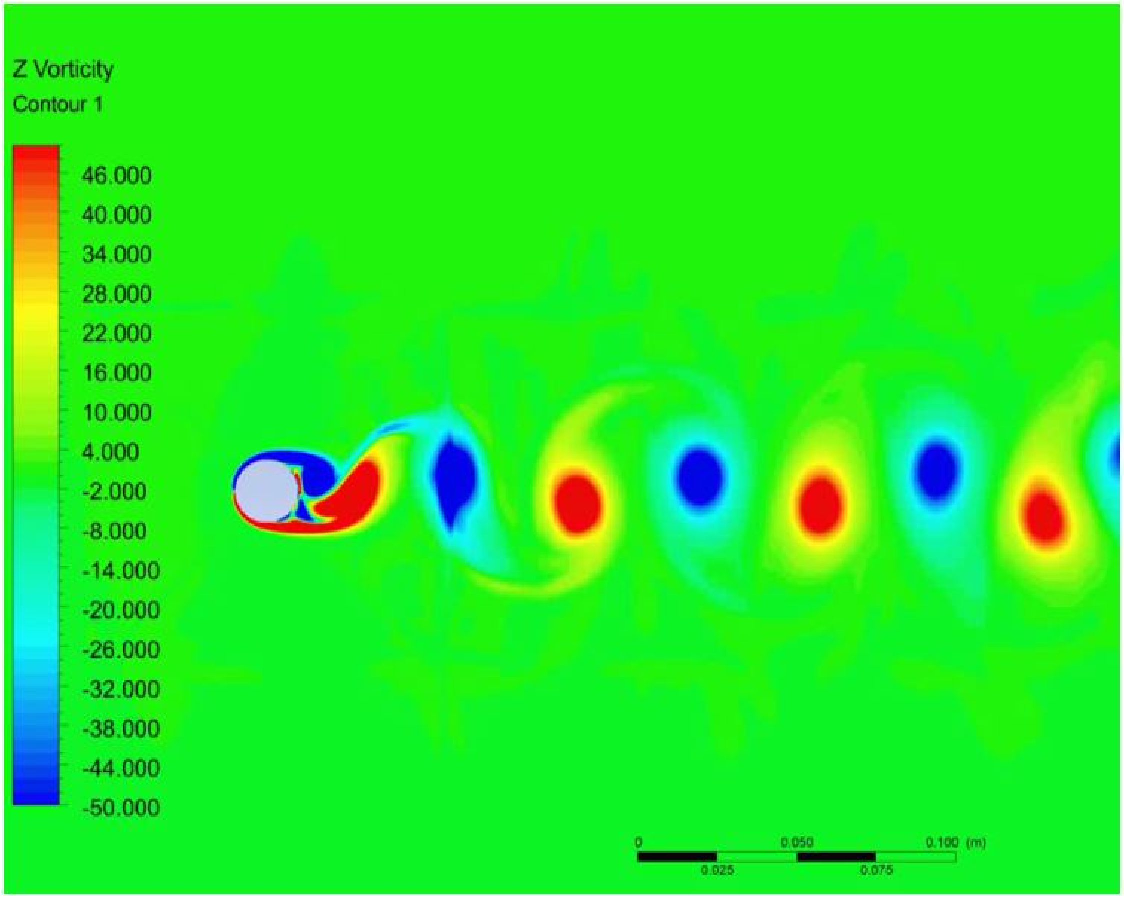

Figure 4.4: Reynolds $Re = 1000$. Vorticitiy contours.

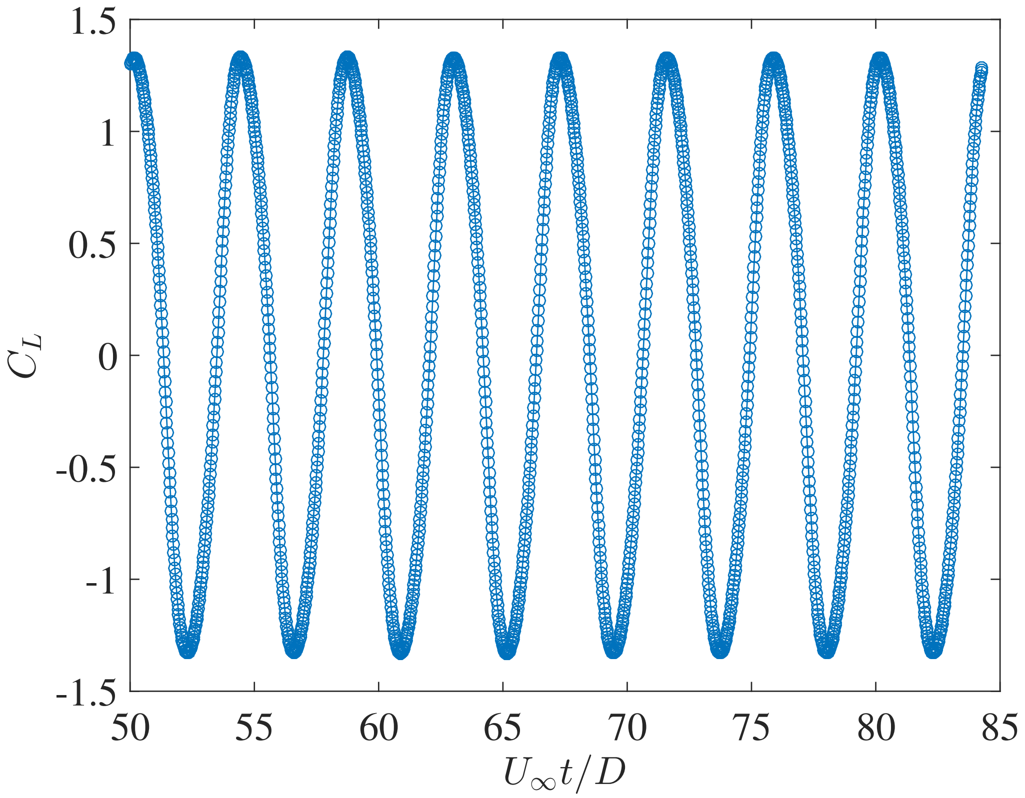

Figure 4.5: Flow at $Re = 1000$ for fluctuating lift coefficient

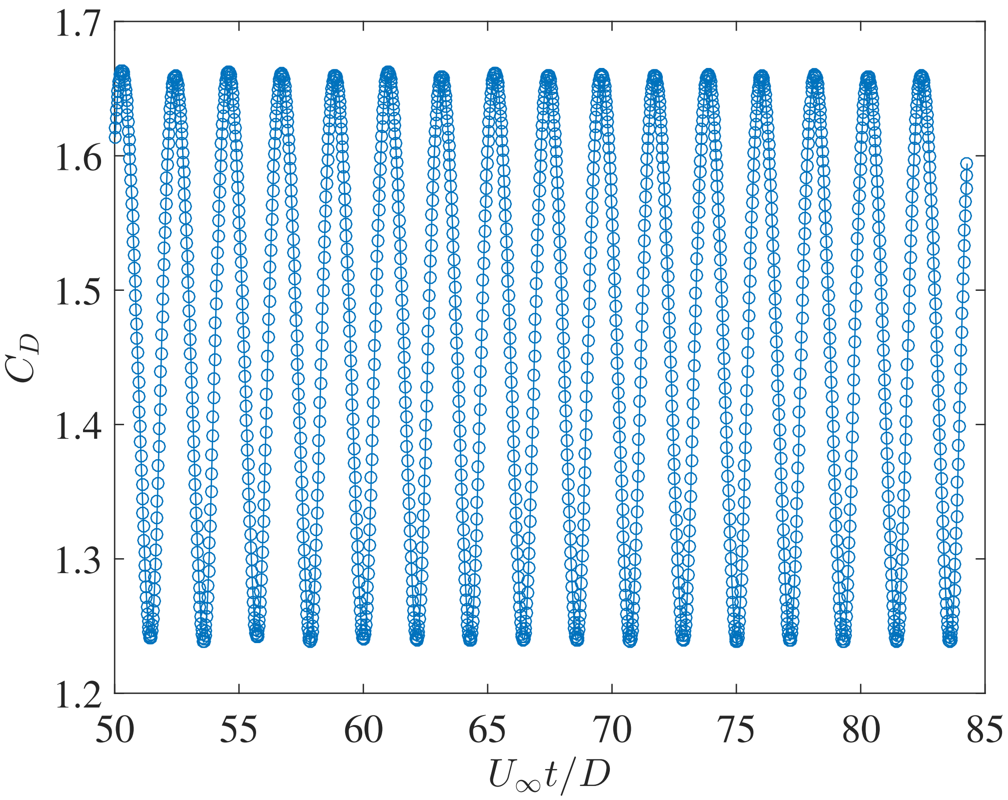

Figure 4.6: Flow at $Re = 1000$ for fluctuating drag coefficient

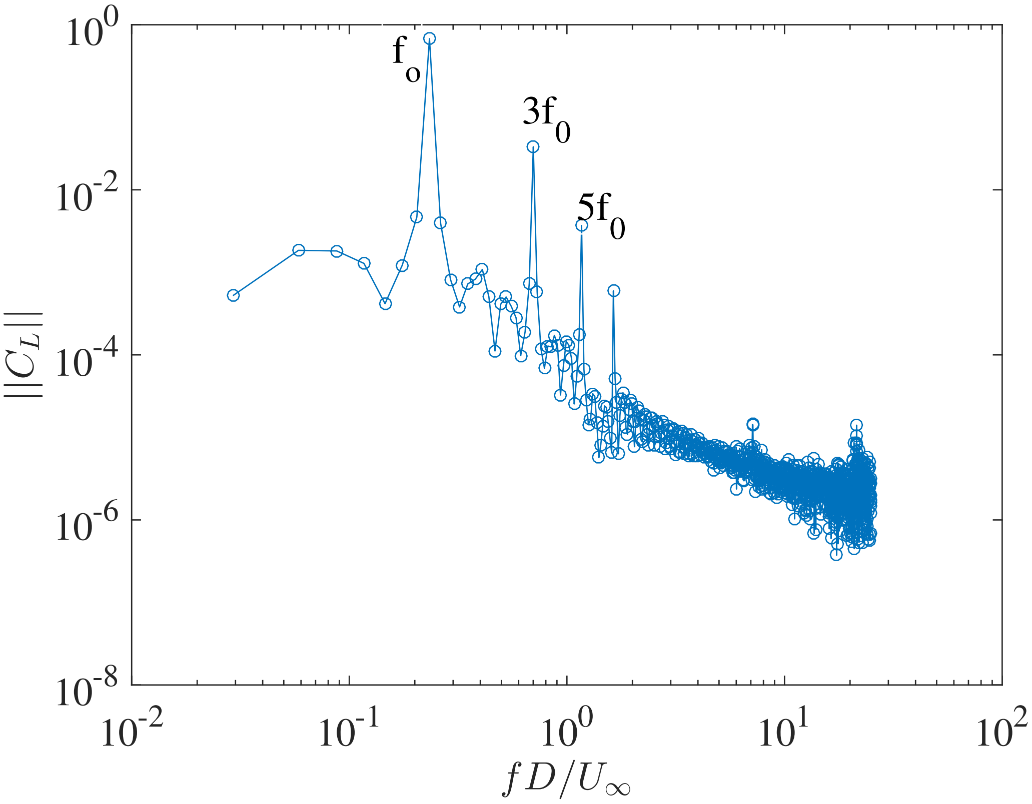

Figure 4.7: Flow at $Re = 1000$ for lift spectrum

Validation

To validate the simulations, we have computed the fluctuating lift coefficient amplitude, and mean drag coefficient at Re=525 and Re= 1000. As shown in Tables 4.1 and 4.2, present results are in good agreement with previously published numerical results by Apte et al. [43], Mittal et al. [46], Mimeau et al. [44], and Akhtar [45].

Re=525			
Source	St	C_L	C_D
Mittal et al. 1995	0.22	1.21	1.44
Imran Akhtar 2004	0.225	1.183	1.145
Present	0.216	1.2035	1.34

Table 4.1: Comparison of Strouhal number St, fluctuating lift coefficient amplitude, and mean drag coefficient at Re=525.

Re=1000			
Source	St	C_L	C_D
Mittal et al. 1995	0.231	1.65	1.48
Mimeau et al. 2015	0.245	1.54	1.51
Apte et al. 2008	0.238	1.36	1.5
Present	0.237	1.364	1.511

Table 4.2: Comparison of Strouhal number, fluctuating lift coefficient amplitude, and mean drag coefficient at Re=1000

4.3 Flow over a circular cylinder in tandem with a square cylinder

The fluid-structural model is two dimensional. The structural model is composed of two cylinders placed in tandem in an otherwise a uniform stream. A square cylinder is placed in the wake of a circular cylinder; both cylinders are fixed. To achieve good resolution of the vortex dominated wakes of the cylinders, the study is limited to a low Reynolds number of 1000 for the circular cylinder.

4.3.1 Computational domain and mesh

The computational domain is very similar to that used for flow over a single circular cylinder at $Re = 1642$. The diameter of the circular cylinder is d and the side of square cylinder is $0.75d$. The separation distance between the centers of the two cylinders is s. The cylinders are placed in a uniform flow. The schematic diagram of the flow model is given in Figure (4.8). The computational domain is $50d$ in the streamwise direction and $40d$ in the cross-stream direction. Figures (4.9-4.11) show block-structured mesh around the cylinders, and the total number of nodes is 438732. Computations are carried out for five values of the separation distance $s = 2d, 3d, 4d, 5d$ and $6d$.

A constant time step $\Delta t = 0.02$ is used for all calculations. The number of sub-iterations is at a maximum of 20. The transient scheme is second-order implicit Euler. The pressure scheme is SIMPLE, and second order in space. The momentum equations are discretized in space by the second order upwind scheme. The residual of continuity equation is set as Conference in each time step is monitored for Residual monitors for continuity as 10^{-5}.

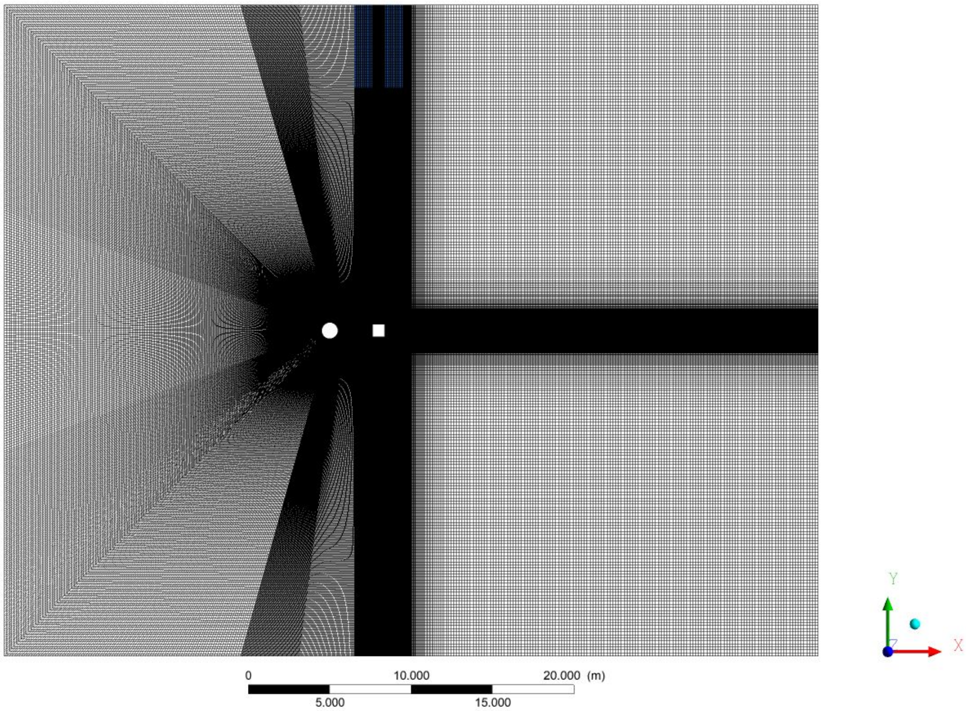

Figure 4.8: Computational mesh used for two cylinders in tandem arrangement with total number of nodes is 438732

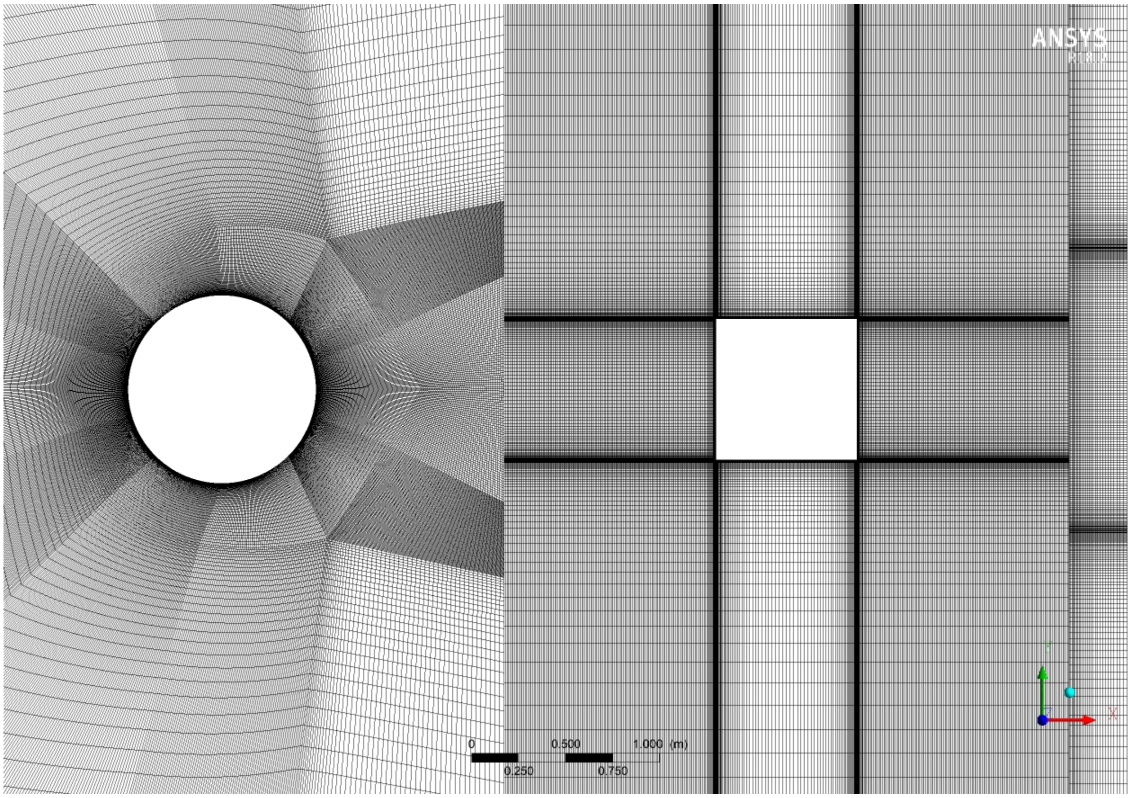

Figure 4.9: Zoomed-in view of the mesh around two cylinders

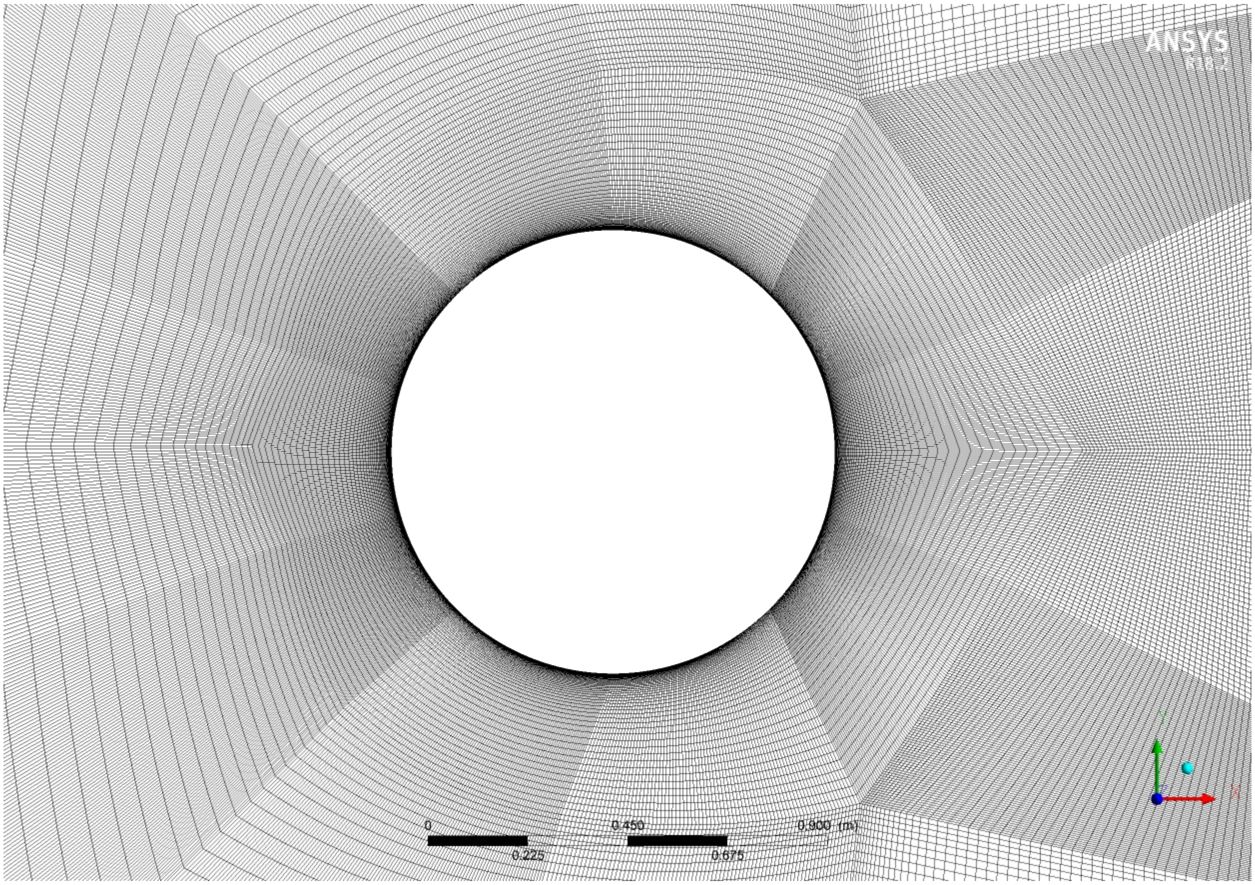

Figure 4.10: Zoomed-in view of the mesh around circular cylinder

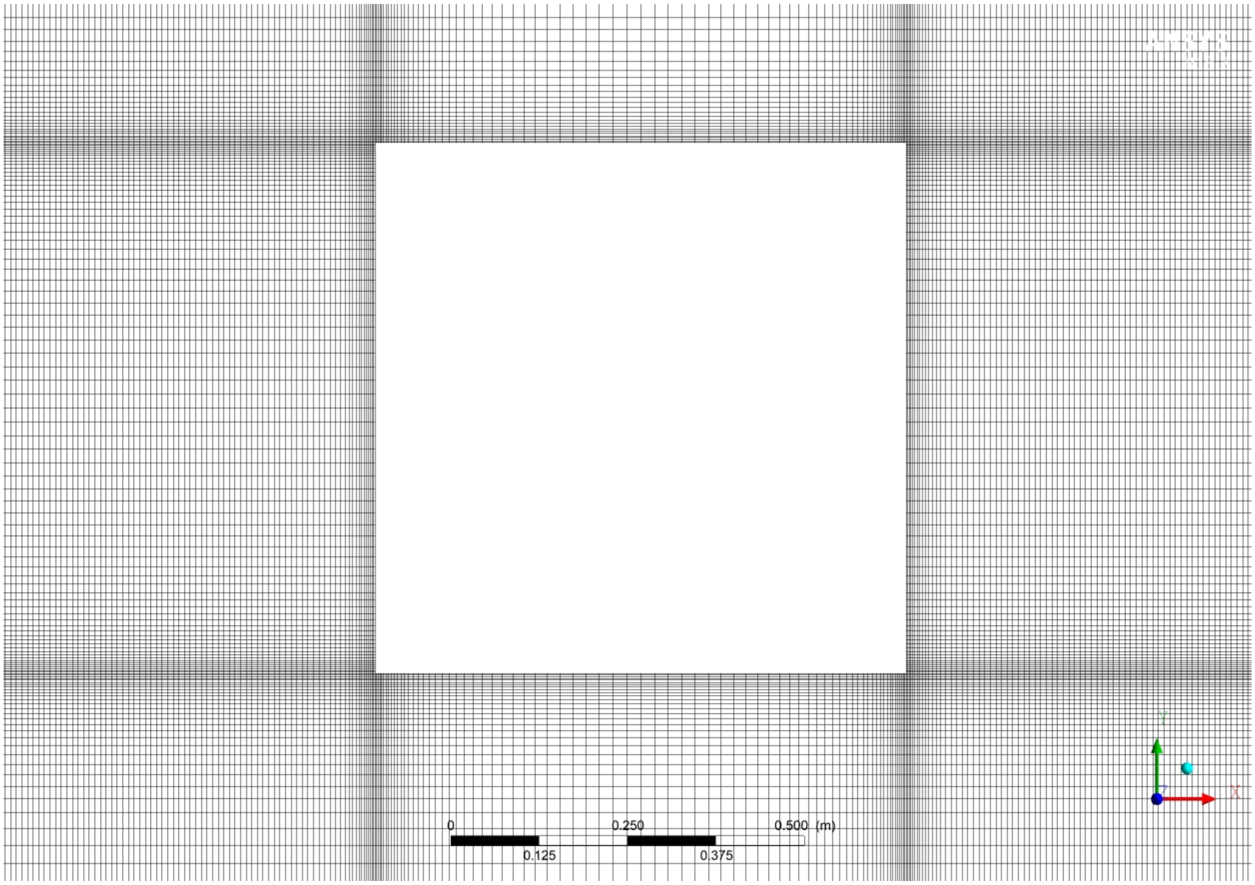

Figure 4.11: Zoomed-in view of the mesh around square cylinder

4.3.2 Results: lift and drag coefficients, and strouhal number

The Reynolds number of the circular cylinder is 1642. Snap shots of vorticity contours are shown in Figures 4.12-4.16 for different spacing s, which vary from $2d$ to $6d$. The red and blue colors represent positive and negative vorticity, respectively. Figure 4.12 for $s = 2d$ shows that the separated shear layers from the circular cylinder impinge on the square cylinder before their roll up into vortices is completed. The two cylinders appear to act as one long bluff body, and there is no distinct wake for the circular cylinder. For separation distance $s \geq 3d$, the separated shear layers from the circular cylinder roll up and impinge on the square cylinder as shown in Figures 4.13-4.16. The interaction of the circular cylinder vortices with the square cylinder produces vorticity of opposite sign.

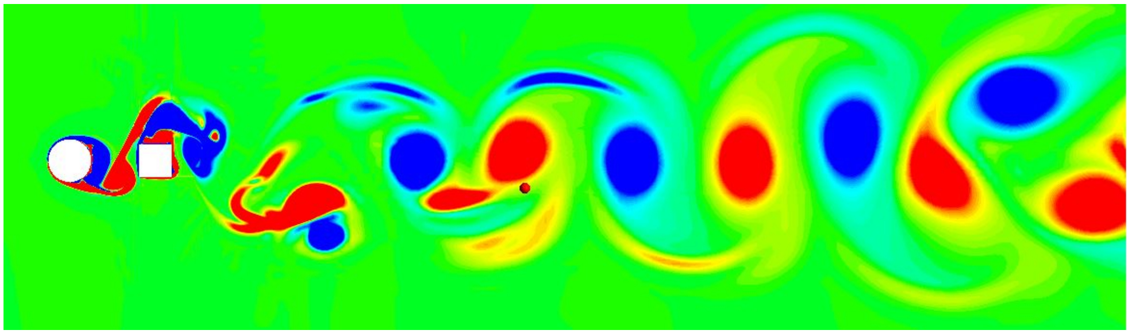

Figure 4.12: Vorticity contours for separation between the cylinders $2d$.

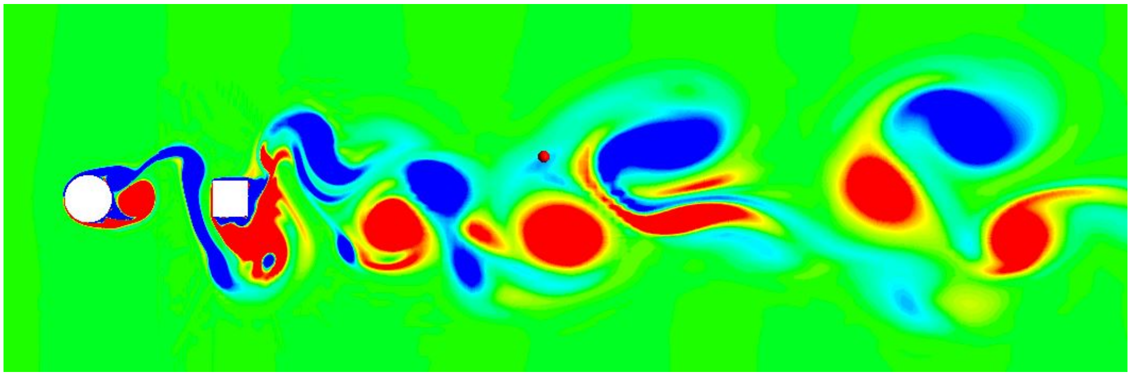

Figure 4.13: Vorticity contours for separation between the cylinders $3d$.

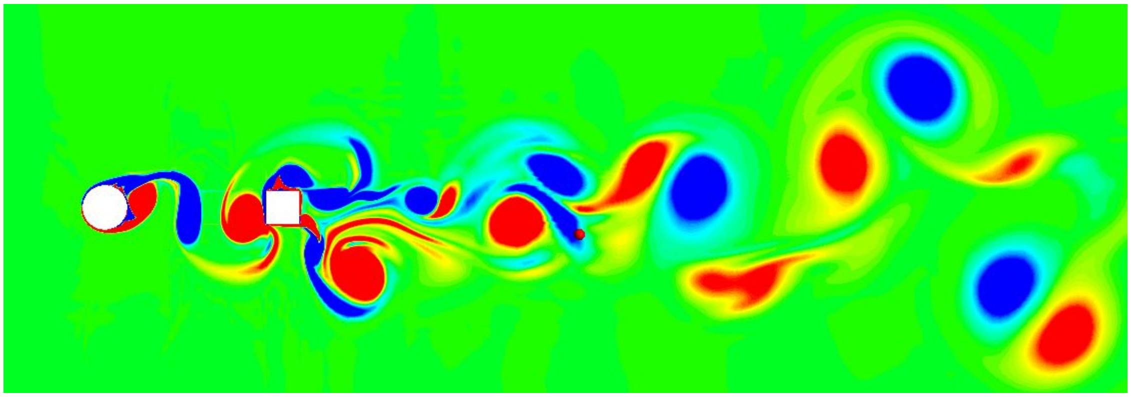

Figure 4.14: Vorticity contours for separation between the cylinders $4d$.

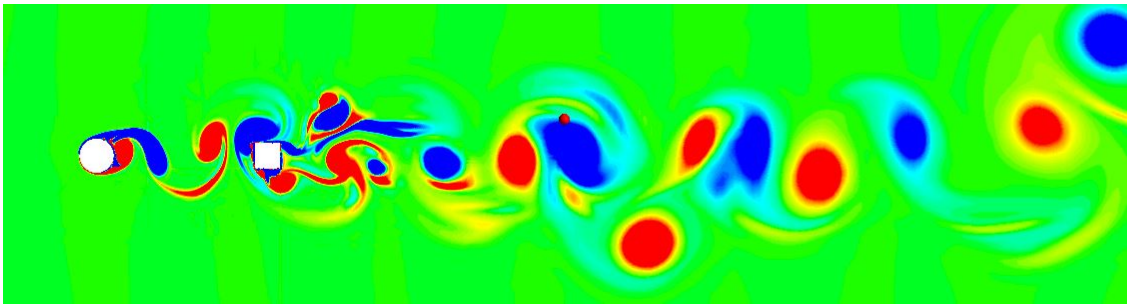

Figure 4.15: Vorticity contours for separation between the cylinders $5d$.

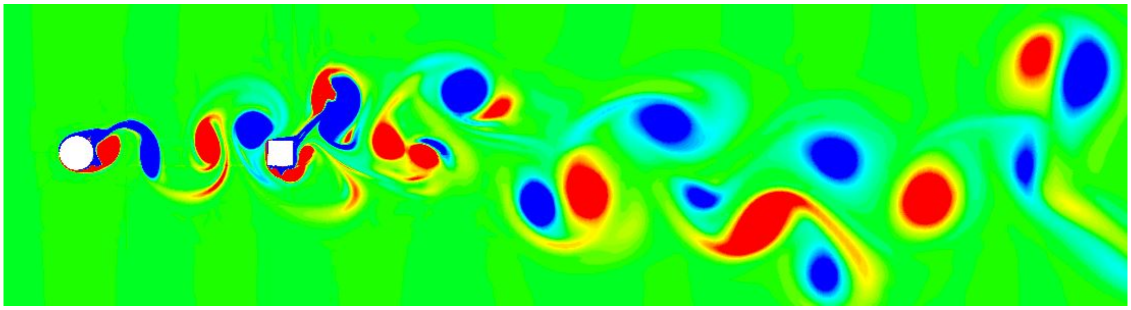

Figure 4.16: Vorticity contours for separation between the cylinders $6d$.

Time history of lift on the circular cylinder is shown in Figure 4.17 for different separation distance. Figure 4.17a shows that the fluctuating lift on the circular cylinder is periodic with smaller amplitude than that on the isolated cylinder. The close proximity of the square cylinder impedes the complete roll up of vortex shedding as show by the vorticity contours. For separation distance $s \geq 3d$, the lift becomes again periodic with amplitude very close to that of the single cylinder. The drag coefficient on the circular cylinder is shown in Figure 4.18 for different separation distance. Figure 4.18a shows that the fluctuating drag on the cylinder is also reduced in comparison with that on the isolated cylinder. For separation distance $s \geq 3d$, the influence of the square cylinder on the circular cylinder is reduced, and the drag becomes again periodic with amplitude very close to that of the isolated cylinder. The lift coefficient spectrum for different separation s is shown in Figure 4.19. For the small separation $s = 2d$ Figure 4.19a, the Strouhal number (fundamental frequency) is reduced to 0.15 in comparison with 0.2 for the isolated cylinder. The Strouhal number is 0.21 for $s = 3d$, and 0.227 for larger separation distance as shown in Table 4.3.

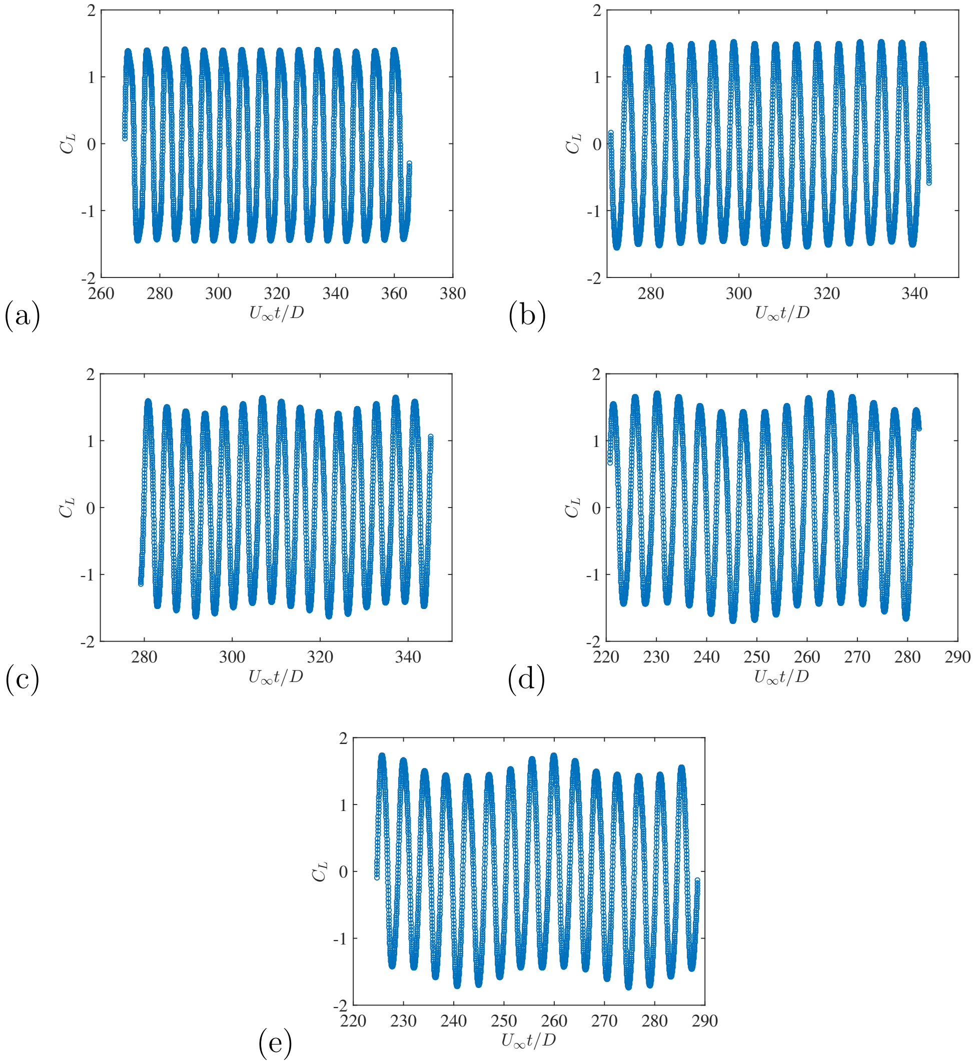

Figure 4.17: Lift coefficient of the circular cylinder for different separation s. (a) $s = 2d$, (b) $s = 3d$, (c) $s = 4d$, (d) $s = 5d$, (e) $s = 6d$.

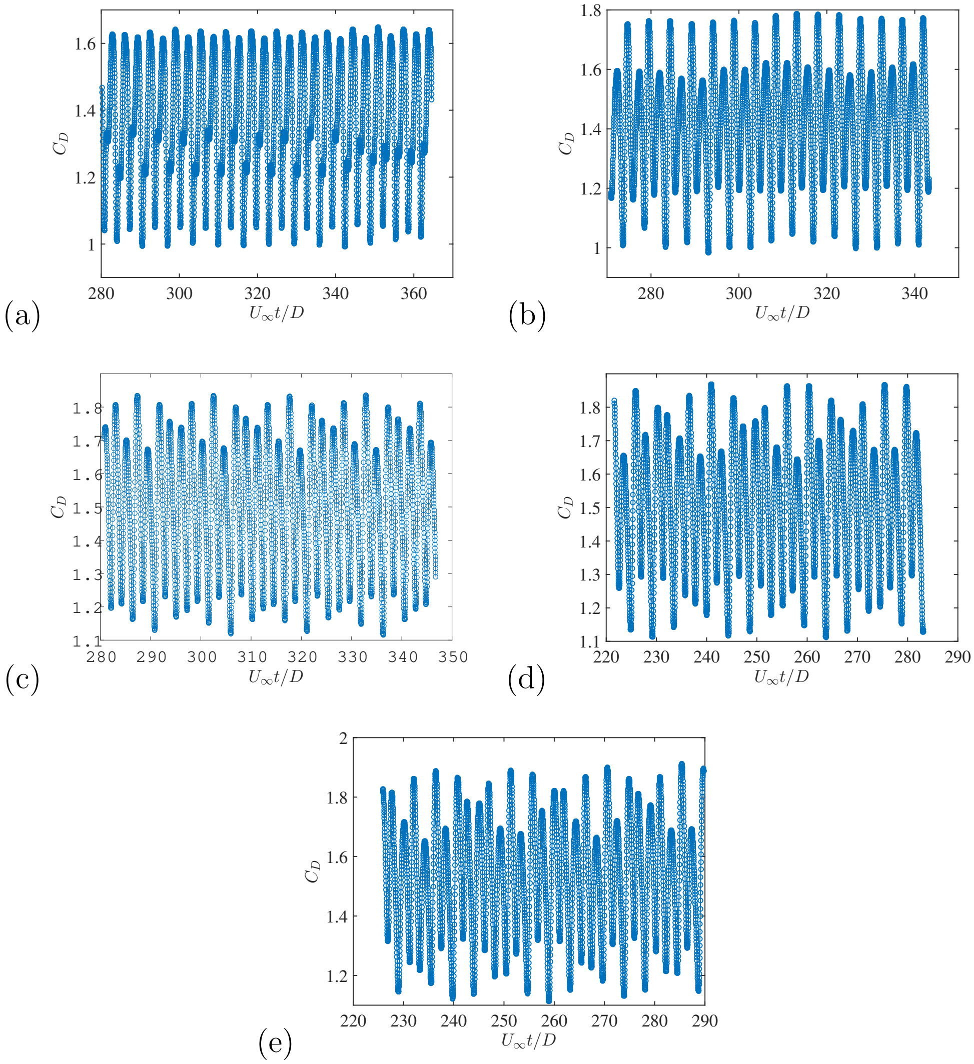

Figure 4.18: Drag coefficient of the circular cylinder for different separation s. (a) $s = 2d$, (b) $s = 3d$, (c) $s = 4d$, (d) $s = 5d$, (e) $s = 6d$.

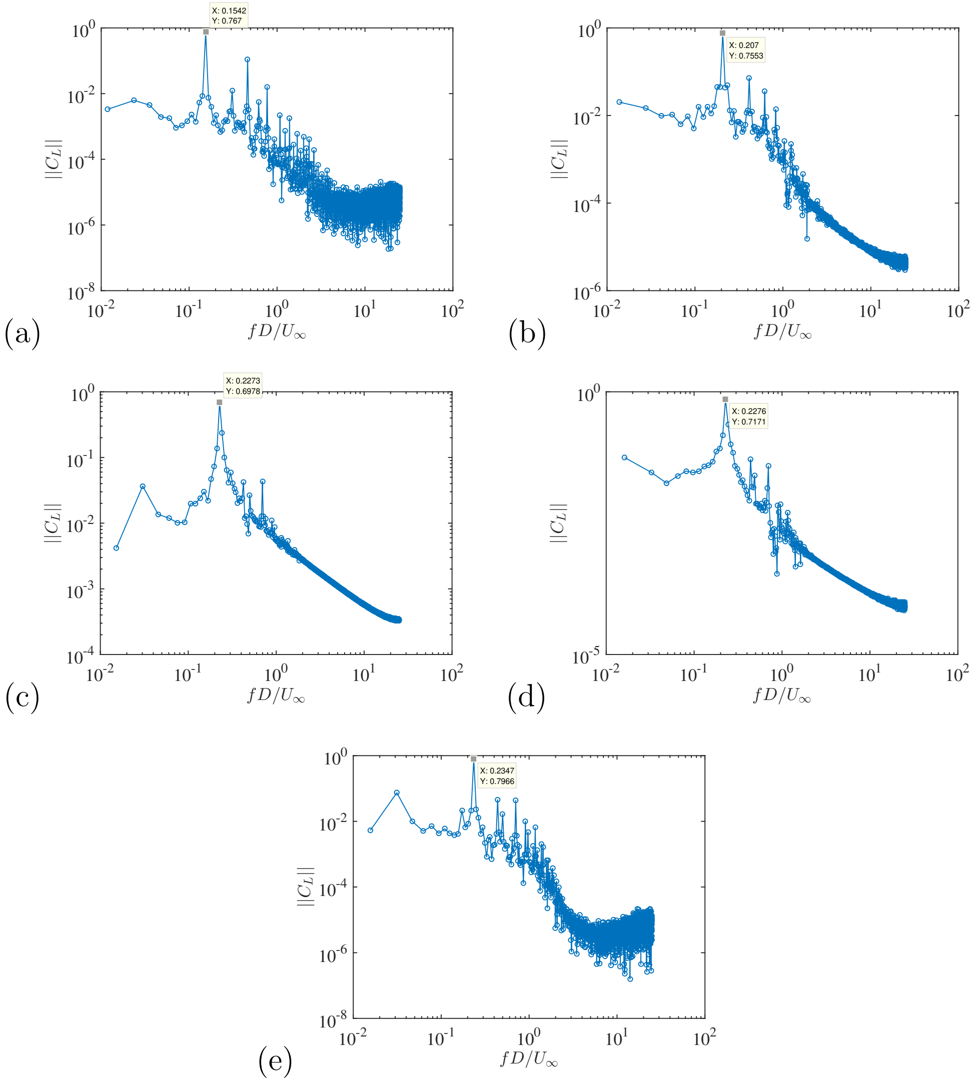

Figure 4.19: Lift coefficient spectrum of the circular cylinder for different separation s. (a) $s = 2d$, (b) $s = 3d$, (c) $s = 4d$, (d) $s = 5d$, (e) $s = 6d$.

Time history of lift on the square cylinder is shown in Figure 4.20 for different separation distance. From these figures, we see that the highest lift on the square cylinder is obtained for separation distance of $s = 2d$, and the frequency of is 0.15. The lift on the square cylinder decreases as the separation distance increases. For $2d < s < 6d$, we find the fundamental frequency (Strouhal number) of the fluctuating lift to be the same for the two cylinders.

The drag coefficient on the square cylinder is shown in Figure 4.21 for different separation distance. Spectral analysis of drag coefficient in Figure 4.21a shows that the fluctuating drag on the square cylinder has two frequencies 0.20 and 0.30; the lower frequency is the Strouhal number.

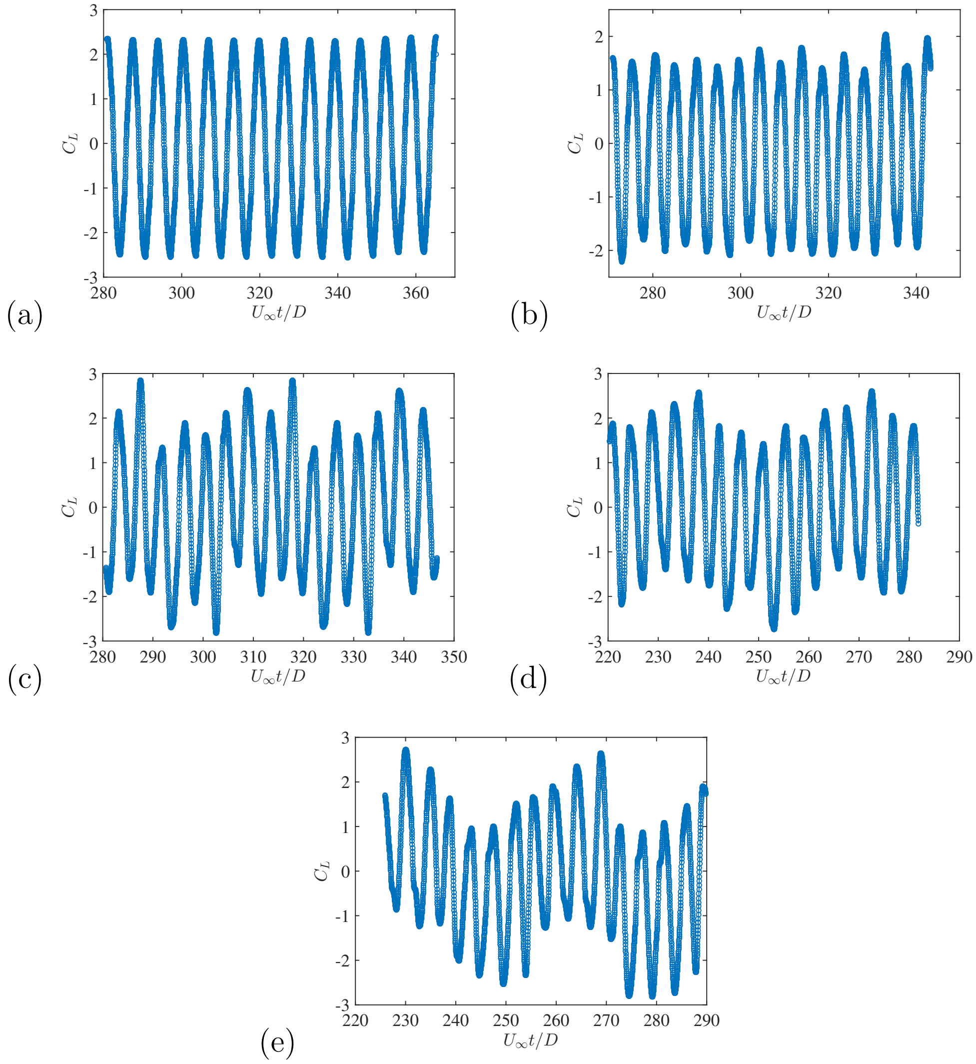

Figure 4.20: Lift coefficient of the square cylinder for different separation s. (a) $s = 2d$, (b) $s = 3d$, (c) $s = 4d$, (d) $s = 5d$, (e) $s = 6d$.

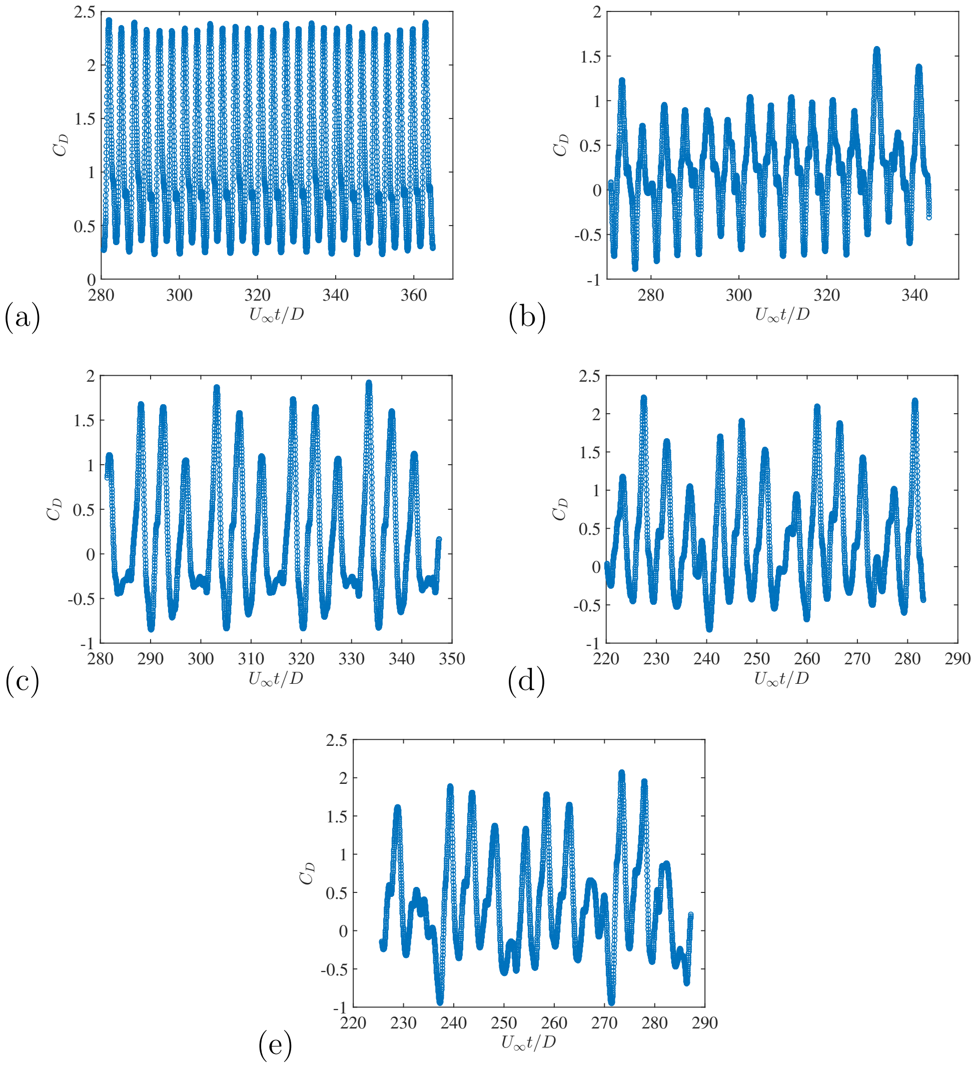

Figure 4.21: Drag coefficient of the square cylinder for different separation s. (a) $s = 2d$, (b) $s = 3d$, (c) $s = 4d$, (d) $s = 5d$, (e) $s = 6d$.

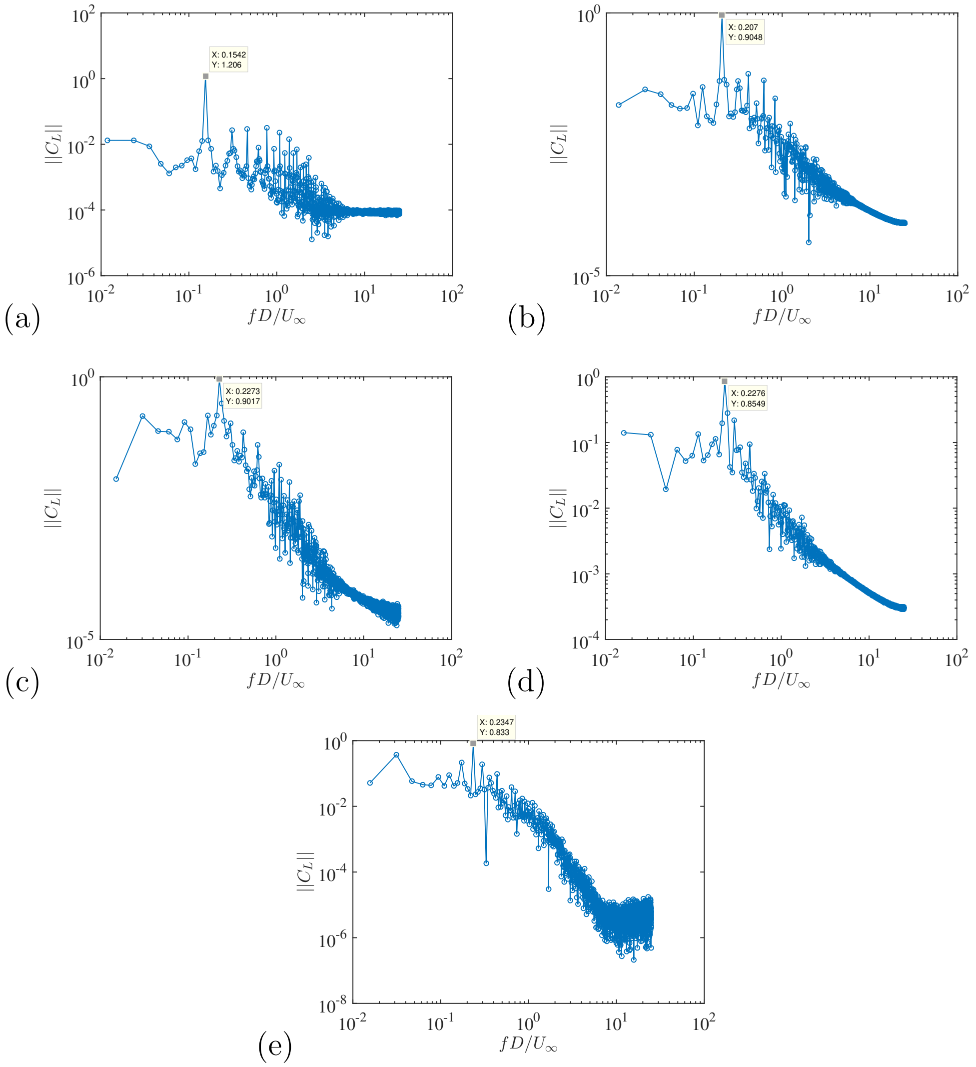

Figure 4.22: Lift coefficient spectrum of the square cylinder for different separation s. (a) $s = 2d$, (b) $s = 3d$, (c) $s = 4d$, (d) $s = 5d$, (e) $s = 6d$.

The obtained values of Strouhal number, fluctuating lift, and drag coefficients amplitudes for different spacing, which vary from $2d$ to $6d$ are shown in table 4.3. For $s = 2d$, frequency of vortex shedding the circular cylinder is reduced, and the lift is smaller than for other separation distances. The lift and drag on the circular cylinder increase slightly by the inference with the square cylinder. For $s > 3d$ the lift on the square appears to be strongly modulated by subharmonic frequencies. For $s = 3d$, the modulation is smaller.

Re=1642					
location	St	Cl_Circle	Cl_Square	CD_Circle	CD_Square
2d	0.1542	1.534	2.4120	0.89400	0.24560
3d	0.207	1.5106	1.8126	0.26300	0.59420
4d	0.2273	1.3956	1.8030	0.25440	0.74980
5d	0.2276	1.4342	1.7098	0.24900	0.49200
6d	0.2274	1.2892	1.6200	0.2344	0.56520

Table 4.3: Comparison of Strouhal number, fluctuating lift coefficient amplitude, and fluctuating drag coefficient at Re=1642

4.4 Conclusions

In this study 2-D numerical simulations were conducted for laminar flow over a single circular cylinder at Reynolds numbers Re=525 and Re= 1000. Analysis was focused on the fluctuation lift coefficients and drag coefficients and the Strouhal number. The results are validated by comparisons with previously published numerical results.

The interference between two cylinders in tandem was also investigated for a stationary circular cylinder at a Reynolds number of 1642 and a square cylinder in its wake. Computations are carried out for five values of the separation distance between the cylinders centers, $s = 2d, 3d, 4d, 5d$ and $6d$, where d the circle diameter. The fluctuating lift and drag coefficients and the Strouhal number have been determined as a function of the cylinders spacing. For $s \leq 2d$, the two cylinders acted as one long bluff body because the shed into vortices could not reach full strength before impingement on the square cylinder. The lift on the square cylinder attains its maximum when the spacing is $2s$ with a Strouhal number of 0.15.

In next chapter, our aim is to investigate energy harvesting from an elastically mounted square cylinder in the wake of a circular cylinder. The present results suggest that a separation distance between the cylinders of $3d$ is recommended because the fluctuating lift is dominated by a single frequency and its magnitude still high in comparison with larger separation distances.

Chapter 5

Piezoelectric energy harvesting from vortex-induced oscillations of tandem cylinders

5.1 Introduction

Conversion of mechanical energy into electrical energy energy is a well known technology. Harvesting mechanical energy from vibrating structures and its conversion to electrical energy has attracted a lot of attention in the past decades and [3, 39, 49]. Energy harvesting systems have been developed to operate electronic components such as wireless sensors, sensors for health monitoring, data transmitters, and medical applications [50, 51]. Those harvesters are designed to replace small batteries which have a finite life span and require frequent replacement. On the other hand, the transformation mechanism can be classified into electromagnetic [52], piezoelectric [53] and electrostatic [54]. However, the piezoelectric one has received the most attention due to its concise application and high energy density. Vortex-induced vibrations is encountered in various engineering applications such as oil industry, heat exchangers, chimneys, offshore platforms, tunnel construction facilities such as piping and crown molding, and underwater ocean structures. Harvesting piezoelectric energy from flow induced vibrations have been extensively studied in the past several years. It can be classified as Vortex Induced Vibrations (VIV) [55–63], flutter [13, 64–78],galloping, and Turbulence Induced Vibrations (TIV) [59, 79].

The flow around circular cylinders has been extensively studied in experimental investigation and numerical simulations. Assi et al. [80, 81] conducted PIV experiments to investigated vortex-induced vibrations of a single circular cylinder. They also investigated the VIV of a cylinder mounted on an elastic base and placed in the wake of fixed cylinder. They examined interference between the cylinders for separation distances between cylinders ranging from $2to6d$, where d is the cylinder diameter. Mittal et al. [46] and Prasanth et al. [82] performed numerical simulations with spacing of $5.5d$ for two similar circular cylinders. The downstream cylinder displayed a higher amplitude in the transverse direction, which was regarded as a typical wake-induced vibration characteristic. Wang et al. [83] performed numerical simulations for two unequal circular cylinders with a spacing of $5.5d$ in the tandem arrangement. Oscillation amplitudes and trajectory figures of the downstream cylinder were analyzed. Han et al. [84] investigated vortex induced vibrations of a circular cylinder placed in the wake of a fixed square cylinder at Reynolds number 150. The cylinder motion has two degrees of freedom. Bao et al. [85] performed numerical simulations of the flow around two circular cylinders in tandem; the front cylinder is fixed while the other one is vibrating. The separation distance is $5d$. Brika and Laneville [86] experimentally researched the vibrations of a flexible circular cylinder in the wake of another fixed cylinder. The cylinders arrangement is typical of transmission lines. The Reynolds number ranged from 5000 to 27000, and the separation between the cylinders is 7 to 25 diameters. There was no hysteresis reaction to the vibrating cylinder response, and a new division with a broader synchronization area declined as the gap between the two cylinders expanded.Hover and Triantafyllou [87] evaluated the flow over two cylinders in a tandem arrangement. They examined the fluid's response and forces in the downstream cylinder mounted elastically in the direction transverse to flow with a fixed gap spacing of $4.75d$ and $Re = 3.05 \times 10^4$. They found that the vortex-induced vibration and galloping response occurred when the reduced velocity was between 2 and 17.

In this chapter, we investigate energy harvesting from a flexible structure which is forced to vibrate by vortices created in the wake of another fixed structure. The vortex generator is a fixed circular cylinder, and the flexible structure is a square cylinder mounted on an elastic beam. Forces on the vibrating structure are determined by solving the Navier-Stokes equations for the flow over two cylinders in tandem in an otherwise uniform flow parallel to the line connecting their centers. The front cylinder is a fixed circular cylinder, and second cylinder is a square cylinder mounted on an elastic beam. The flow is assumed to be two dimensional, and the square cylinder is restricted to move in the transverse direction to the free stream flow. The square cylinder mass represents the energy harvesting model's tip mass, and the flexible beam represents the piezoelectric substrate, and is modeled by a spring-dash-pot system attached to the square cylinder mass. A mathematical model for the energy harvesting system is developed to investigate the effects of the structural model's geometric and material properties on energy harvesting. Geometric parameters include the streamwise positions of the square cylinder relative to the circular cylinder and their relative sizes. Also, the ratio of the galloping cylinder's natural frequency to the vortex shedding frequency is an important parameter that affects the galloping phenomenon and energy harvesting. The mass ratio, defined here as the mass of fluid displaced by the square cylinder to its mass, controls the vibrations amplitude and hence the harvested energy, and its effects will be investigated. The model can be used to study the effects of electromechanical coupling coefficient and equivalent capacitance of the piezoelectric element on the energy harvesting. It is expected that the present simplified model will be an economical and effective tool for the design and optimization of energy harvesting from galloping motion.

5.2 Mathematical formulation and numerical simulations

This section describes the mathematical model of the reduced order energy-harvesting model. The vibrating structure is a square cylinder placed in the wake of a fixed circular cylinder. We will discuss the coupling of the equations of motion of structure, fluid force, and voltage equation of the piezoelectric element. We will also present the time advancement scheme for the coupled equations. A dynamic mesh approach is adopted to account for the oscillating square cylinder.

We study the flow field characteristics around a square cylinder mounted on an elastic thin plate and restricted to move only transversely to the free stream flow direction, as shown in Fig. 5.1. The separation distance between the centers of circular and square cylinders is $3d$, and the height of the square cylinder is h. The square cylinder motion is forced by the vortices shed by the fixed circular cylinder.

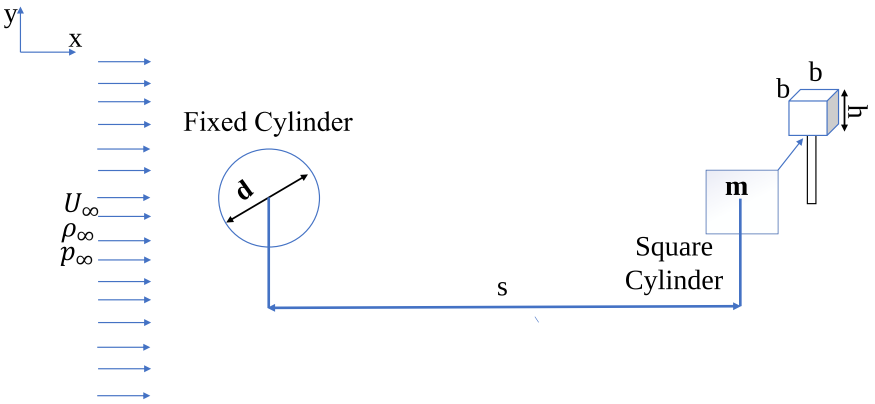

Figure 5.1: A schematic of a two-dimensional model of a fixed circular cylinder and an oscillating square cylinder

5.2.1 Hydrodynamic model

We assume a two-dimensional unsteady incompressible flow, and solve the unsteady Navier-Stokes equations numerically. We limit our study to low Reynolds number, and use fine grid to resolve all the two-dimensional motion scales. Thus no turbulence model is activated in the simulations. The equations for continuity and momentum may be expressed as follows:

Continuity :

$$\frac{\partial u}{\partial x} + \frac{\partial v}{\partial y} = 0 \tag{5.1}$$

Momentum:

$$\frac{\partial u}{\partial t} + u\frac{\partial u}{\partial x} + v\frac{\partial u}{\partial y} = -\frac{1}{\rho}\frac{\partial p}{\partial x} + \nu\left(\frac{\partial^2 u}{\partial x^2} + \frac{\partial^2 u}{\partial y^2}\right) \tag{5.2}$$

$$\frac{\partial v}{\partial t} + u\frac{\partial v}{\partial x} + v\frac{\partial v}{\partial y} = -\frac{1}{\rho}\frac{\partial p}{\partial y} + \nu\left(\frac{\partial^2 v}{\partial x^2} + \frac{\partial^2 v}{\partial y^2}\right) \tag{5.3}$$

where $\nu = \mu/\rho$ is the kinematic viscosity.

Nondimensional variables

We use the cylinder diameter d, free stream velocity U, pressure ρU^2, time d/U as reference length, velocity, pressure, and time, respectively and rewrite the equations in a non-dimensional form as

$$\frac{\partial u}{\partial x} + \frac{\partial v}{\partial y} = 0 \tag{5.4}$$

$$\frac{\partial u}{\partial t} + u\frac{\partial u}{\partial x} + v\frac{\partial u}{\partial y} = -\frac{\partial p}{\partial x} + \frac{1}{Re}\left(\frac{\partial^2 u}{\partial x^2} + \frac{\partial^2 u}{\partial y^2}\right) \tag{5.5}$$

$$\frac{\partial v}{\partial t} + u\frac{\partial v}{\partial x} + v\frac{\partial v}{\partial y} = -\frac{\partial p}{\partial y} + \frac{1}{Re}\left(\frac{\partial^2 v}{\partial x^2} + \frac{\partial^2 v}{\partial y^2}\right) \tag{5.6}$$

where $Re = Ud/\nu$ is the Reynolds number.

5.2.2 Lumped parameter model of piezoelectric energy harvester

In this analysis, we considered two cylinders of which one is mounted to be fixed and another is mounted to an elastic support such that it was allowed to oscillate in the Y direction. A lumped parameter linear spring-mass-damper equation is used to represent the oscillation of the cylinder when forced by a fluid load to perform the parametric identification analysis as

Governing equations of beam and structure are

$$m\frac{d^2 y}{dt^2} + c\frac{dy}{dt} + ky = F_y \tag{5.7}$$

where m is the oscillating system's mass, c is the coefficient of structural damping, k is the coefficient of stiffness, and F_y is the fluid force exerted in the direction of motion. We introduce nondimensional variables

$$y^* = \frac{y}{d} \qquad t^* = \frac{U_\infty t}{d} \qquad F^* = \frac{F}{\rho_\infty U_\infty^2 dh} \tag{5.8}$$

where is U_∞ free stream velocity and ρ_∞ is the fluid density, and rewrite the equation of motion in nondimensional form,

$$U_\infty^2 \quad \frac{md}{d^2} \quad \frac{d^2y^*}{dt^{*2}} + \frac{cU_\infty d}{d} \quad \frac{dy^*}{dt^*} + kdy^* = \rho_\infty U_\infty^2 dhF^* \tag{5.9}$$

hence

$$\ddot{y^*} + \frac{cd}{mU_\infty}\dot{y^*} + \frac{k}{m}\frac{d^2}{U_\infty^2}y^* = \frac{\rho_\infty d^2 h}{m}F^* \tag{5.10}$$

Let

$$\omega_n^2 = \frac{k}{m} \quad ; \quad \omega_n^* = \frac{d}{U_\infty}\sqrt{\frac{k}{m}}; \quad c^* = \frac{cd}{mU_\infty}, \quad m_f = \rho_\infty hb^2 \tag{5.11}$$

hb^2 is the volume of the square cylinder, and $m_f = \rho_\infty hb^2$ is the fluid mass displaced by the cylinder.

$$F^* = \frac{F}{\rho_\infty U_\infty^2 dh} = \frac{F/h}{\rho_\infty U_\infty^2 d} \tag{5.12}$$

We note that F/h is the lift on the square cylinder per unit length, which is the instantaneous force in the $y-$direction as computed by the two-dimensional numerical simulations, hence $F^* = F_y^*$. We wrote a user defined function (UDF) for integrating the equation of motion in time simultaneously with the Navier-Stokes equations. The instantaneous value of F_y^* computed by Fluent software is passed to the UDF.

$$\ddot{y^*} + c^*\dot{y^*} + \omega_n^{*2}y^* = \frac{\rho_\infty d^2 h}{m}F_y^* \tag{5.13}$$

$$\frac{\rho_\infty d^2 h}{m} F_y^* = \frac{\rho_\infty d^2 h}{m} \left(\frac{d}{b}\right)^2 F_y^* = \frac{m_f}{m} \left(\frac{d}{b}\right)^2 F^* \tag{5.14}$$

Let $r_m = m_f/m$, is the ratio of fluid mass displacement by the energy-harvester cylinder to its mass.

$$c^* = \frac{cd}{mU_\infty} = \frac{dc\omega_n^2}{U_\infty k} = 2\zeta{\omega_n}^* \tag{5.15}$$

where

$$\zeta = \frac{c\omega_n}{2k} \tag{5.16}$$

$$\ddot{y}^* + 2\zeta\omega^* \dot{y}^* + \omega_n^{*2} y^* = \alpha_o F^* \tag{5.17}$$

where

$$\alpha_o = r_m \left(\frac{d}{b}\right)^2 \tag{5.18}$$

Without the piezoelectric element, the forced equation of motion of the square cylinder depends on six non-dimensional parameters: ω_n^*, ζ, r_m, $b^* = b/d$, $s^* = s/d$, and Re. We note that ω_n^* is the natural frequency of the oscillator scaled by U_∞/d. Since the Stouhal number is defined by $St = fd/U_\infty$, then

$$\omega_n^* = \frac{\omega_n}{f} St \tag{5.19}$$

As such, ω_n^* is the ratio of natural frequency of the energy-harvesting cylinder to the vortex shedding frequency. ζ is structural damping parameter. The mass ratio r_m is an important parameter. For light fluids such as air, its value will be small unless the energy-harvesting cylinder volume is large.

The energy-harvesting element is the beam and the attached square cylinder. When placed in the wake of a fixed circular cylinder, it is forced to oscillate in the cross-flow direction. Piezoelectric patches are bonded to the beam, and the induced strains generate an electric potential difference, V, across a resistor load, R. The equations governing the dynamics of this coupled system can be written as

$$m\ddot{y} + c\dot{y} + ky - \theta V = F \tag{5.20}$$

$$\theta\dot{y} + C_p\dot{V} + \frac{V}{R} = 0 \tag{5.21}$$

where θ and C_p are the electro mechanical coupling and equivalent capacitance, respectively. F the fluid force in the transverse direction acting on the harvester square cylinder. We define

$$G = \theta V \tag{5.22}$$

and note that G has the units of force, N. The voltage equation is written in terms of G,

$$\theta^2\dot{y} + C_p\dot{G} + \frac{G}{R} = 0 \tag{5.23}$$

We rewrite G in non-dimensional form

$$G^* = \frac{dG}{mU_\infty^2} \tag{5.24}$$

The non-dimensional coupled equation of motion and voltage equation are

$$\ddot{y^*} + 2\zeta\omega^*\dot{y^*} + \omega_n^{*2}y^* - G^* = \alpha_o F^* \tag{5.25}$$

$$\eta_1\dot{y}^* + \eta_2\dot{G}^* + G^* = 0 \tag{5.26}$$

where

$$\eta_1 = \frac{\theta^2 dR}{mU_\infty}, \qquad \eta_2 = \frac{C_p R U_\infty}{d} \tag{5.27}$$

The coupled system now has eight non-dimensional parameters: ω_n^*, ζ, r_m, b^*, s^*, Re, η_1 and η_2.

5.2.3 Time integration scheme of coupled model

The equation of motion is advanced in time by the Newmark Method, and the voltage equation by an implicit second-order finite difference method.

Change the notion: We drop the asterisk, and let $y^* = y$ and $G^* = G$, etc.

Newmark method

At time step m, we assume that the displacement y^m, the velocity $\dot{y}^m$, acceleration $\ddot{y}^m$, and voltage G^m are known. We want to find these quantities at time step $m+1$, where the time step is Δt.

Displacement update formula

$$y^{m+1} = y^m + \dot{y}^m \triangle t + \frac{1}{2}(1-\gamma)(\triangle t)^2 \ddot{y}^m + \frac{1}{2}\gamma(\triangle t)^2 \ddot{y}^{m+1} \tag{5.28}$$

Velocity update formula

$$\dot{y}^{m+1} = \dot{y}^m + (1-\alpha)\triangle t \ddot{y}^m + \alpha \Delta t \ddot{y}^{m+1} \tag{5.29}$$

where α and γ are constants. We take $\alpha = \gamma = 0.5$.

Using second-order implicit finite-difference formulae, we write the voltage equation at $m+1$

$$\eta_1 \frac{1}{2}(\dot{y}^{m+1} + \dot{y}^m) + \eta_2 \frac{G^{m+1} - G^m}{\triangle t} + \frac{1}{2}(G^{m+1} + G^m) = 0 \tag{5.30}$$

$$G^{m+1} = -\frac{\eta_1}{1+\frac{2\eta_2}{\triangle t}}(\dot{y}^{m+1}+\dot{y}^m) - \frac{1-\frac{2\eta_2}{\triangle t}}{1+\frac{2\eta_2}{\triangle t}}G^m \tag{5.31}$$

Voltage update formula

$$G^{m+1} = -c_1(\dot{y}^{m+1}+\dot{y}^m) - c_2 G^m \tag{5.32}$$

where ;

$$c_1 = \frac{\eta_1}{1+\frac{2\eta_2}{\triangle t}}, \quad c_2 = \frac{1-\frac{2\eta_2}{\triangle t}}{1+\frac{2\eta_2}{\triangle t}} \tag{5.33}$$

The equation of motion at step $m+1$ gives

$$\ddot{y}^{m+1} + 2\zeta\omega_n\dot{y}^{m+1} + \omega_n^2 y^{m+1} - G^{m+1} = \alpha_o F^{m+1} \tag{5.34}$$

Using the voltage update formula, we get

$$\ddot{y}^{m+1} + 2\zeta\omega_n\dot{y}^{m+1} + \omega_n^2 y^{m+1} + c_1(\dot{y}^{m+1}+\dot{y}^m) + c_2 G^m = \alpha_o F^{m+1} \tag{5.35}$$

$$\ddot{y}^{m+1} + (2\zeta\omega_n + c_1)\dot{y}^{m+1} + \omega_n^2 y^{m+1} = \alpha_o F^{m+1} - c_1\dot{y}^m - c_2 G^m \tag{5.36}$$

By substituting the displacement and velocity update formulas, we eliminate $\dot{y}^{m+1}$ and y^{m+1}, and obtain $\ddot{y}^{m+1}$,

$$\begin{aligned} \ddot{y}^{m+1} + (2\zeta\omega_n + c_1)[\dot{y}^m + (1-\alpha)\triangle t\ddot{y}^m + \alpha\Delta t\ddot{y}^{m+1}] \\ +\omega_n^2[y^m + \dot{y}^m\triangle t + \frac{1}{2}(1-\gamma)(\triangle t)^2\ddot{y}^m + \frac{1}{2}\gamma(\triangle t)^2\ddot{y}^{m+1}] = \alpha_o F^{m+1} - c_1\dot{y}^m - c_2 G^m \end{aligned} \tag{5.37}$$

Once $\ddot{y}^{m+1}$ is found, the velocity, displacement, and voltage can be found at the new time step $m+1$. This algorithm is programmed in a user-defined function UDF, and coupled with the Navier-Stokes solver that provides the force F^{m+1}.

Mean power

Measures of the energy harvesting device output are the instantaneous power dissipated in the resistor

$$P = \frac{V^2}{R} \tag{5.38}$$

and its root-mean-square

$$P_{rms} = \frac{V_{rms}^2}{R} \tag{5.39}$$

5.2.4 Computational domain and boundary conditions

We used ANSYS-Fluent (V17.2) to solve the Navier-Stokes equations on a block-structured mesh. The dynamic mesh model can be used to model flows where, due to motion on the domain borders, the shape of the domain changes over time. The dynamic mesh allows the trajectory of a moving object to be calculated by aero or hydrodynamic forces.

Geometry of the domain is created using built-in geometry creation tools of ICEM CFD. One degree-of-freedom (DOF) model is used because the Square Cylinder is only allowed to move in the transverse direction. The entire computational domain is divided into four domains as shown in Figure 5.2, including inlet-domain (domain 1), deforming domain around the square cylinder (domain 2), far field fixed portion (domain 3), downstream fixed mesh (domain 4). The computational domain lengths in x-direction and y-direction are $51d$ and $30d$, respectively. The cylinders are separated by a fixed distance of $s = 3d$ in the stream-wise direction. The mesh size is 304592 nodes as shown in figures 5.3 to 5.5. Inflow boundary condition is imposed on the upstream boundary where uniform flow velocity is prescribed. Symmetry conditions are imposed on the two sides (bottom and top) of the computational domain. The downstream boundary, atmospheric pressure is prescibed.

The flow solver is pressure based where the pressure and momentum equations are solved by the ”Simple” technique. We used the transient (unsteady) solution method and second-order Euler for time integration with fixed time-step of 0.02s.The coupling between the square cylinder motion and flow field is realized by the User-Defined Function (UDF) in Fluent. The instantaneous force on the square cylinder is passed from the Navier-Stokes solver to the UDF. The equation of motion and voltage equation are advanced by one time step, and the new instantaneous displacement and velocity are passed back to the dynamic mesh routine for updating the deforming mesh (re-meshing).

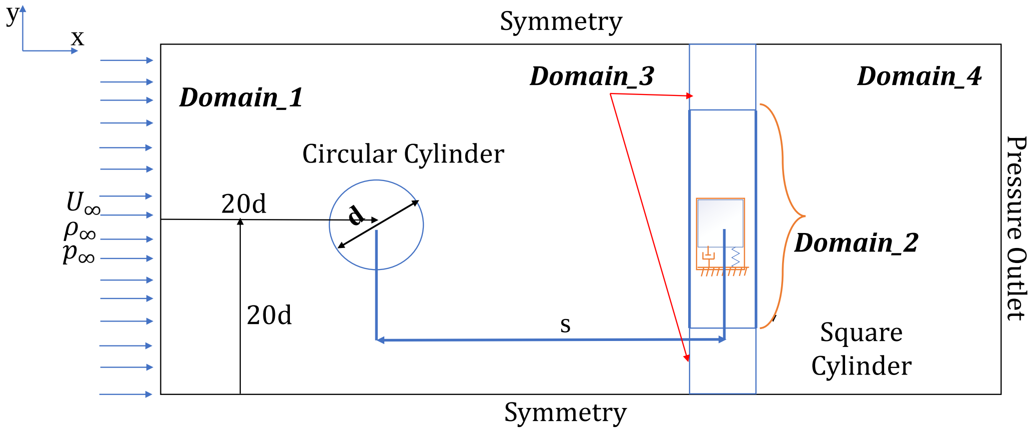

Figure 5.2: A schematic of a two-dimensional model of a fixed circular cylinder and an oscillating square cylinder.

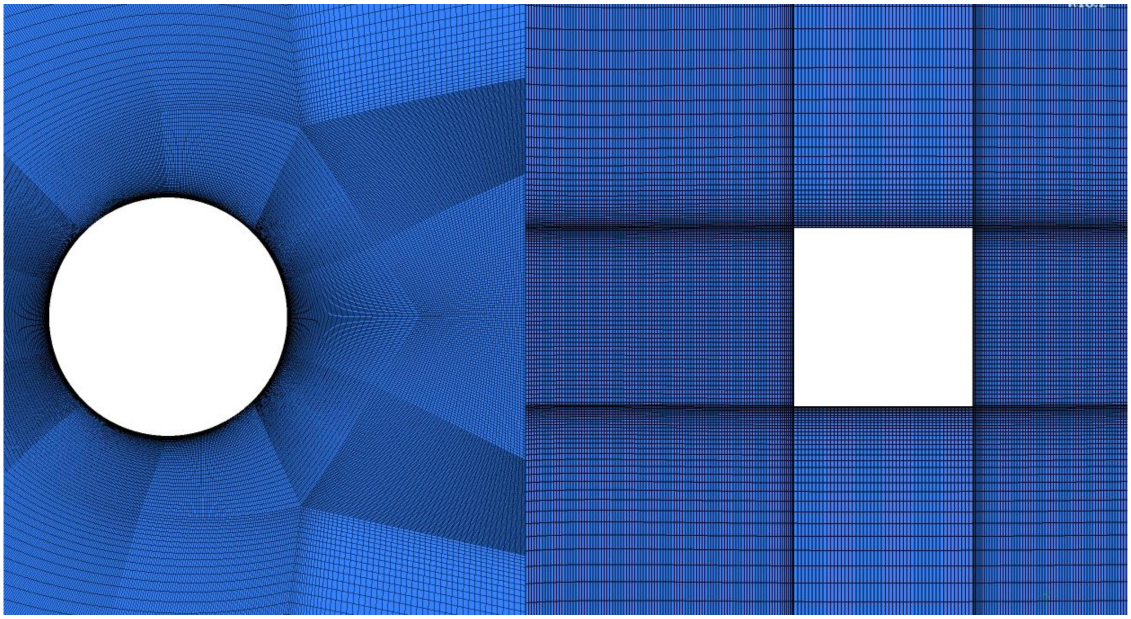

Figure 5.3: Zoomed-in view of the mesh around two cylinders with total nodes 304592

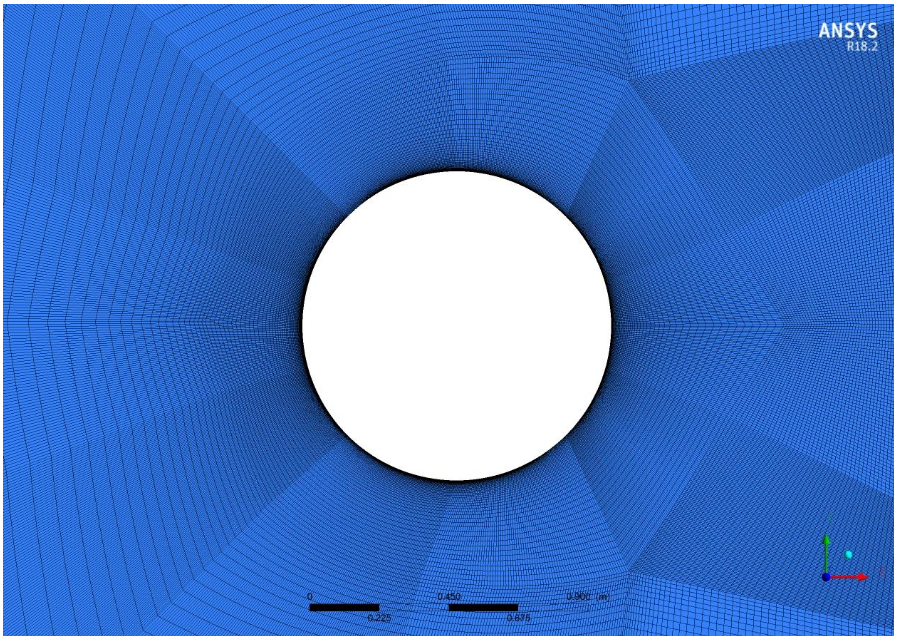

Figure 5.4: Zoomed-in view of the mesh around circular cylinder

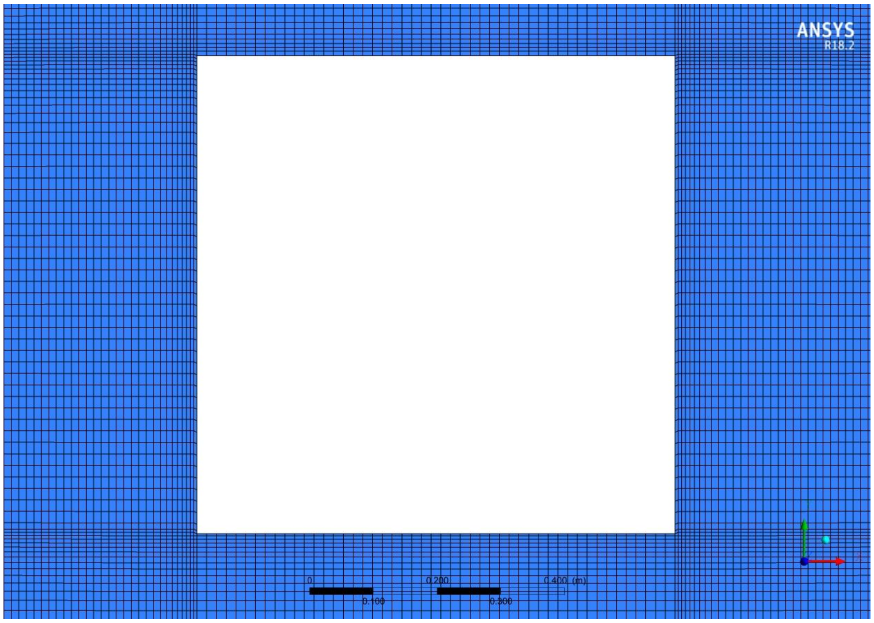

Figure 5.5: Zoomed-in view of the mesh around for square cylinder

5.3 Results and discussion

The power output of the piezoelectric energy harvesting model adopted in this dissertation depends on thirteen physical parameters given in Table 5.3. They are reduced to eight non-dimensional groups shown in Table 5.3. The coupled fluid-structure model is solved in terms of non-dimensional variables. Therefore, only non-dimensional parameters are input to the simulation model. For clearer understanding of the energy harvester performance, the model outputs (voltage, power, and harvester mass displacement) are presented in dimensional form. Certain parameters are fixed for all the results presented in this chapter: diameter ratio $b^* = b/d = 0.75$, separation distance between cylinders centers $s^* = s/d = 3$, and structural damping parameter $\zeta = 0.1$. For converting the non-dimensional outputs to dimensional quantities, certain variables must be prescribed.

Circular cylinder diameter	d (m)
Square cylinder side	b (m)
Square cylinder height	h (m)
Separation distance between cylinders	s (m)
Free stream velocity	U_∞ (m.s^{-1})
Fluid density	ρ_∞ (kg.m^{-3})
Fluid viscosity	μ_∞ (N.s.m^{-2})
Mass of square cylinder	m (kg)
Spring stiffness	k (N.m^{-1})
Structural damping coefficient	c (N.s.m^{-1})
Electromechanical coupling	θ (N.V^{-1})
Equivalent capacitance	C_p (F$\equiv$ N.m.V^{-2}), Farad
Electric resistance	R ($\Omega \equiv$ V^2.s.N^{-1}.m^{-1}), Ohm

Table 5.1: Dimensional input parameters.

Diameter ratio	$b^* = b/d$
Separation distance ratio	$s^* = s/d$
Reynolds number	$Re = \rho_\infty U_\infty d/\mu_\infty$
Mass ratio	$r_m = \rho_\infty b^2 h/m$
Natural frequency parameter	$\omega^* = (d/U_\infty)\sqrt{k/m}$
Structural damping parameter	$\zeta = (c/2k)\sqrt{k/m}$
Electromechanical coupling parameter	$\eta_1 = \theta^2 Rd/(mU_\infty)$
Equivalent capacitance parameter	$\eta_2 = C_p RU_\infty/d$

Table 5.2: Nondimensional input parameters.

We studied the effects of two of the eight non-dimensional parameters, namely ω_n^* and the mass ratio r_m on the voltage and power of the piezoelectric energy harvester.

5.3.1 Preliminary results assuming harmonic forcing

In this section, we assume that the fluid force acting on the square cylinder is harmonic in time with prescribed frequency $2\pi St$, where $St = 0.2$.

$$F^* = F_o cos(2\pi St\, t) \tag{5.40}$$

where $F_o = 1.6$. In this case we integrate the coupled fluid-piezoelectric model in time independently of the Navier-Stokes solver. The selected parameters are given in Table 5.3.2. Effects of $\omega_n^*/(2\pi St)$ and θ on the RMS power are shown in Figure 5.3.1. There is a sharp maximum of power when the natural frequency of the piezoelectric harvesting element is equal to the Strouhal number (resonance). Also, when $\omega_n^*/2\pi St = 1$, there is an optimum value of the electromechanical coupling parameter θ.

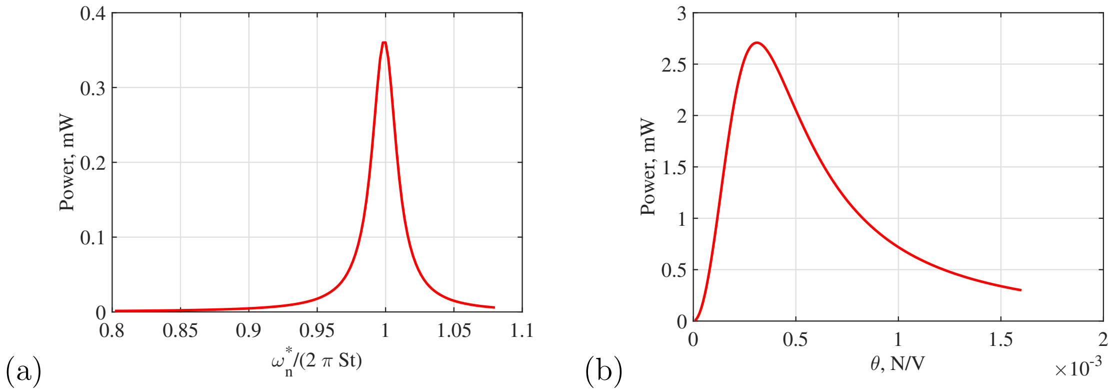

Figure 5.6: Effects of (a) $\omega_n^*/(2\pi St)$ and (b) θ on RMS power for harmonic forcing.

5.3.2 Effects of varying ω_n^*n the system outputs

We anticipate large displacements of the square cylinder when the vortex shedding frequency (Strouhal number) is close to the natural frequency of the energy harvesting oscillator. So, we select values of ω_n^* to be close to St. Based on the simulations of the previous chapter, we assumed $St = 0.2$, and select the set $\omega_n^* = (0.7, 0.8, 0.9, 1.0, 1.1, 1.2)(2\pi St)$.

d	0.02 m
h	0.3 m
m	0.01 kg
U_∞	1.2 m/s
ρ_∞	1.225 kg/m^3
μ_∞	1.789×10^{-5} Pa.s
θ	8×10^{-5} N/V
C_p	2×10^{-8} F
R	$4 \times 10^{6}\Omega$
Re	1.6434×10^{3}
r_m	8.2688×10^{-3}
η_1	0.042667
η_2	4.8

Table 5.3: Input parameters of energy harvesting system.

Figures 5.7 and 5.8 show the history of fluctuating lift on the circular and square cylinders, respectively, for different values of ω_n^*. When the vortex are generated by the fixed circular cylinder they give excitation to the elastic cylinder behind it. The spectrum of lift on the square cylinder is shown in figure 5.36. The lift on the circular cylinder is self induced by the shed vortices and hence is dominated by a clear single frequency. The lift on the square cylinder is dominated by the interaction with the incident vortices and also by self generated vortices. As such, the spectrum of the square cylinder lift exhibits multiple frequencies. The lift is dominated by the incident vortices frequency for the case (d) for which the natural frequency of the energy harvester is close to the Strouhal number of the circular cylinder. Even though the cross-section of the square cylinder is smaller that that of the circular cylinder, the lift magnitude on the square cylinder is higher that that on the circular cylinder.

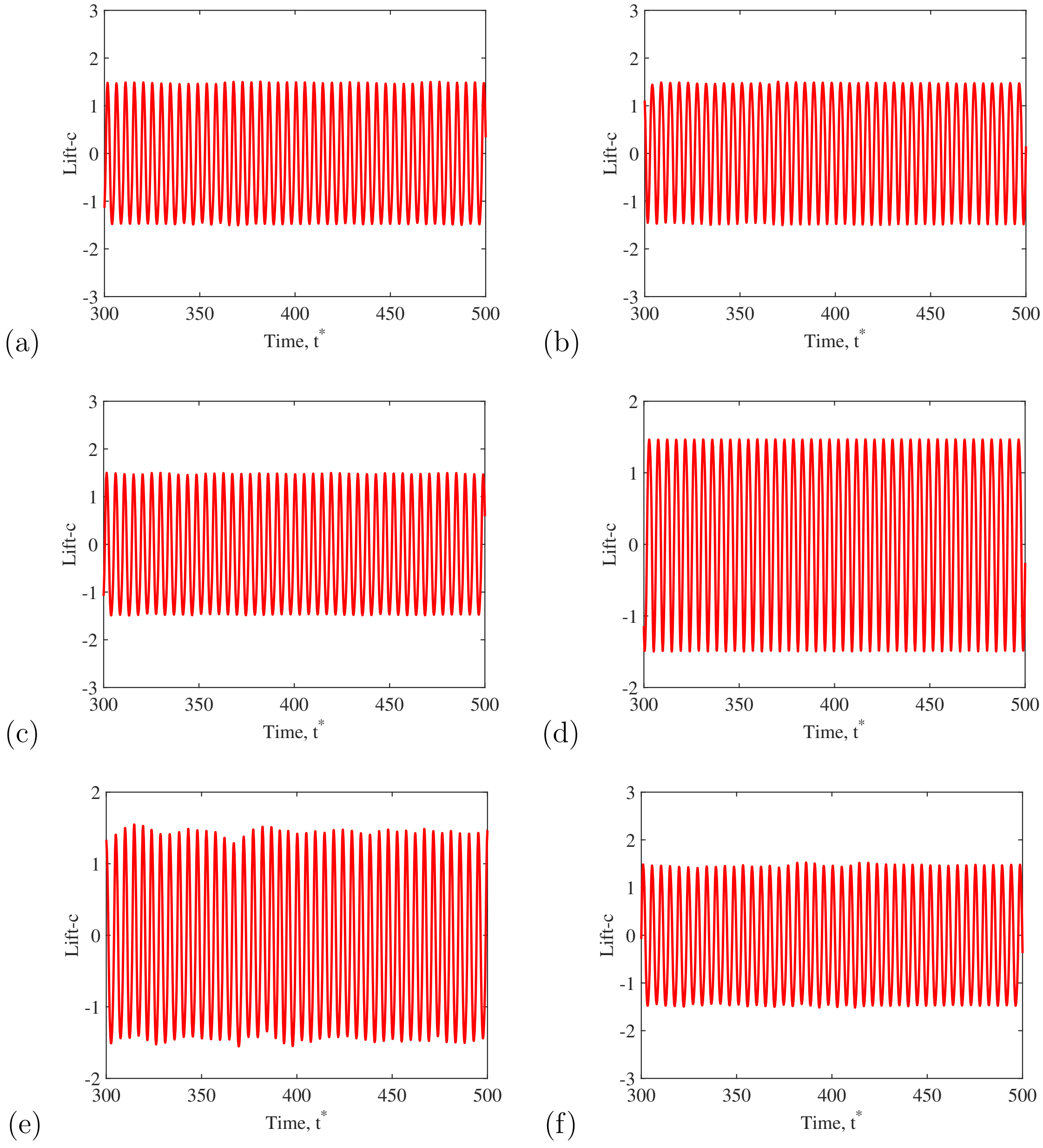

Figure 5.7: Fluctuating circular cylinder lift for various natural frequency $\omega_n^*/(2\pi St)$. (a) 0.7, (b) 0.8, (c) 0.9, (d) 1, (e) 1.1, and (f) 1.2

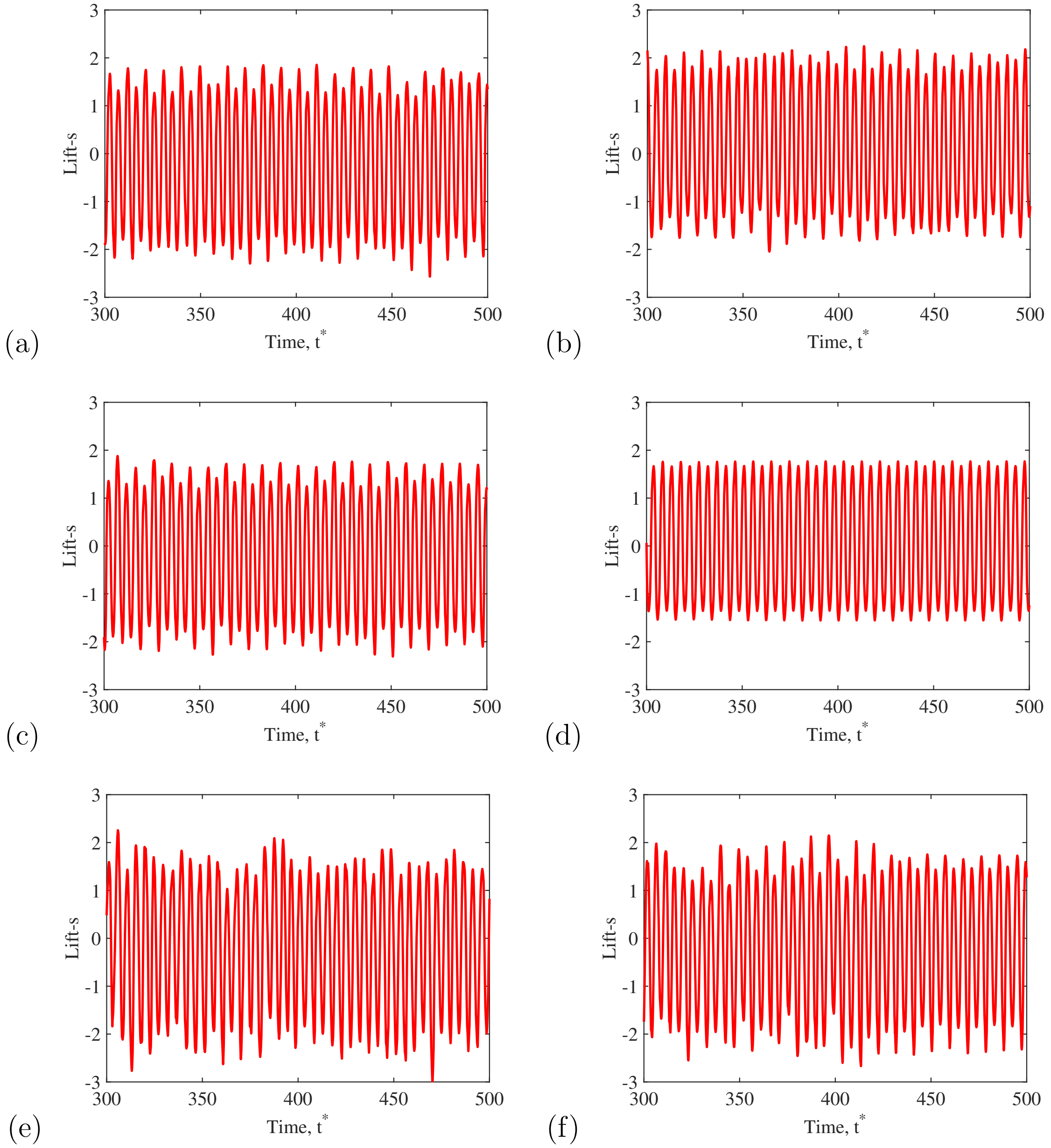

Figure 5.8: Fluctuating square cylinder lift for various natural frequency $\omega_n^*/(2\pi St)$. (a) 0.7, (b) 0.8, (c) 0.9, (d) 1, (e) 1.1, and (f) 1.2

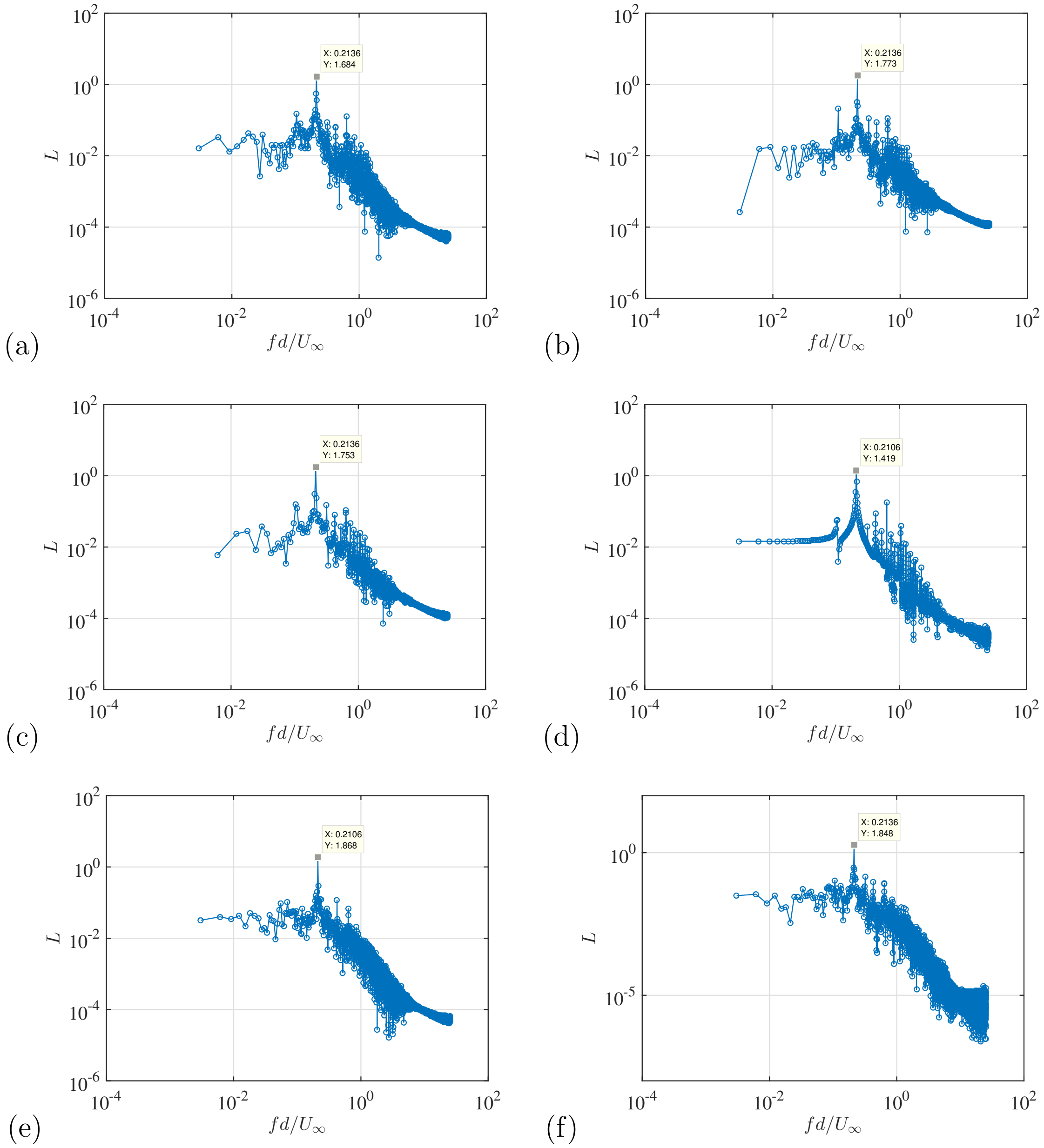

Figure 5.9: Square cylinder lift coefficient spectrum for various natural frequency $\omega_n^*/(2\pi St)$. (a) 0.7, (b) 0.8, (c) 0.9, (d) 1, (e) 1.1, and (f) 1.2

Figure 5.10 shows the history of the displacement of square cylinder for six different natural frequency $\omega_n^*/(2\pi St)$. The displacement of the square cylinder is in the range of 0.4 to 2 mm, which much smaller than the diameter the circular cylinder ($d = 20$ mm). The maximum displacement happens when the natural frequency is close to the vortex shedding frequency. When $\omega_n^*/(2\pi St) = 1$, the square cylinder oscillates with amplitude 1.5 mm at the dominant frequency of the lift. For $\omega_n^*/(2\pi St) = 1.1$, the displacement amplitude is 2 mm, but with multiple frequencies.

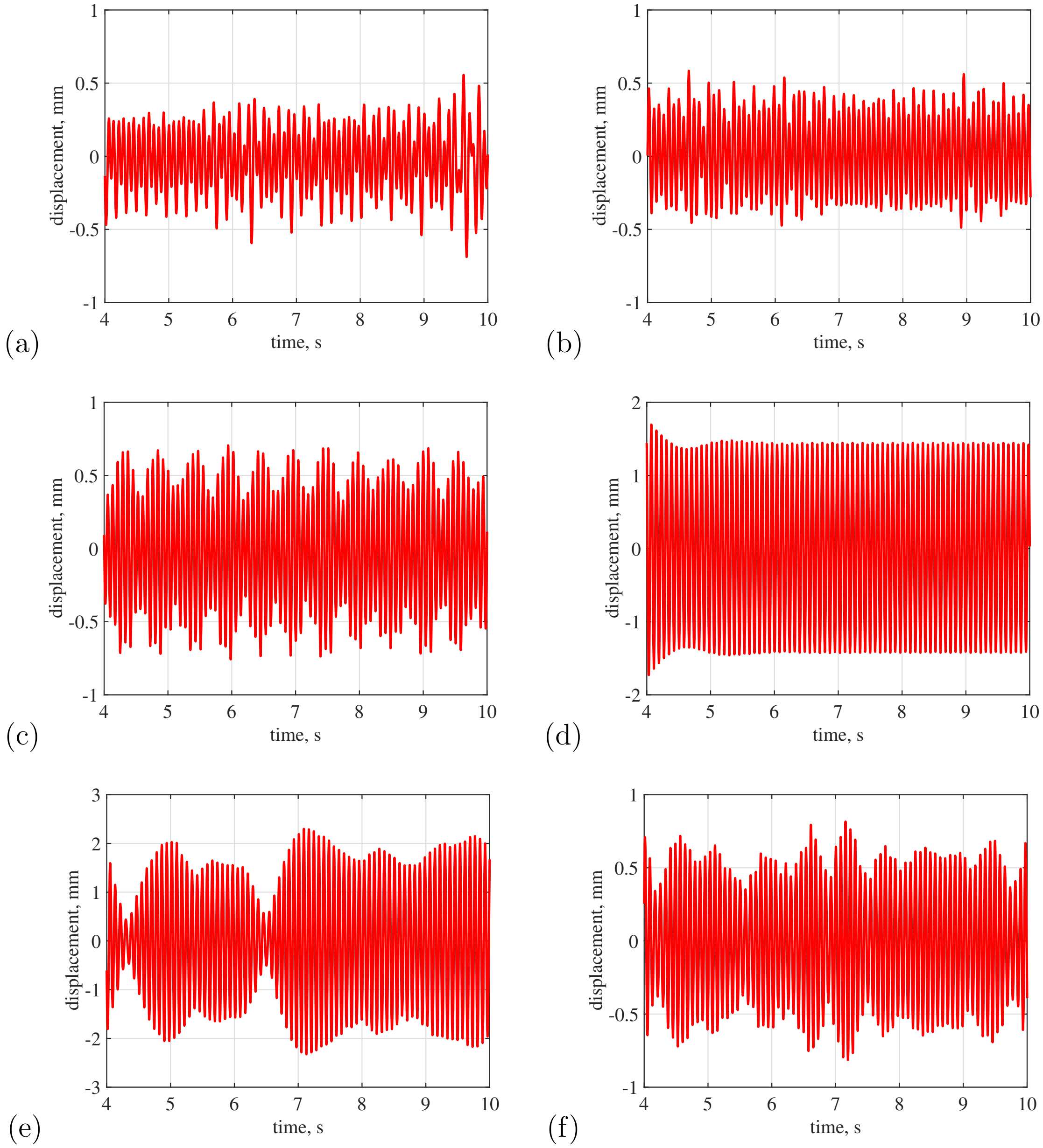

Figure 5.10: Displacement of square cylinder for various natural frequency $\omega_n^*/(2\pi St)$. (a) 0.7, (b) 0.8, (c) 0.9, (d) 1, (e) 1.1, and (f) 1.2

Figure 5.11 shows the history of the voltage in piezoelectric element for different natural frequency $\omega_n^*/(2\pi St)$. The voltage, being proportional to the velocity of the square cylinder, behaves similar to the square cylinder displacement. The volt amplitude is in the range of 2 to 7 V. The The maximum volt is nearly periodic with single frequency when the natural frequency of the energy harvester is close to the vortex shedding frequency. When $\omega_n^*/(2\pi St) = 1$, the amplitude 5.5 V at the dominant frequency of the lift. For $\omega_n^*/(2\pi St) = 1.1$, the volt amplitude reaches 7 V, but with multiple frequencies.

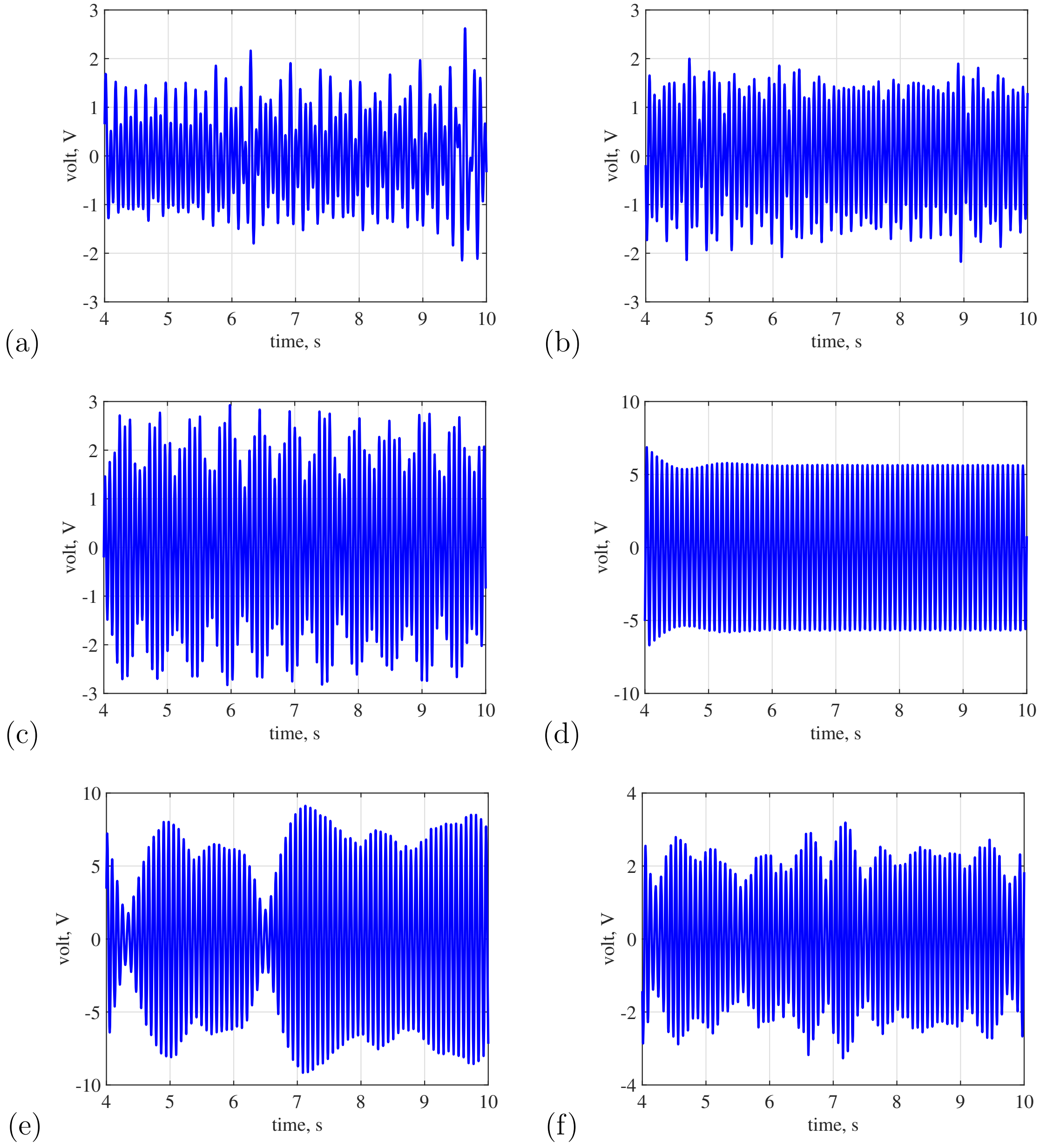

Figure 5.11: Voltage for various natural frequency $\omega_n^*/(2\pi St)$. (a) 0.7, (b) 0.8, (c) 0.9, (d) 1, (e) 1.1, and (f) 1.2

Figure 5.12 shows the instantaneous power dissipated in the resistor for different natural frequency $\omega_n^*/(2\pi St)$. The highest instantaneous power of 8 μW is obtained for $\omega_n^*/(2\pi St) =$ 1 and 1.1. Table 5.4 gives a summary of the results of the effects of natural frequency on the output voltage and power. The Strouhal number of the square cylinder is determined by the vortex shedding from the circular cylinder at it takes the value 0.21. The best performance of the harvester is obtained for $\omega_n^* = 1.38$ which corresponds to $\omega_n^*/(2\pi St) = 1.1$. Figure 5.13 shows the RMS power as a function of the natural frequency ω_n^*. The power deteriorates very rapidly when the natural frequency is shifted from the shedding frequency.

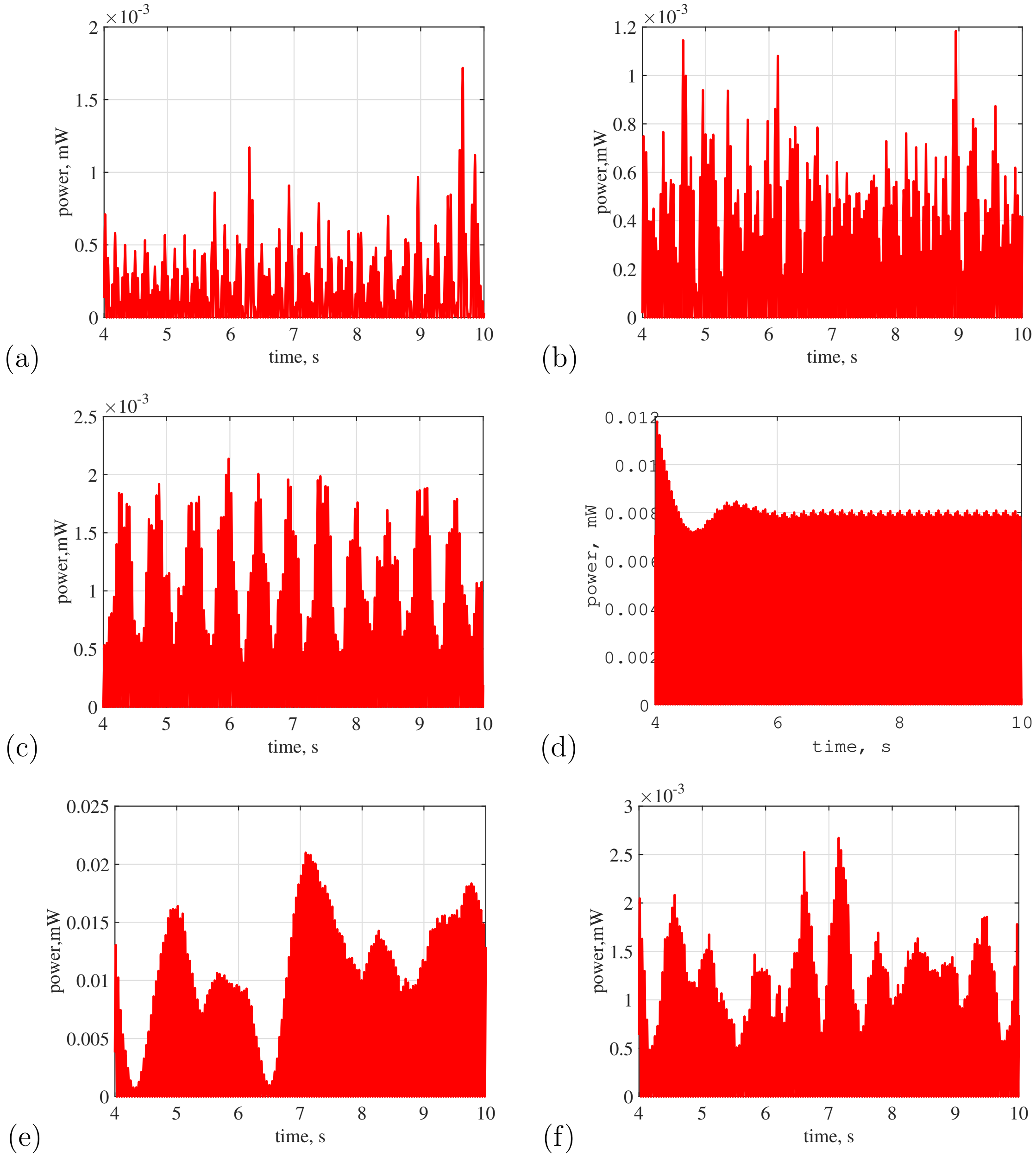

Figure 5.12: Power dissipated in the resistor for various natural frequency $\omega_n^*/(2\pi St)$. (a) 0.7, (b) 0.8, (c) 0.9, (d) 1, (e) 1.1, and (f) 1.2

ω_n^*	Square, St	$\omega_n^*/(2\pi St)$	V_{rms}, V	$P_{rms}, \mu W$
0.8796	0.2124	0.6591	0.95432	0.22768
1.005	0.2137	0.7485	1.0168	0.25848
1.0681	0.2197	0.23466	1.2214	0.37295
1.1310	0.2133	0.8439	1.5518	0.60198
1.1938	0.2072	0.24736	3.2004	1.1865
1.2566	0.2114	0.9460	3.9898	3.9797
1.3823	0.2104	1.0456	5.1339	6.5893
1.4137	0.2096	0.29617	2.5602	2.5607
1.4451	0.2074	0.29986	2.5602	1.6387
1.4765	0.2197	0.32424	2.0554	1.0562
1.508	0.2129	1.127	1.6228	0.65838
1.6336	0.2075	0.33897	0.92716	0.21490

Table 5.4: Voltage and power for different natural frequency parameter ω_n^*.

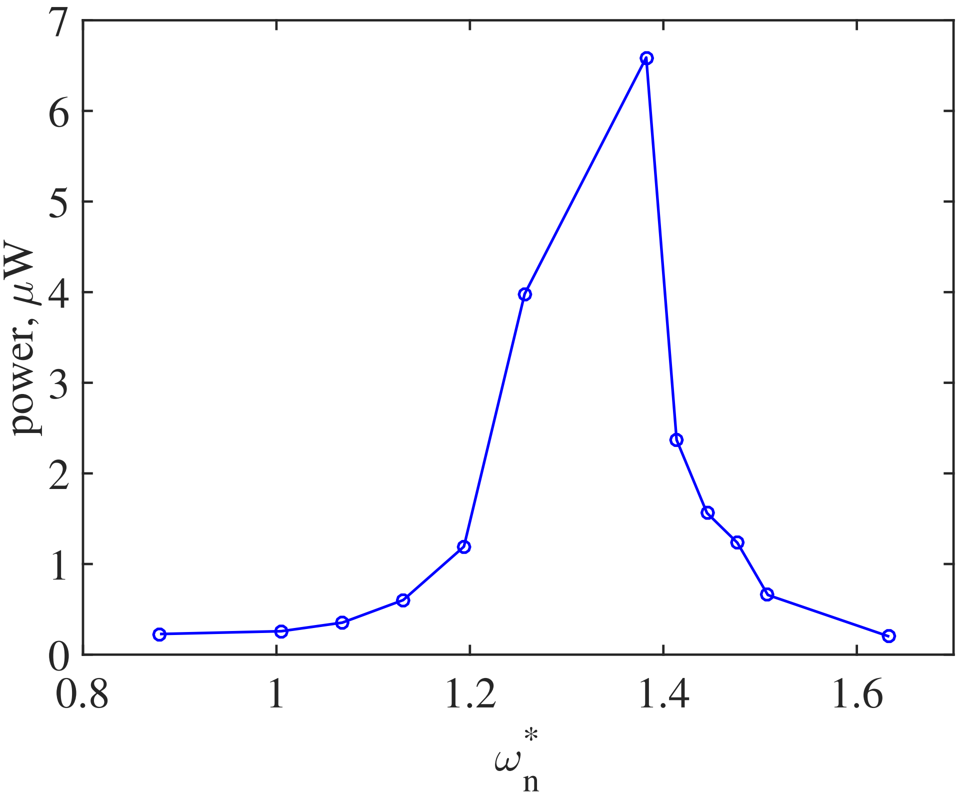

Figure 5.13: Effects of ω_n^* on RMS power.

Snap shots of vorticity contours for different natural frequency $\omega_n^*/(2\pi St)$ are depicted in figures 5.14-5.19. The figures show a very interesting picture of vortex shedding from the two cylinders. The impingement of a vortex from the circular cylinder on the square cylinder generates a vortex of opposite but weaker vortex. Because the square cylinder is smaller $(b/d = 0.75)$ than the circular cylinder, it appears that the vortices of the circular cylinder maintain their strengths in the far wake although their trajectories are significantly altered by their interaction with the vortices generated by the square cylinder. The wake of the two cylinder still contain strong vortices that can be used to excite other elastic cylinders for energy harvesting as has been done in the experimental study of this dissertation.

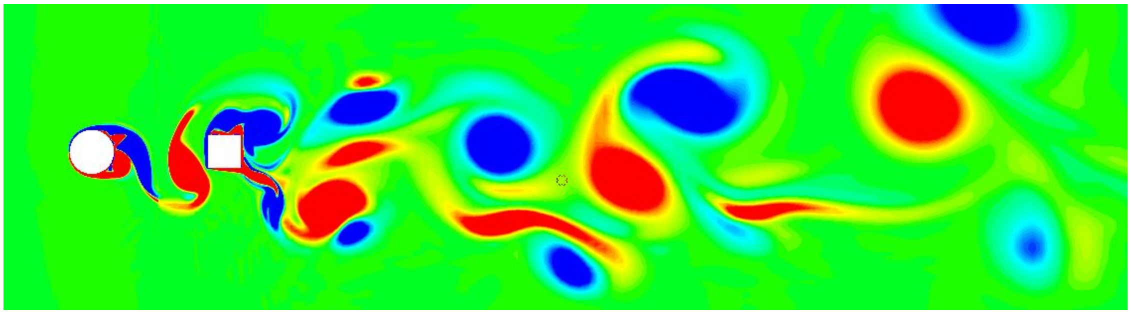

Figure 5.14: A snap shot of vorticity contours for cylinders in tandem arrangement when $\omega_n^*/(2\pi St) = 0.7$

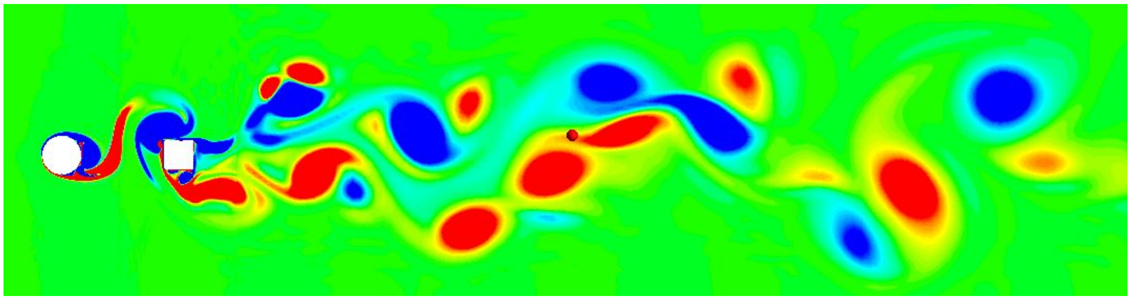

Figure 5.15: A snap shot of vorticity contours for cylinders in tandem arrangement when $\omega_n^*/(2\pi St) = 0.8$

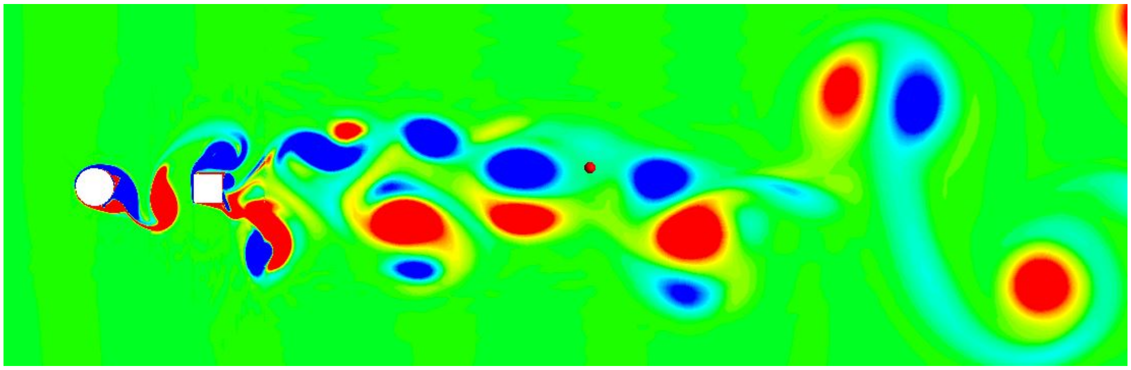

Figure 5.16: A snap shot of vorticity contours for cylinders in tandem arrangement when $\omega_n^*/(2\pi St) = 0.9$

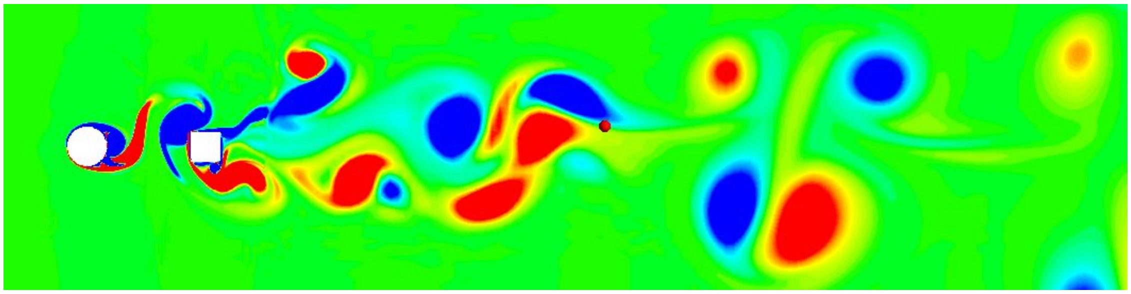

Figure 5.17: A snap shot of vorticity contours for cylinders in tandem arrangement when $\omega_n^*/(2\pi St) = 1$

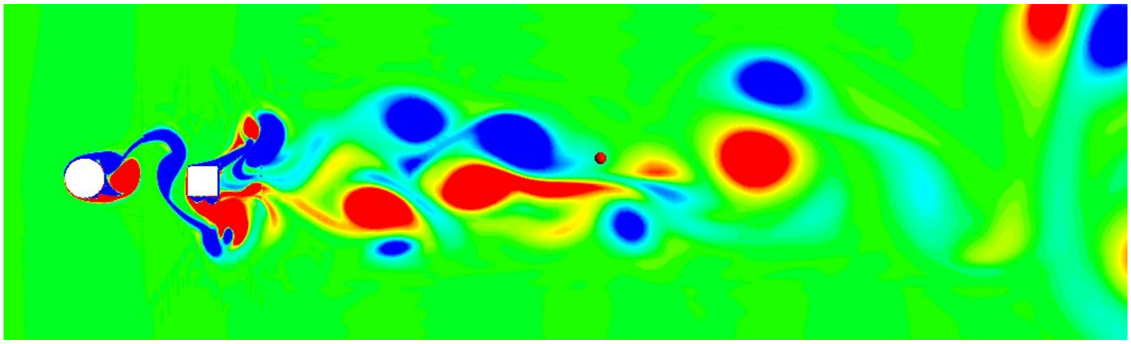

Figure 5.18: A snap shot of vorticity contours for cylinders in tandem arrangement when $\omega_n^*/(2\pi St) = 1.1$

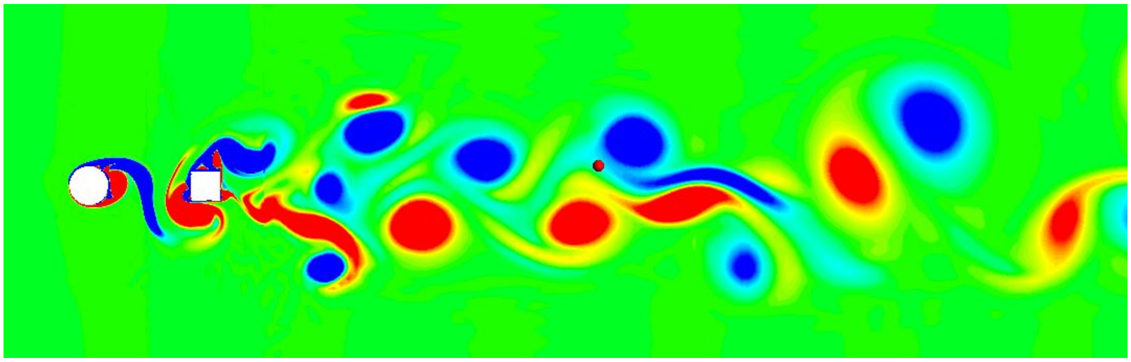

Figure 5.19: A snap shot of vorticity contours for cylinders in tandem arrangement when $\omega_n^*/(2\pi St) = 1.2$

5.3.3 Grid sensitivity

The effect of grid refinement on the system response is studied for the case $\omega_n^*/2\pi St = 1$. The mesh is refined in the region around the square cylinder by adding around 113,000 cells to the base grid. The base grid has a total of 304,592 cells whereas the finer grid has 417,812 cells. The finer mesh is shown in Figure 5.20. Comparisons of displacement of square cylinder, instantaneous voltage and power are shown in Figures 5.21, 5.22, and 5.23, respectively, for the two grids. The system response for the refined appears to be modulated by a small amplitude low frequency which is absent in the base grid response. However, volt amplitude in both grid is around 6 V. The RMS power for the base grid is 3.98 μW, and for the refined mesh it is 4.25μW. The discrepancy is less than 7%.

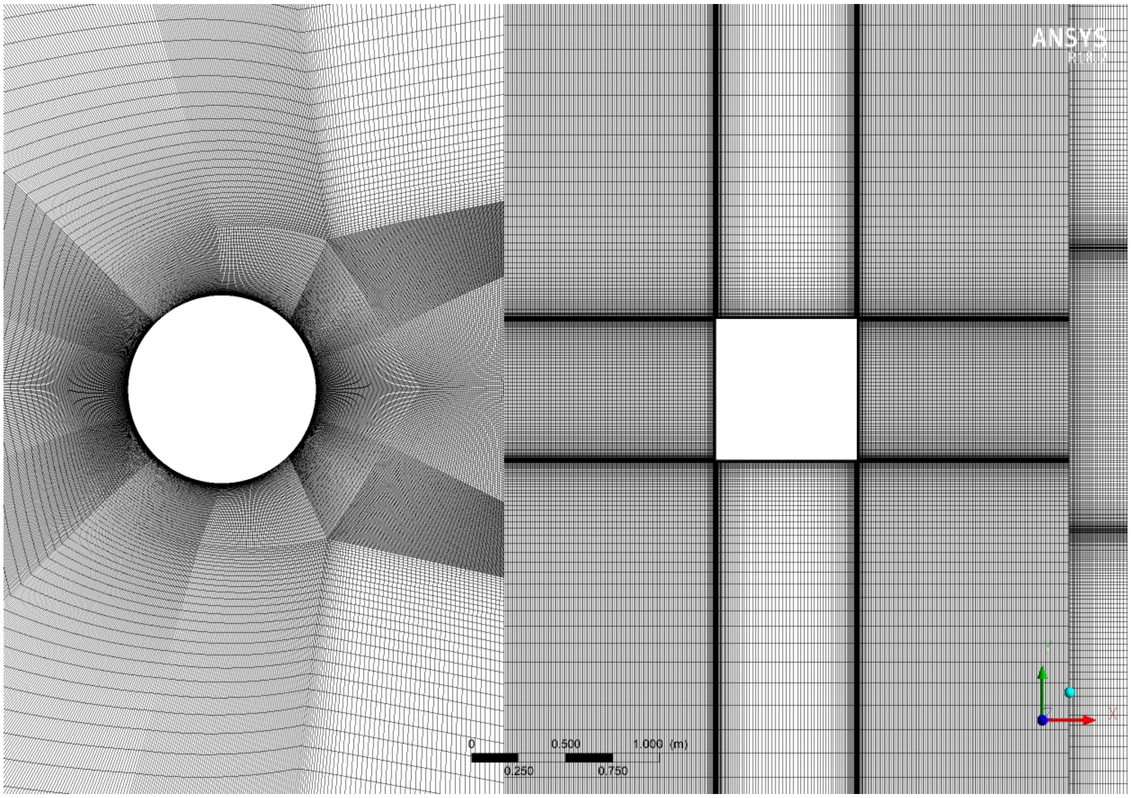

Figure 5.20: zoomed-in view of the mesh around two cylinders with total node is 417812

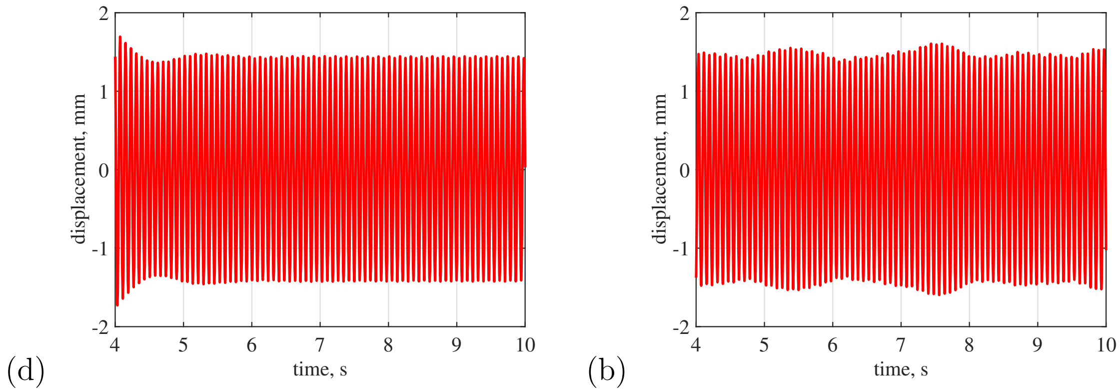

Figure 5.21: Displacement of square cylinder for natural frequency $\omega_n^*/(2\pi St) = 1$ (a) base grid, (b) fine grid

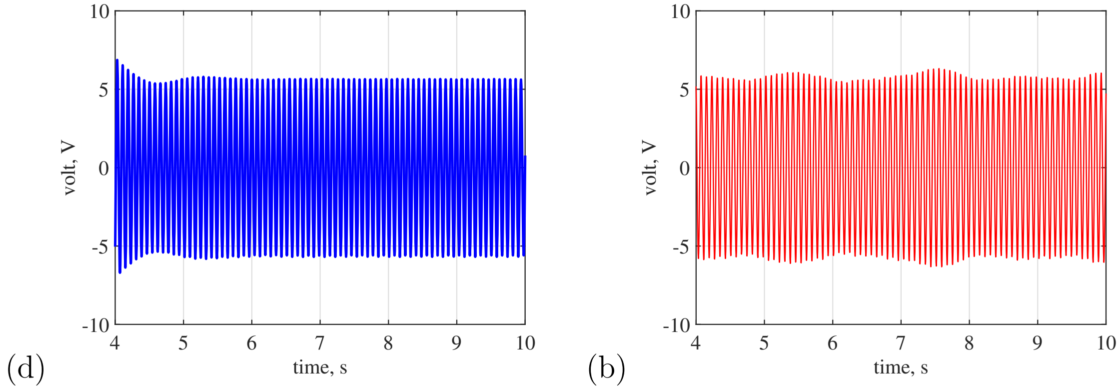

Figure 5.22: Voltage for natural frequency $\omega_n^*/(2\pi St) = 1$ (a) base grid, (b) refined grid

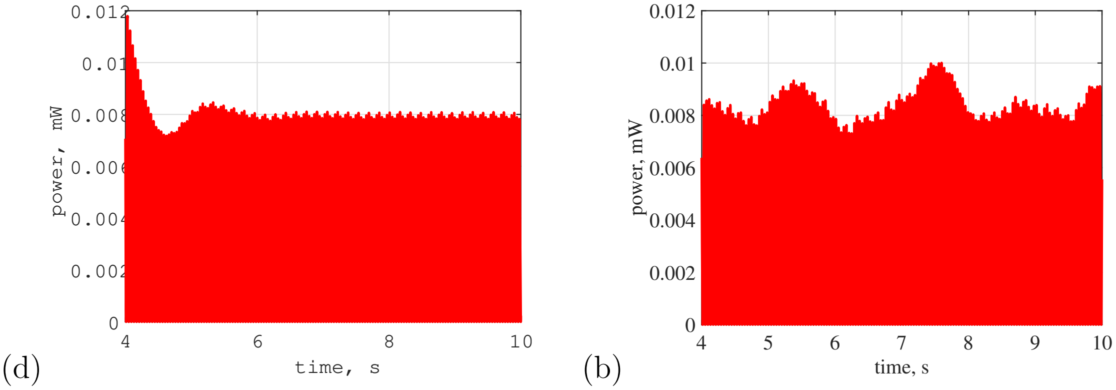

Figure 5.23: Power dissipated in the resistor for natural frequency $\omega_n^*/(2\pi St) = 1$ (a) base grid, (b) refined grid

5.3.4 Effects of mass ratio r_mn the system outputs

d	0.02 m
h	0.3 m
U_∞	1.2 m/s
ρ_∞	1.225 kg/m^3
μ_∞	1.789×10^{-5} Pa.s
θ	8×10^{-5} N/V
C_p	2×10^{-8} F
R	$4 \times 10^6 \Omega$
Re	1.6434×10^3
η_2	4.8
ω_n^*	1.2566

Table 5.5: Parameters of system for mass ratio effects.

The mass ratio r_m, which is mass of the displaced fluid to to the mass of the oscillating device, affects significantly the amplitude of the oscillations. To study the effects of the mass ratio on the system outputs, we fixed fixed certain parameters as shown in Table 5.3.4. We want the mass ratio to be on the order of 0.5. Since the device is operated in air at atmospheric conditions, the mass ratio is very small unless the volume of the square cylinder is large of its mass is small. We selected the mass values of $m = (0.14, 0.2, 0.4, 0.8) \times 10^{-3}$ kg. The corresponding mass ratios are $r_m = 0.591, 0.413, 0.207, 0.103$. These values of mass are too small for practical implementation. An alternative method for increasing the mass ratio is to operate the device in water which has much higher density than air. However, the Reynolds number will also increase for the same size device and velocity.

Figures 5.24 and 5.25 present the history of fluctuating lift on the circular and square cylinder, respectively, for different mass ratios. The magnitude of lift on the square cylinder is on the order of 1.2 for various mass ratios, but the frequency shows wide spectrum. Only for the high mass ratio is the lift is dominated by a single frequency. The non-dimensional force acting on the square cylinder is the product of the lift and the mass ratio. Figure 5.27 shows the history of the displacement of square cylinder for different mass ratio. The displacement of the square cylinder is about 10 mm, and is dominated by the vortex shedding frequency for the high mass ratio. This is in contrast to the very small displacements found in the previous section fro which the mass ratio was very small.

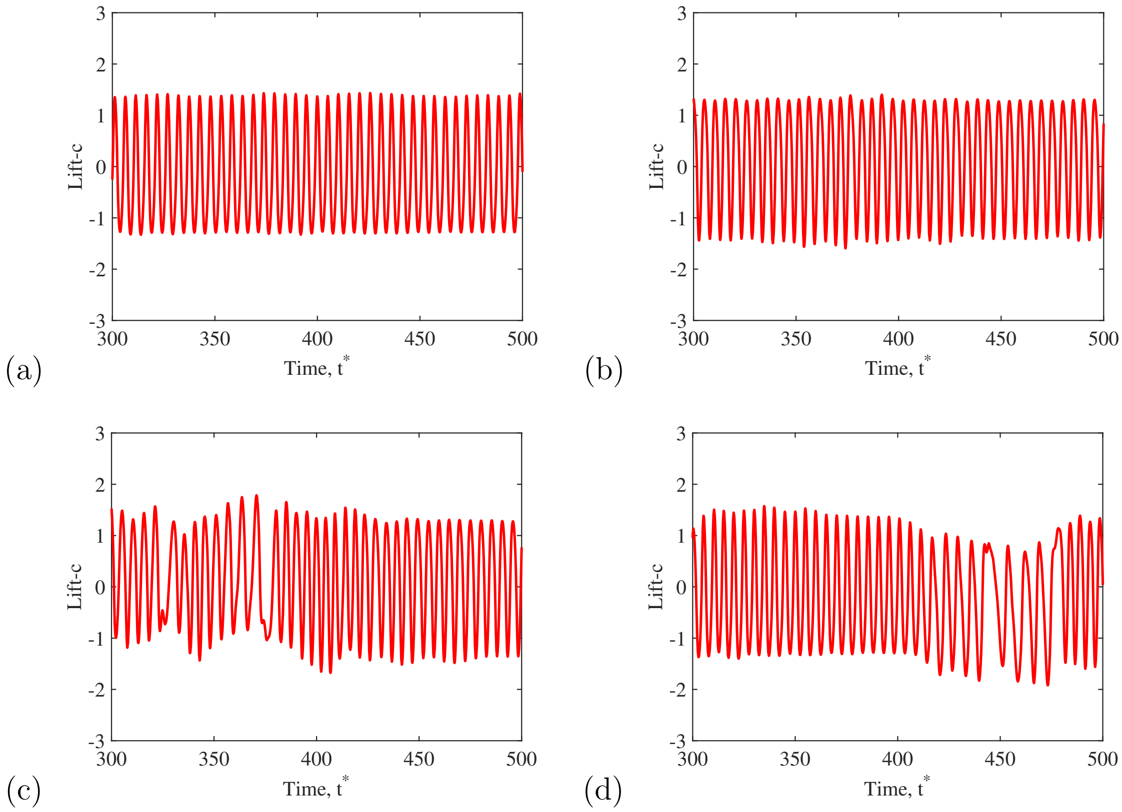

Figure 5.24: Fluctuating circular cylinder lift for various mass ratio r_m. (a) 0.591, (b) 0.413, (c) 0.207, (d) 0.103

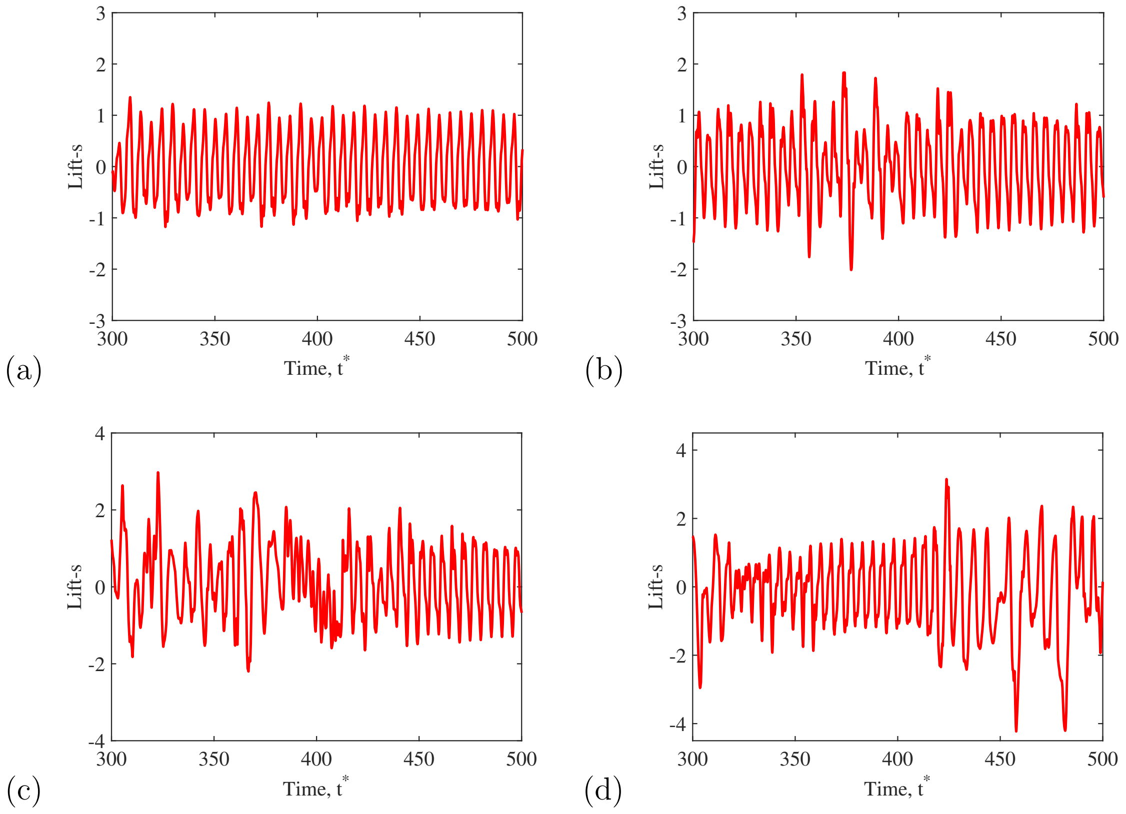

Figure 5.25: Fluctuating lift on square cylinder for various mass ratio r_m. (a) 0.591, (b) 0.413, (c) 0.207, (d) 0.103

Figure 5.26 shows lift spectrum on the square cylinder.

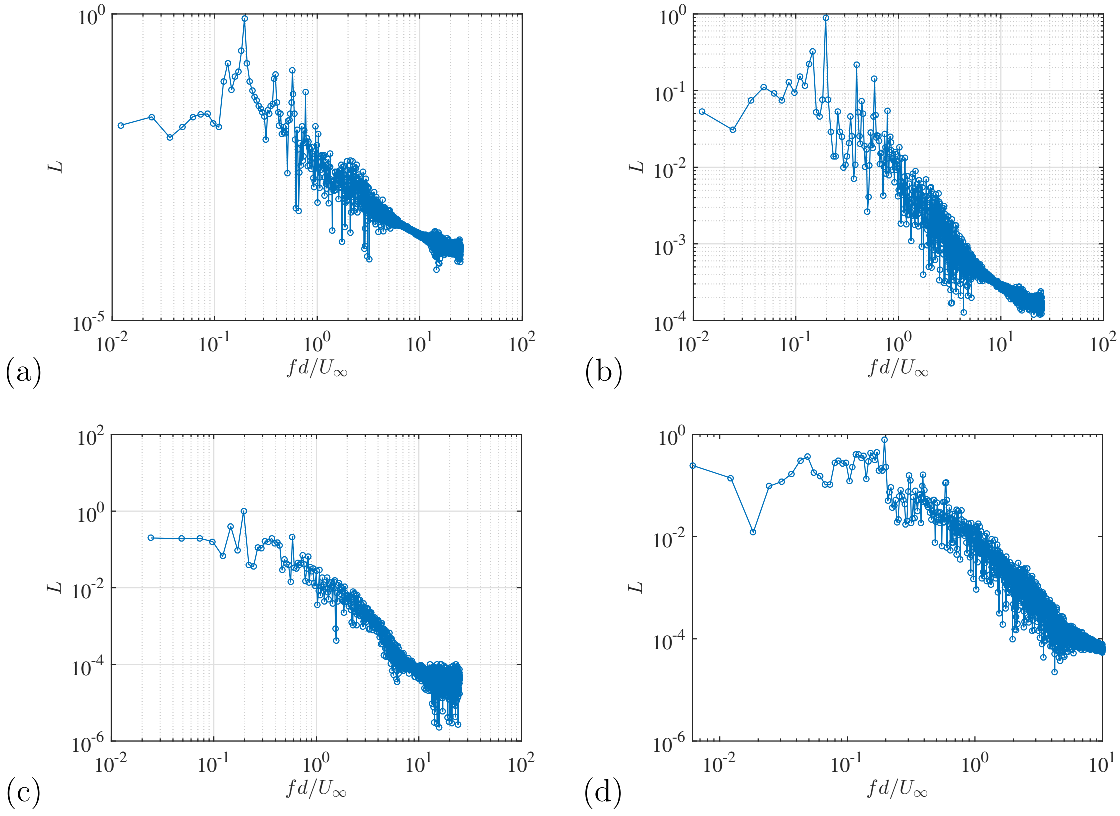

Figure 5.26: Square cylinder lift coefficient spectrum for various mass ratio r_m. (a) 0.591, (b) 0.413, (c) 0.207, (d) 0.103

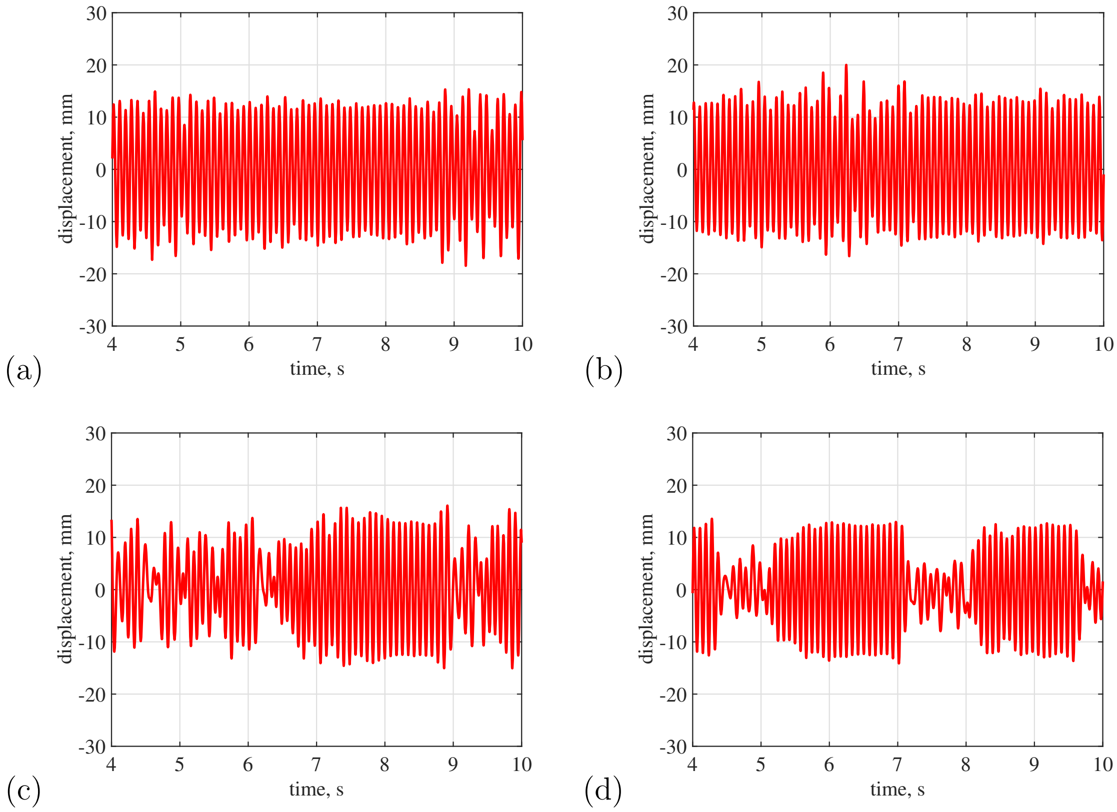

Figure 5.27: Displacement of square cylinder for various mass ratio r_m. (a) 0.591, (b) 0.413, (c) 0.207, (d) 0.103

Figure 5.3.4 shows the history of the voltage in piezoelectric element for different mass ratio. The voltage, being proportional to the velocity of the square cylinder, behaves similar to the square cylinder displacement. The volt amplitude is in the range of 50 V. The volt is nearly periodic with single frequency for the high mass ratio, but is intermittent for low mass ratio.

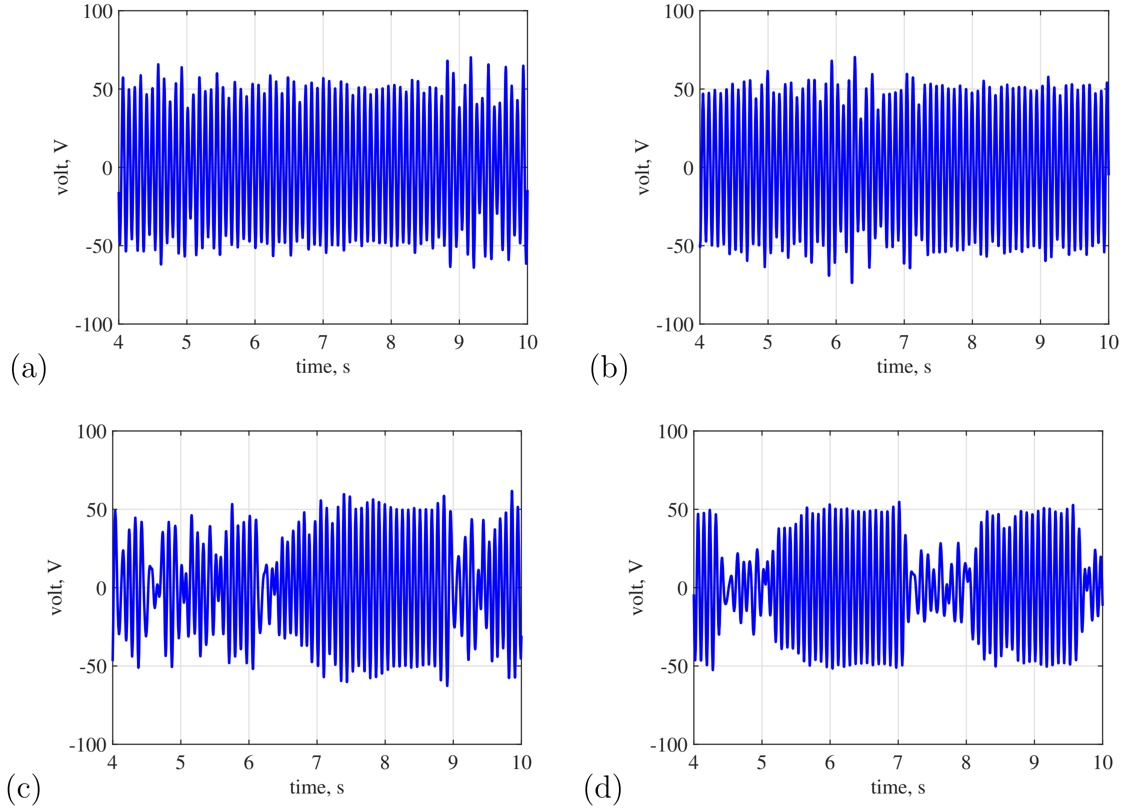

Figure 5.28: Voltage for various mass ratio r_m. (a) 0.591, (b) 0.413, (c) 0.207, (d) 0.103

Figure 5.3.4 shows the instantaneous power dissipated in the resistor for different mass ratio r_m. The highest instantaneous power of 1 mW is obtained for the high mass ratio. Table 5.6 gives a summary of the output power. The power is on the order of 0.33 mW for the high range of mass ratio.

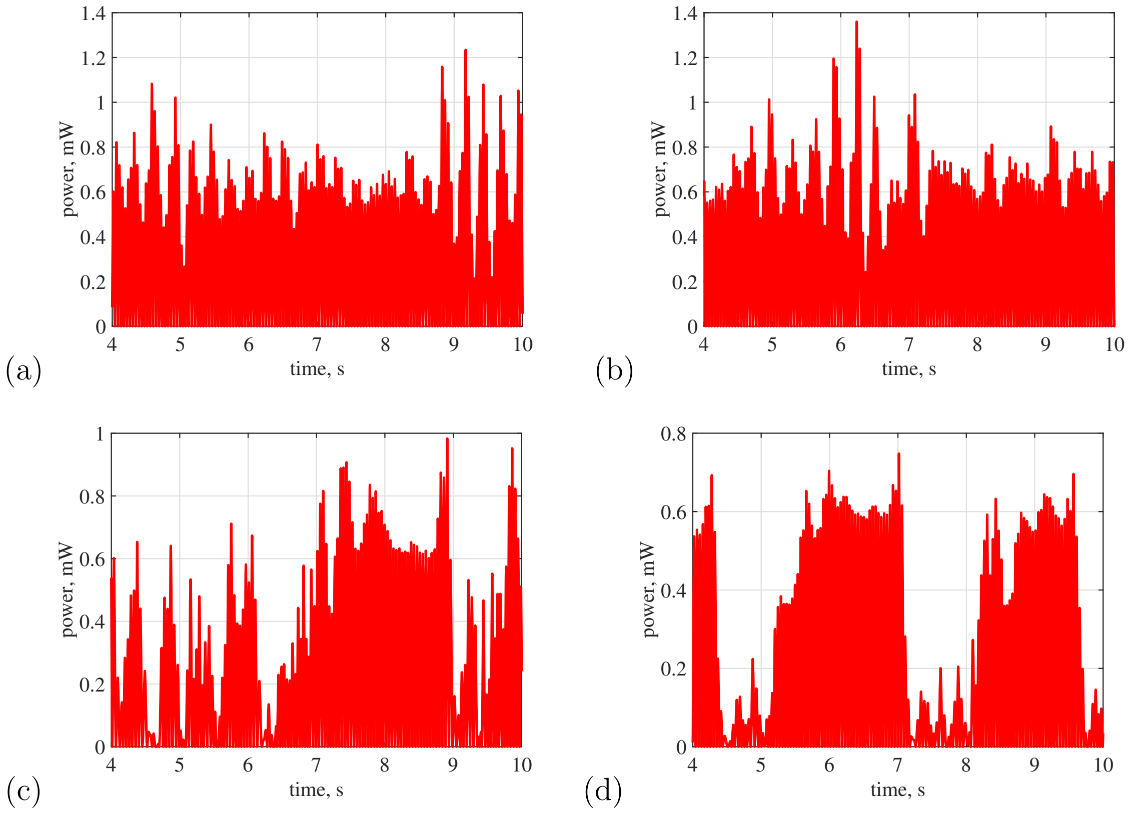

Figure 5.29: Power dissipated in the resistor for various mass ratio r_m. (a) 0.591, (b) 0.413, (c) 0.207, (d) 0.103

m (kg)	1.40E-04	2.00E-04	4.00E-04	8.00E-04
r_m	0.591	0.413	0.207	0.103
η_1	3.05	2.13	1.07	0.533
V_{rms}, V	36.427	36.800	32.712	27.108
P_{rms}, mW	0.33174	0.33857	0.26751	0.18370
St	0.193	0.1946	0.1964	0.1972
$\omega_n^*/(2\pi St)$	0.9460	0.9460	0.9460	0.9460

Table 5.6: Average power and high mass ratio

Snap shots of vorticity contours for different mass ratio r_m are depicted in figures 5.30-5.33. The figures show a very interesting picture of vortex shedding from the two cylinders. The impingement of a vortex from the circular cylinder on the square cylinder generates a vortex of opposite but weaker vortex. Because the square cylinder is smaller ($b/d = 0.75$) than the circular cylinder, it appears that the vortices of the circular cylinder maintain their strengths in the far wake although their trajectories are significantly altered by their interaction with the vortices generated by the square cylinder. The wake of the two cylinder still contain strong vortices that can be used to excite other elastic cylinders for energy harvesting as has been done in the experimental study of this dissertation.

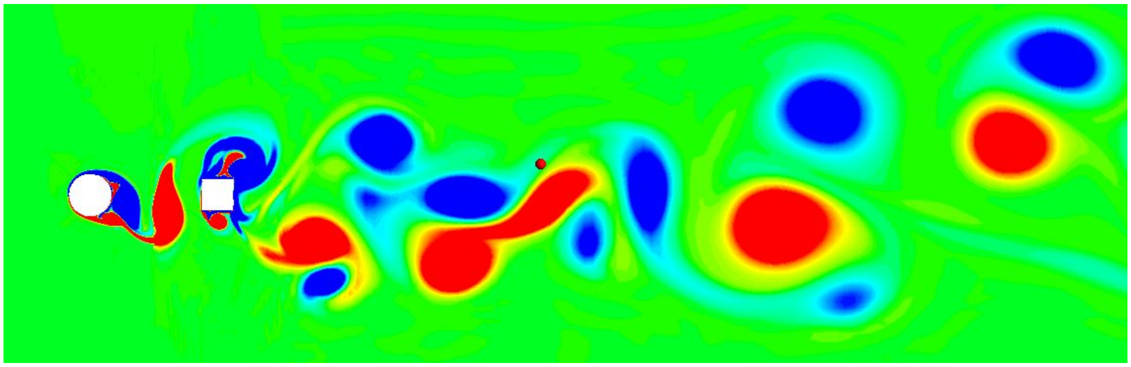

Figure 5.30: A snap shot of vorticity contours for cylinders in tandem arrangement when mass ratio r_m 0.00014

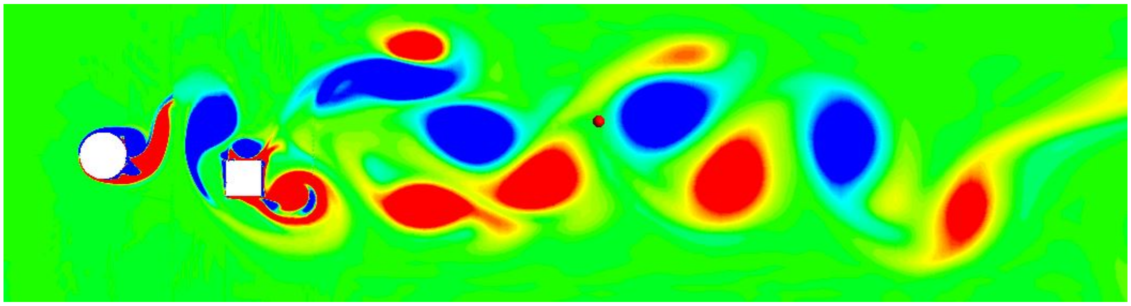

Figure 5.31: A snap shot of vorticity contours for cylinders in tandem arrangement when mass ratio r_m 0.0002

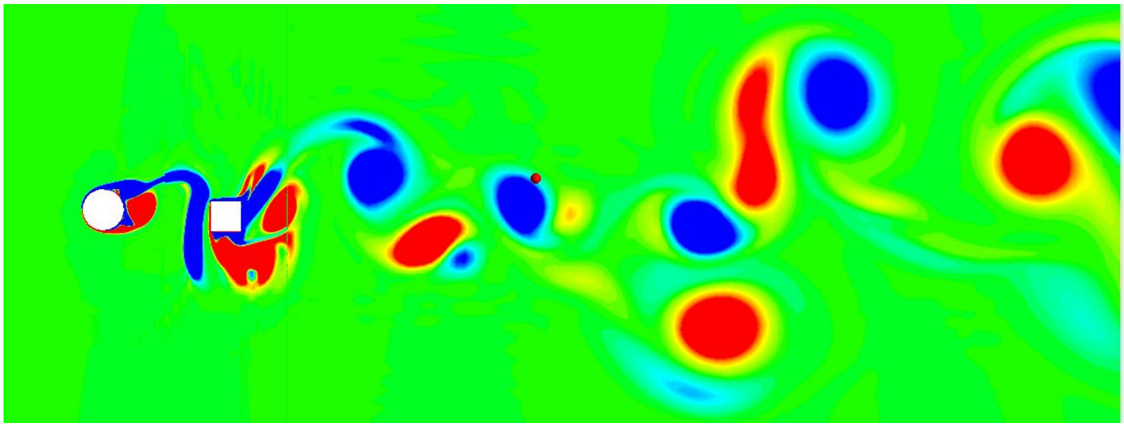

Figure 5.32: A snap shot of vorticity contours for cylinders in tandem arrangement when mass ratio r_m 0.0004

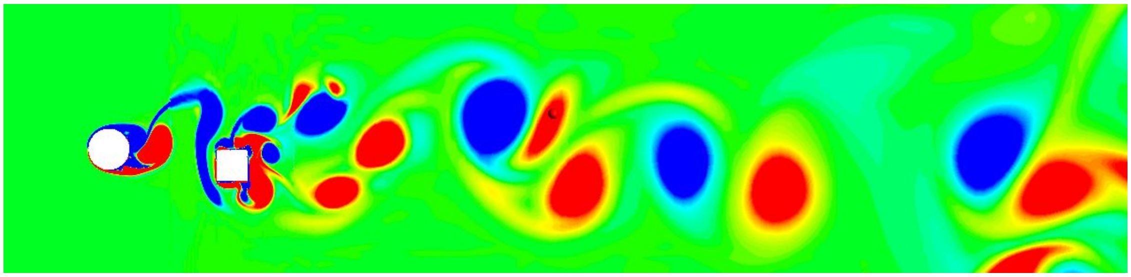

Figure 5.33: A snap shot of vorticity contours for cylinders in tandem arrangement when mass ratio r_m 0.0008

5.3.5 Simulations for experimental parameters

Laboratory experiments of Chapter three are three-dimensional with a farm of square cylinders in the wake of a circular cylinder. A computational model of such an experimental setup is beyond the scope of this dissertation, but is worth exploring in future work. In this section, we used the present two-dimensional model to simulate a system with parameters equal to those of the laboratory experiments. We conducted simulations for U_∞= 1.4 and 2.03 m/s. The parameters shown in Table 5.3.5 match the experimental setup values except the values of θ and C_p which are assumed to be those used in other simulations in this chapter. For both cases we fixed $\omega_n^*/(2\pi St) = 1.08$. With the assumed $St = 0.2$, we find $\omega_n^* = 1.3572$.

Figures 5.34 and 5.35 show the lift on the circular and square cylinders, respectively, for $U_\infty =$ 1.4 and 2.03 m/s. For the low velocity 1.4 m/s, the lift is dominated by a single frequency whereas for the higher velocity 2.04 m/s it is modulated by low frequencies. Consequently, the displacement and voltage as shown in Figures 5.37 and 5.38, respectively, for the low velocity 1.4 m/s are well behaved and dominated by single frequency wheres for the high velocity 2.03 m/s the response exhibits a beat phenomenon. The power dissipated in the load resistance is shown in Figure 5.39. Although the peak instantaneous power is higher for the higher velocity, the RMS power is higher for the low velocity as summarized in 5.8. The different response may be due to fixing $\omega_n^*/(2\pi St) = 1.08$.

d	12.7×10^{-3} m
h	254×10^{-3} m
m	5.2×10^{-3} kg
ρ_∞	1.225 kg/m^3
μ_∞	1.789×10^{-5} Pa.s
θ	8×10^{-5} N/V
C_p	2×10^{-8} F
R	$400 \times 10^3 \Omega$
r_m	5.4287×10^{-3}

Table 5.7: Input parameters of energy harvesting system.

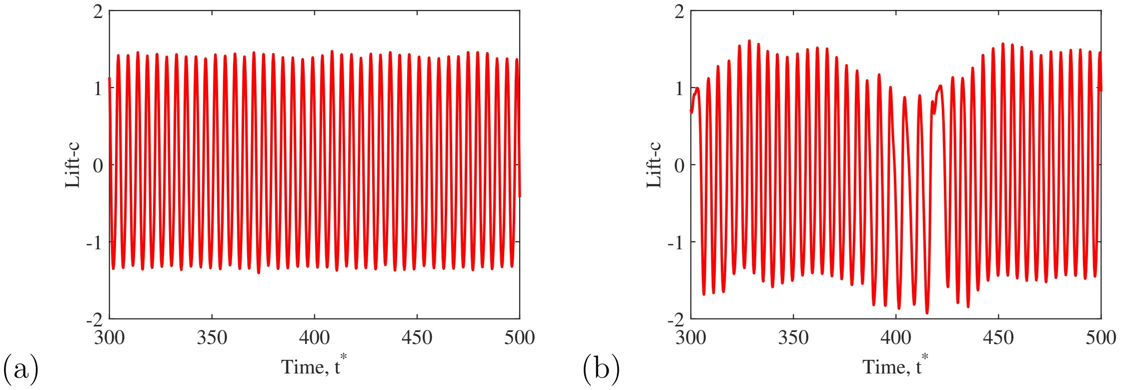

Figure 5.34: Fluctuating circular cylinder lift for various speed. (a) 1.4 m/s, (b) 2.03 m/s

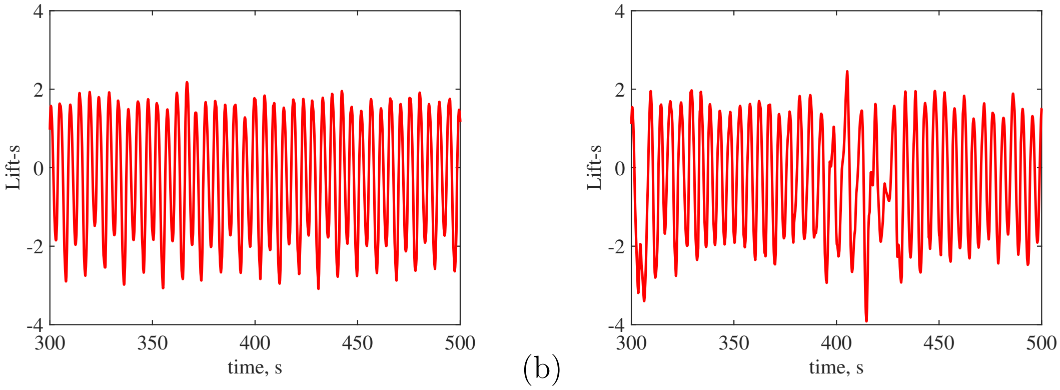

(a) (b)

Figure 5.35: Fluctuating square cylinder lift for various speed. (a) 1.4 m/s, (b) 2.03 m/s

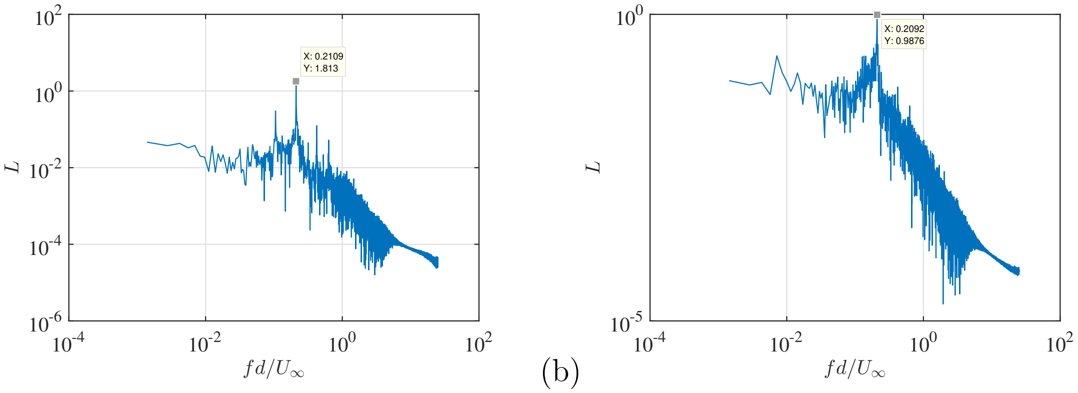

(a) (b)

Figure 5.36: Square cylinder lift coefficient spectrum for various speed. (a) 1.4 m/s, (b) 2.03 m/s

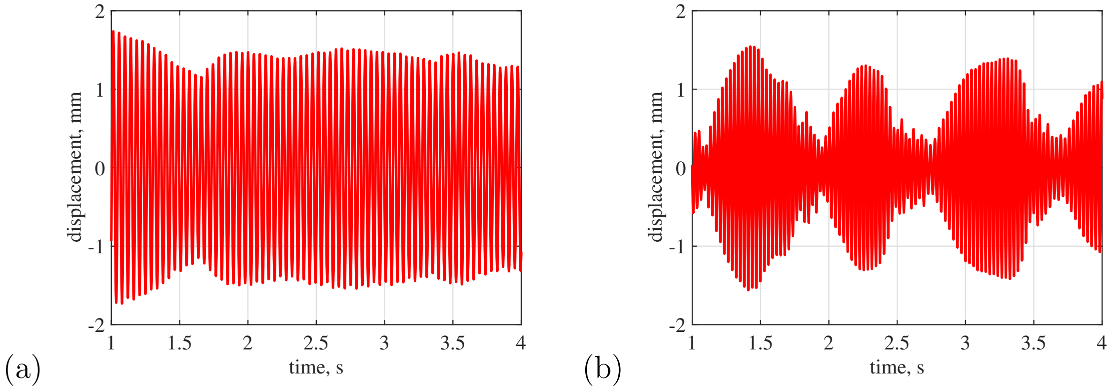

Figure 5.37: Displacement of square cylinder for various speed. (a) 1.4 m/s, (b) 2.03 m/s

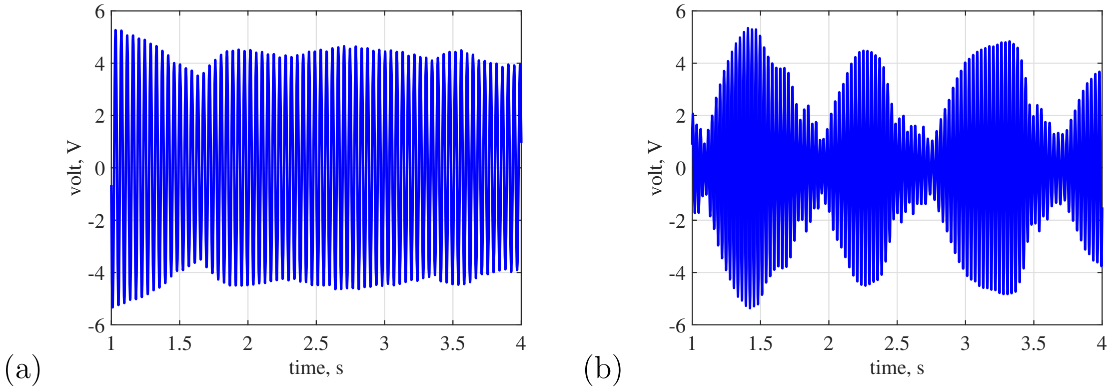

Figure 5.38: Voltage for various natural frequency various speed. (a) 1.4 m/s, (b) 2.03 m/s

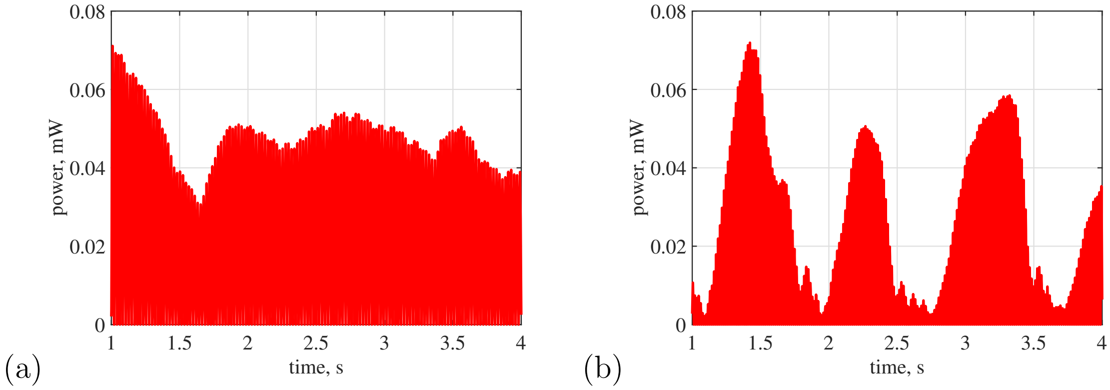

Figure 5.39: Power dissipated in the resistor for various speed. (a) 1.4 m/s, (b) 2.03 m/s

U_∞ m/s	1.4	2.03
Re	1.2175e+03	1.7653e+03
ω_n^*	1.3572e+00	1.3572e+00
Square, St	0.2192	0.2092
$\omega_n^*/(2\pi St)$	9.8590e-01	1.0330e+00
η_1	4.4659e-03	3.0800e-03
η_2	8.8189e-01	1.2787e+00
V_{rms}, V	2.7582e+00	2.4937e+00
P_{rms}, mW	1.9020e-02	1.5546e-02

Table 5.8: Results for experimental conditions at speed U_∞ (a) 1.4 m/s , (b) 2.03 m/s

5.4 Conclusions

A simple mathematical model for energy harvesting from vortex induced vibrations is developed . The vibrations of the energy harvesting element is forced by interaction with vortices generated by an upstream fixed structure. The vibrating structure is modeled by a single degree of freedom mass-spring system. The equation of motion is coupled with the circuit equation for the piezoelectric element. The instantaneous hydrodynamic load is determine by solving the incompressible Navier-Stokes equations assuming two-dimensional flow. The output voltage and power depend on thirteen dimensional parameters which are reduced to eight non-dimensional parameters.

The maximum output power is obtained when the natural frequency of the vibrating energy harvesting device (square cylinder and elastic beam) is close to the Strouhal number of vortex shedding from the fixed vortex generator. It is important that the tip mass, elastic beam dimensions and materials should be selected or adapted so that the natural frequency is equal to the vortex shedding in the incoming stream. Another important parameter that needs to be maximized is the mass ratio, which is the mass of fluid displaced by the vibrating body to its own mass. The lift on the vibrating object depends on its dimensions and fluid properties, but its amplitude response depends on its mass. Larger mass ratio gives larger amplitudes and hence larger strains in the piezoelectric element. The possibility of operating the proposed mechanism of energy harvesting in water should be explored because water density is much larger than air density at normal conditions. In such a case the added mass effects become important.

The simple model in this work can be used to select mechanical and electric parameters of the energy harvesting device to maximize the power output for certain flow conditions.

Chapter 6

Conclusions and proposed future work

6.1 Conclusions

The presented research pertains to vibration-based energy harvesting technologies in support of powering sensing and communication devices. In chapter 2, we presented a configuration that uses energy harvested from a vibration source to power communication modules of sensed vibrations of the source itself.

In chapter 3, we developed a reduced-order phenomenological model for voltage harvested from wake galloping energy - a complicated multiphysics phenomena dealing with aerodynamics, aeroelasticity, and piezoelectricity. The model consisted of a single nonlinear ordinary differential equation with linear and nonlinear damping terms that represent physical aspects related to the galloping and energy harvesting phenomena. We showed that, by modeling the variations of linear and quadratic damping terms with the flow speed, one can accurately determine the harvested voltage over a broad range of incident flow speeds.

In chapter 4, and as a first step for simulating wake galloping, we performed two-dimensional numerical simulations over a single circular cylinder at Reynolds numbers Re=525 and Re= 1000. The analysis focused on the fluctuation lift and drag coefficients and the Strouhal number as they will determine the galloping magnitude of another cylinder placed in its wake. The results were validated against results from previously published numerical simulations. Then, we simulated the patterns of the flow over a square cylinder placed in the wake of an upstream circular cylinder at Re= 1634. Computations were carried out for five values of the separation distance between the cylinders' centers, namely $s = 2d, 3d, 4d, 5d$ and $6d$, where d is the diameter of the circular cylinder. The fluctuating lift and drag coefficients and the Strouhal number were analyzed as a function of the cylinders' spacing. The analysis showed that for $s \leq 2d$, the two cylinders acted as one long bluff body as the shed vortices impinge on the square cylinder before fully formed. The results showed that the lift on the square cylinder attains its maximum when the spacing is $2d$.

In chapter 5, we developed a mathematical model for energy harvesting from wake galloping. The motion of the galloping cylinder was modeled as that of a single degree of freedom mass-spring system. The equation of motion was coupled with the circuit equation for the piezoelectric element. We determined that the output voltage and power depend on thirteen dimensional parameters that were subsequently reduced to eight non-dimensional parameters. The maximum output power was obtained when the natural frequency of the vibrating energy harvesting device (square cylinder and elastic beam) is close to the Strouhal number of vortex shedding from the upstream circular cylinder. The results show that the tip mass, elastic beam dimensions and materials should be selected or adapted so that the natural frequency is equal to the vortex shedding frequency. Another important parameter that need to be optimized is the mass ratio, defined as the ratio of the mass of fluid displaced by the vibrating cylinder to its own mass. It was determined that a larger mass ratio yields larger amplitudes and hence larger strains in the piezoelectric element, which presents the potential to optimize the energy harvesting based on the fluid medium.

6.2 Future work

Proposed future work that can impact the development of energy harvesting technologies from galloping structures include:

- Expanding the current two-dimensional simulations at Re=1000 to three-dimensional simulations at higher Reynolds numbers.
- Expanding the simulations proposed under the above point to design a farm for energy harvesting from wake galloping elements.

  It is important to note that both of the above expansions will require implementation of turbulence modeling in the numerical simulations and experimental validation.

Chapter 7

Supplementary material: Approximate solution of phenomenological model of piezoelectric energy harvesting from galloping oscillations

Details of the approximate solution of the phenomenological model using the method of multiple scales [35, 36] are presented below. The phenomenological model is written as

$$\ddot{V} + \Omega^2 V - \epsilon \hat{\mu}_l \dot{V} + \epsilon \hat{\mu_2} \dot{V} |\dot{V}| = 0 \tag{7.1}$$

Here Ω, μ_l, and μ_2 are respectively the oscillation frequency, linear damping coefficient, and quadratic damping coefficient. We write the solution of voltage till $\epsilon-$order as

$$V(t; \epsilon) = V_0(T_0, T_1) + \epsilon V_1(T_0, T_1) \tag{7.2a}$$

and note that

$$\dot{V} = \frac{\partial V_0}{\partial T_0} + \epsilon \frac{\partial V_0}{\partial T_1} + \epsilon \frac{\partial V_1}{\partial T_0} \equiv D_0 V_0 + \epsilon D_1 V_0 + \epsilon D_0 V_1, \tag{7.2b}$$

and

$$\ddot{V} = \frac{\partial^2 V_0}{\partial T_0^2} + 2\epsilon \frac{\partial^2 V_0}{\partial T_1 \partial T_0} + \epsilon \frac{\partial^2 V_1}{\partial T_0^2}$$

$$\equiv D_0^2 V_0 + 2\epsilon D_0 D_1 V_0 + \epsilon D_0^2 V_1 \tag{7.2c}$$

Substituting equations 7.2a-7.2c into equation 7.1 and separating ϵ^0, and ϵ^1 order terms, we obtain

ϵ^0-*order equation*

$$D_0^2 V_0 + \Omega^2 V_0 = 0, \text{ and} \tag{7.3a}$$

ϵ^1-*order equation*

$$D_0^2 V_1 + \Omega^2 V_1 = -2 D_0 D_1 V_0 + \mu_l D_0 V_0$$

$$- \mu_2 D_0 V_0 |D_0 V_0| \tag{7.3b}$$

From ϵ^0-order equation, we obtain

$$V_0(T_0, T_1) = A(T_1) e^{j\Omega T_0} + cc \tag{7.4}$$

where $A(T_1)$ is the complex amplitude, cc denotes the complex conjugate, and $j = \sqrt{-1}$. Substituting equation 7.4 in ϵ^1-order equation 7.3b and eliminating secular terms, we obtain the complex amplitude modulation equation as

$$D_1 A = \frac{1}{2\Omega} \left[\Omega \mu_1 A + j \mu_2 g_1 \right] \tag{7.5}$$

and the solution for V_1 as

$$V_1 = \frac{g_2}{3\Omega^2} \mu_2 e^{2j\Omega T_0} + \frac{g_3}{8\Omega^2} \mu_2 e^{3j\Omega T_0} + \text{H.O.T} + cc \tag{7.6}$$

In writing equations 7.5 and 7.6, we used that [37,88]

$$D_0 q_0 |D_0 q_0| = \sum_{n=-\infty}^{\infty} g_n e^{jn\Omega T_0} \tag{7.7}$$

Representing complex amplitude in the polar form as $A(T_1) = a(T_1)e^{j\beta(T_1)}$, we obtain the coefficients g_1, g_2, and g_3 as

$$g_1 = \frac{4}{3\pi} j\Omega^2 a^2 e^{j\beta}, \;\; g_3 = \frac{4}{15\pi}\Omega^2 a^2 e^{-3j\beta}, \tag{7.8a}$$

and

$$g_{2m} = 0 \;\forall\; m = 1, 2, 3, \ldots \tag{7.8b}$$

where a, and β respectively represent the absolute amplitude and phase. From the expressions for g_1, g_2, and g_3 we obtain the approximate solution as

$$V(t,\epsilon) = a(t,\epsilon)\cos[\Omega t + \beta] + \frac{a(t,\epsilon)^2 \mu_2}{15\pi} \sin\left[3\Omega t + 3\beta\right] \tag{7.9a}$$

where β is a constant phase and the amplitude a is governed by the amplitude modulation relation determined as

$$\dot{a}(t,\epsilon) = \frac{1}{2}\mu_l a(t,\epsilon) - \frac{4}{3\pi} a(t,\epsilon)^2 \Omega \mu_2 \tag{7.9b}$$

By imposing the steady state condition on equation 7.9b in conjunction with the approximate solution presented in equation 7.9a, we obtain

$$\mu_2 = 15\pi \frac{V_{3\Omega}}{V_{\Omega}^2}, \text{ and} \tag{7.10a}$$

$$\mu_l = \frac{8}{3\pi}\Omega \mu_2 V_{\Omega} \tag{7.10b}$$

where $V_{\Omega} = a_0$, and $V_{3\Omega} = a_0^2 \mu_2 / 15\pi$; and a_0 is the steady state amplitude, which is the nontrivial fixed point of equation 7.9b.

Bibliography

[1] Paul D Mitcheson, Peng Miao, Bernard H Stark, EM Yeatman, AS Holmes, and TC Green. Mems electrostatic micropower generator for low frequency operation. *Sensors and Actuators A: Physical*, 115(2-3):523–529, 2004.

[2] Peter Glynne-Jones, Michael John Tudor, Stephen Paul Beeby, and Neil M White. An electromagnetic, vibration-powered generator for intelligent sensor systems. *Sensors and Actuators A: Physical*, 110(1-3):344–349, 2004.

[3] Steven R Anton and Henry A Sodano. A review of power harvesting using piezoelectric materials (2003–2006). *Smart materials and Structures*, 16(3):R1, 2007.

[4] Alper Erturk. *Electromechanical modeling of piezoelectric energy harvesters*. PhD thesis, Virginia Tech, 2009.

[5] A Abdelkefi, AH Nayfeh, and MR Hajj. Design of piezoaeroelastic energy harvesters. *Nonlinear Dynamics*, 68(4):519–530, 2012.

[6] Abdulmohsen A Alothman, Mohamed Y Zakaria, Muhammad R Hajj, and Sami F Masri. Use of thermoelectric generator for water flow metering. *Applied Physics Letters*, 109(3):033903, 2016.

[7] Farhan Simjee and Pai H Chou. Everlast: long-life, supercapacitor-operated wireless sensor node. In *Proceedings of the 2006 international symposium on Low power electronics and design*, pages 197–202, 2006.

[8] ZD Deng, Thomas J Carlson, Huidong Li, Jie Xiao, Mitchell J Myjak, Jun Lu, Jayson J Martinez, Christa M Woodley, Mark A Weiland, and Matthew B Eppard. An injectable acoustic transmitter for juvenile salmon. *Scientific reports*, 5:8111, 2015.

[9] Huicong Liu, Songsong Zhang, Ramprakash Kathiresan, Takeshi Kobayashi, and Chengkuo Lee. Development of piezoelectric microcantilever flow sensor with wind-driven energy harvesting capability. *Applied Physics Letters*, 100(22):223905, 2012.

[10] Huidong Li, Chuan Tian, Jun Lu, Mitchell J Myjak, Jayson J Martinez, Richard S Brown, and Zhiqun Daniel Deng. An energy harvesting underwater acoustic transmitter for aquatic animals. *Scientific reports*, 6:33804, 2016.

[11] Yen Kheng Tan and Sanjib Kumar Panda. Energy harvesting from hybrid indoor ambient light and thermal energy sources for enhanced performance of wireless sensor nodes. *IEEE Transactions on Industrial Electronics*, 58(9):4424–4435, 2011.

[12] Jamal S Alrowaijeh and Muhammad R Hajj. Autonomous self-powered water meter. *Applied Physics Letters*, 113(3):033902, 2018.

[13] Alper Erturk, WGR Vieira, C De Marqui Jr, and Daniel J Inman. On the energy harvesting potential of piezoaeroelastic systems. *Applied physics letters*, 96(18):184103, 2010.

[14] Shuguang Li, Jianping Yuan, and Hod Lipson. Ambient wind energy harvesting using cross-flow fluttering. *Journal of Applied Physics*, 109(2):026104, 2011.

[15] Mohamed Y. Zakaria, Mohammad Y. Al-Haik, and Muhammad R. Hajj. Experimental analysis of energy harvesting from self-induced flutter of a composite beam. *Applied Physics Letters*, 107(2):023901, 2015.

[16] Soon-Duck Kwon. A t-shaped piezoelectric cantilever for fluid energy harvesting. *Applied Physics Letters*, 97(16):164102, 2010.

[17] H. L. Dai, A. Abdelkefi, Y. Yang, and L. Wang. Orientation of bluff body for designing efficient energy harvesters from vortex-induced vibrations. *Applied Physics Letters*, 108(5):053902, 2016.

[18] O. Goushcha, N. Elvin, and Y. Andreopoulos. Interactions of vortices with a flexible beam with applications in fluidic energy harvesting. *Applied Physics Letters*, 104(2):021919, 2014.

[19] Gang Hu, K. T. Tse, K. C. S. Kwok, Jie Song, and Yuan Lyu. Aerodynamic modification to a circular cylinder to enhance the piezoelectric wind energy harvesting. *Applied Physics Letters*, 109(19):193902, 2016.

[20] Abdessattar Abdelkefi and Muhammad R Hajj. Performance enhancement of wing-based piezoaeroelastic energy harvesting through freeplay nonlinearity. *Theoretical and Applied Mechanics Letters*, 3(4):041001, 2013.

[21] Yaowen Yang, Liya Zhao, and Lihua Tang. Comparative study of tip cross-sections for efficient galloping energy harvesting. *Applied Physics Letters*, 102(6):064105, 2013.

[22] A Bibo and MF Daqaq. On the optimal performance and universal design curves of galloping energy harvesters. *Applied Physics Letters*, 104(2):023901, 2014.

[23] AH Alhadidi and MF Daqaq. A broadband bi-stable flow energy harvester based on the wake-galloping phenomenon. *Applied Physics Letters*, 109(3):033904, 2016.

[24] Gang Hu, K. T. Tse, and K. C. S. Kwok. Enhanced performance of wind energy harvester by aerodynamic treatment of a square prism. *Applied Physics Letters*, 108(12):123901, 2016.

[25] Feng-Rui Liu, Hong-Xiang Zou, Wen-Ming Zhang, Zhi-Ke Peng, and Guang Meng. Y-type three-blade bluff body for wind energy harvesting. *Applied Physics Letters*, 112(23):233903, 2018.

[26] Xuefeng He, Xiaokang Yang, and Senlin Jiang. Enhancement of wind energy harvesting by interaction between vortex-induced vibration and galloping. *Applied Physics Letters*, 112(3):033901, 2018.

[27] GV Parkinson and JD Smith. The square prism as an aeroelastic non-linear oscillator. *The Quarterly Journal of Mechanics and Applied Mathematics*, 17(2):225–239, 1964.

[28] Milos Novak. Galloping oscillations of prismatic structures. *Journal of Engineering Mechanics*, 1972.

[29] Michael P Païdoussis, Stuart J Price, and Emmanuel De Langre. *Fluid-structure interactions: cross-flow-induced instabilities.* Cambridge University Press, 2010.

[30] S Tucker Harvey, IA Khovanov, and P Denissenko. A galloping energy harvester with flow attachment. *Applied Physics Letters*, 114(10):104103, 2019.

[31] Richard Evelyn Donohue Bishop and AY Hassan. The lift and drag forces on a circular cylinder oscillating in a flowing fluid. *Proceedings of the Royal Society of London. Series A. Mathematical and Physical Sciences*, 277(1368):51–75, 1964.

[32] Ronald T Hartlen and Iain G Currie. Lift-oscillator model of vortex-induced vibration. *Journal of the Engineering Mechanics Division*, 96(5):577–591, 1970.

[33] RA Skop and OM Griffin. A model for the vortex-excited resonant response of bluff cylinders. *Journal of Sound and Vibration*, 27(2):225–233, 1973.

[34] Ali H Nayfeh, Farouk Owis, and Muhammad R Hajj. A model for the coupled lift and drag on a circular cylinder. In *ASME 2003 International Design Engineering Technical Conferences and Computers and Information in Engineering Conference*, pages 1289–1296. American Society of Mechanical Engineers, 2003.

[35] Ali H Nayfeh and Dean T Mook. *Nonlinear oscillations.* John Wiley & Sons, 2008.

[36] Ali H Nayfeh. *Introduction to perturbation techniques.* John Wiley & Sons, 2011.

[37] MR Hajj, J Fung, AH Nayfeh, and SO'F Fahey. Damping identification using perturbation techniques and higher-order spectra. *Nonlinear Dynamics*, 23(2):189–203, 2000.

[38] Shashank Priya and Daniel J Inman. *Energy harvesting technologies*, volume 21. Springer, 2009.

[39] Henry A Sodano, Daniel J Inman, and Gyuhae Park. A review of power harvesting from vibration using piezoelectric materials. *Shock and Vibration Digest*, 36(3):197–206, 2004.

[40] Andrew Truitt and S Nima Mahmoodi. A review on active wind energy harvesting designs. *International Journal of Precision Engineering and Manufacturing*, 14(9):1667–1675, 2013.

[41] Abdessattar Abdelkefi. Aeroelastic energy harvesting: A review. *International Journal of Engineering Science*, 100:112–135, 2016.

[42] Santiago Orrego, Kourosh Shoele, Andre Ruas, Kyle Doran, Brett Caggiano, Rajat Mittal, and Sung Hoon Kang. Harvesting ambient wind energy with an inverted piezoelectric flag. *Applied energy*, 194:212–222, 2017.

[43] Sourabh V Apte, Mathieu Martin, and Neelesh A Patankar. A numerical method for fully resolved simulation (frs) of rigid particle–flow interactions in complex flows. *Journal of Computational Physics*, 228(8):2712–2738, 2009.

[44] Chloe Mimeau, Federico Gallizio, Georges-Henri Cottet, and Iraj Mortazavi. Vortex penalization method for bluff body flows. *International Journal for Numerical Methods in Fluids*, 79(2):55–83, 2015.

[45] Imran Akhtar. *Parallel simulations, reduced-order modeling, and feedback control of vortex shedding using fluidic actuators.* PhD thesis, Virginia Tech, 2008.

[46] S Mittal and V Kumar. Flow-induced vibrations of a light circular cylinder at reynolds numbers 103to 104. *Journal of sound and vibration*, 245(5):923–946, 2001.

[47] Bryce Sharman, Fu-Sang Lien, Lars Davidson, and Christoffer Norberg. Numerical predictions of low reynolds number flows over two tandem circular cylinders. *International Journal for Numerical Methods in Fluids*, 47(5):423–447, 2005.

[48] JR Meneghini, F Saltara, CLR Siqueira, and JA Ferrari. Numerical simulation of flow interference between two circular cylinders in tandem and side-by-side arrangements. *Journal of fluids and structures*, 15(2):327–350, 2001.

[49] Abdessattar Abdelkefi. *Global nonlinear analysis of piezoelectric energy harvesting from ambient and aeroelastic vibrations.* PhD thesis, Virginia Tech, 2012.

[50] Daniel J Inman and Benjamin L Grisso. Towards autonomous sensing. In *Smart Structures and Materials 2006: Sensors and Smart Structures Technologies for Civil, Mechanical, and Aerospace Systems*, volume 6174, page 61740T. International Society for Optics and Photonics, 2006.

[51] Abdessattar Abdelkefi and Mehdi Ghommem. Piezoelectric energy harvesting from morphing wing motions for micro air vehicles. *Theoretical and Applied Mechanics Letters*, 3(5):052004, 2013.

[52] Hossein Roshani, Samer Dessouky, Arturo Montoya, and AT Papagiannakis. Energy harvesting from asphalt pavement roadways vehicle-induced stresses: A feasibility study. *Applied Energy*, 182:210–218, 2016.

[53] HL Dai, A Abdelkefi, and L Wang. Piezoelectric energy harvesting from concurrent vortex-induced vibrations and base excitations. *Nonlinear Dynamics*, 77(3):967–981, 2014.

[54] Daniel Hoffmann, Bernd Folkmer, and Yiannos Manoli. Fabrication, characterization and modelling of electrostatic micro-generators. *Journal of Micromechanics and Microengineering*, 19(9):094001, 2009.

[55] George W Taylor, Joseph R Burns, SA Kammann, William B Powers, and Thomas R Welsh. The energy harvesting eel: a small subsurface ocean/river power generator. *IEEE journal of oceanic engineering*, 26(4):539–547, 2001.

[56] S Pobering, M Menacher, S Ebermaier, and N Schwesinger. Piezoelectric power conversion with self-induced oscillation. *PowerMEMS*, 2009:384–387, 2009.

[57] S Pobering, S Ebermeyer, and N Schwesinger. Generation of electrical energy using short piezoelectric cantilevers in flowing media. In *Active and Passive Smart Structures*

and Integrated Systems 2009, volume 7288, page 728807. International Society for Optics and Photonics, 2009.

[58] Enrico Bischur, Sebastian Pobering, Markus Menacher, and Norbert Schwesinger. Flow driven vibration energy harvester. In *ASME 2010 Conference on Smart Materials, Adaptive Structures and Intelligent Systems*, pages 523–528. American Society of Mechanical Engineers, 2010.

[59] Huseyin Dogus Akaydin, Niell Elvin, and Yiannis Andreopoulos. Energy harvesting from highly unsteady fluid flows using piezoelectric materials. *Journal of Intelligent Material Systems and Structures*, 21(13):1263–1278, 2010.

[60] Huseyin Dogus Akaydin, Niell Elvin, and Yiannis Andreopoulos. Experimental study of a self-excited piezoelectric energy harvester. In *ASME 2010 Conference on Smart Materials, Adaptive Structures and Intelligent Systems*, pages 179–185. American Society of Mechanical Engineers, 2010.

[61] Sebastian Pobering. Energy harvesting under induced best conditions. In *Structural Dynamics and Renewable Energy, Volume 1*, pages 239–245. Springer, 2011.

[62] William B Hobbs and David L Hu. Tree-inspired piezoelectric energy harvesting. *Journal of fluids and Structures*, 28:103–114, 2012.

[63] Xiaotong Gao, Wei-Heng Shih, and Wan Y Shih. Flow energy harvesting using piezoelectric cantilevers with cylindrical extension. *IEEE Transactions on Industrial Electronics*, 60(3):1116–1118, 2013.

[64] William McKinney and James DeLaurier. Wingmill: an oscillating-wing windmill. *Journal of energy*, 5(2):109–115, 1981.

[65] V Hugo Schmidt. Piezoelectric wind generator, August 20 1985. US Patent 4,536,674.

[66] S Pobering and N Schwesinger. A new micro hydro power device. *Poster Nanotech*, pages 23–27, 2003.

[67] William P Robbins, Dustin Morris, Ivan Marusic, and Todd O Novak. Wind-generated electrical energy using flexible piezoelectric mateials. In *ASME 2006 International Mechanical Engineering Congress and Exposition*, pages 581–590. American Society of Mechanical Engineers, 2006.

[68] Eriko Shimizu, Koji Isogai, and Shigeru Obayashi. Multiobjective design study of a flapping wing power generator. *Journal of Fluids Engineering*, 130(2):021104, 2008.

[69] Niell G Elvin and Alex A Elvin. The flutter response of a piezoelectrically damped cantilever pipe. *Journal of Intelligent Material Systems and Structures*, 20(16):2017–2026, 2009.

[70] Liaosha Tang, Michael P Païdoussis, and Jin Jiang. Cantilevered flexible plates in axial flow: energy transfer and the concept of flutter-mill. *Journal of Sound and Vibration*, 326(1-2):263–276, 2009.

[71] Matthew Bryant and Ephrahim Garcia. Energy harvesting: a key to wireless sensor nodes. In *Second International Conference on Smart Materials and Nanotechnology in Engineering*, volume 7493, page 74931W. International Society for Optics and Photonics, 2009.

[72] Shuguang Li and Hod Lipson. Vertical-stalk flapping-leaf generator for wind energy harvesting. In *ASME 2009 Conference on Smart Materials, Adaptive Structures and Intelligent Systems*, pages 611–619. American Society of Mechanical Engineers, 2009.

[73] Matthew Bryant and Ephrahim Garcia. Development of an aeroelastic vibration power harvester. In *Active and Passive Smart Structures and Integrated Systems 2009*, volume 7288, page 728812. International Society for Optics and Photonics, 2009.

[74] Carlos De Marqui Jr, Alper Erturk, and Daniel J Inman. Piezoaeroelastic modeling and analysis of a generator wing with continuous and segmented electrodes. *Journal of Intelligent Material Systems and Structures*, 21(10):983–993, 2010.

[75] Shuguang Li, Jianping Yuan, and Hod Lipson. Ambient wind energy harvesting using cross-flow fluttering, 2011.

[76] JA Dunnmon, SC Stanton, BP Mann, and EH Dowell. Power extraction from aeroelastic limit cycle oscillations. *Journal of Fluids and Structures*, 27(8):1182–1198, 2011.

[77] Carlos De Marqui Jr and Alper Erturk. Electroaeroelastic analysis of airfoil-based wind energy harvesting using piezoelectric transduction and electromagnetic induction. *Journal of Intelligent Material Systems and Structures*, 24(7):846–854, 2013.

[78] Mohamed Y Zakaria, Mohammad Y Al-Haik, and Muhammad R Hajj. Experimental analysis of energy harvesting from self-induced flutter of a composite beam. *Applied Physics Letters*, 107(2):023901, 2015.

[79] Jared D Hobeck and Daniel J Inman. Energy harvesting from turbulence-induced vibration in air flow: Artificial piezoelectric grass concept. In *ASME 2011 Conference on Smart Materials, Adaptive Structures and Intelligent Systems*, pages 637–646. American Society of Mechanical Engineers, 2011.

[80] GRS Assi, JR Meneghini, JAP Aranha, PW Bearman, and E Casaprima. Experimental investigation of flow-induced vibration interference between two circular cylinders. *Journal of Fluids and Structures*, 22(6-7):819–827, 2006.

[81] GRS Assi, PW Bearman, and JR Meneghini. On the wake-induced vibration of tandem circular cylinders: the vortex interaction excitation mechanism. *Journal of Fluid Mechanics*, 661:365, 2010.

[82] TK Prasanth and S Mittal. Flow-induced oscillation of two circular cylinders in tandem arrangement at low re. *Journal of Fluids and Structures*, 25(6):1029–1048, 2009.

[83] Huakun Wang, Wenyu Yang, Kim Dan Nguyen, and Guoliang Yu. Wake-induced vibrations of an elastically mounted cylinder located downstream of a stationary larger cylinder at low reynolds numbers. *Journal of Fluids and Structures*, 50:479–496, 2014.

[84] Zhaolong Han, Dai Zhou, and Jiahuang Tu. Wake-induced vibrations of a circular cylinder behind a stationary square cylinder using a semi-implicit characteristic-based split scheme. *Journal of Engineering Mechanics*, 140(8):04014059, 2014.

[85] Yan Bao, Cheng Huang, Dai Zhou, Jiahuang Tu, and Zhaolong Han. Two-degree-of-freedom flow-induced vibrations on isolated and tandem cylinders with varying natural frequency ratios. *Journal of Fluids and Structures*, 35:50–75, 2012.

[86] D Brika and A Laneville. The flow interaction between a stationary cylinder and a downstream flexible cylinder. *Journal of Fluids and Structures*, 13(5):579–606, 1999.

[87] FS Hover and MS Triantafyllou. Galloping response of a cylinder with upstream wake interference. *Journal of fluids and structures*, 15(3-4):503–512, 2001.

[88] Jimmy Fung Jr. *Parameter identification of nonlinear systems using perturbation methods and higher-order statistics.* PhD thesis, Virginia Tech, 1998.